UNIVERSITY OF OKLAHOMA
GRADUATE COLLEGE

Coarse-Grained Simulation of Heat Transport in Functionalized Nanotubes for Biomedical Applications

A DISSERTATION SUBMITTED TO THE GRADUATE FACULTY

in partial fulfillment of the
requirements for the degree of

Doctor of Philosophy

By

Delaram Nematollahi

Norman, Oklahoma

Downloaded from SHAREOK. Persistent Handle URL: https://hdl.handle.net/11244/341647

COARSE-GRAINED SIMULATION OF HEAT TRANSPORT IN FUNCTIONALIZED NANOTUBES FOR BIOMEDICAL APPLICATIONS

A DISSERTATION APPROVED FOR THE
HOMER L. DODGE DEPARTMENT OF PHYSICS AND
ASTRONOMY

BY THE COMMITTEE CONSISTING OF

Dr. Kieran Mullen, Chairperson

Dr. Bruno Uchoa

Dr. Michael B. Santos

Dr. Arne Schwettmann

Dr. Dimitrios V. Papavassiliou

© Copyright 2025
by
Delaram Nematollahi
All Rights Reserved.

To My Mom & Dad for always being there for me.

Acknowledgements

First and foremost, I want to deeply thank my advisor, Dr. Kieran Mullen. He not only helped me develop essential research skills but also nurtured my ability to think critically and independently. He gave me the freedom to find a project that matched both my intellectual curiosity and desire to contribute to real-world applications. I've always loved physics and found joy in understanding the world around me. But during my PhD, I came to realize that I also needed a deeper sense of human connection in my work. I'm grateful that my current project, with its biomedical applications, allows me to contribute to society in a meaningful way. My fascination with physics began in high school when Mr. Hasan Zahmatkesh introduced us to Van de Graaff generators and light-scattering experiments. I was amazed that the beauty of nature could be explained through mathematics. Physics not only deepened my understanding of the world, but also taught me critical thinking—something I apply in all aspects of my life. Since childhood, I have been drwn art, but discovering physics revealed a new kind of beauty: the elegance of using simplified models to describe complex phenomena. To me, physics is also the art of seeing the world differently. I pursued physics as my major at Ferdowsi University of Mashhad, where I particularly enjoyed Dr. Shahtahmasebi's condensed matter classes. He made complex topics both understandable and enjoyable. Getting admitted to the University of Oklahoma was a big opportunity for growth, and I was thrilled. I'll never forget how Dr. Bumm patiently and promptly answered my emails, helping me understand the process when I first arrived. This experience helped me grow as a physicist, and I truly appreciated courses like Statistical

Physics with Dr. Barbara Capogrosso and Quantum Mechanics with Dr. Gutierrez. I've learned a lot in Dr. Schwettmann's lab. I was his first student, and he gave me the unique opportunity to help build the lab from scratch. We installed the vacuum system, set up the optical trapping apparatus, and I even built a lock-in amplifier. I also had the chance to fabricate AMO component holders in the machine shop, which helped me become familiar with machining tools and techniques. I would like to thank Joel and Barry for their guidance and support during that time. I later explored skyrmions, and finally focused on heat transfer in single-walled carbon nanotubes (SWCNTs) for photothermal therapy. Throughout this journey, I not only developed lab and theoretical skills but also had the privilege of meeting amazing people for whom I'm deeply grateful. I want to sincerely thank my committee members, Dr. Mike Santos, Dr. Arne Schwettmann, Dr. Bruno Uchoa, and Dr. Dimitrios Papavassiliou, for their support and guidance. Dr. Dimitrios Papavassiliou, in particular, held biweekly meetings with me and my advisor, offering invaluable help. Dr. Santos gave me the opportunity to participate in outreach programs for high school students, which was a wonderful experience. Dr. Santos, Dr. Schwettmann and Dr. Uchoa challenged me to think deeper with their insightful questions. A very special thanks goes to my academic coach, Dr. Sherri Irvin. Her unwavering support made me feel like I had a mentor, a best friend, and a family member all in one. I turned to her during some of the darkest moments of my journey, and she helped me stand back up and believe in myself again. Her guidance and care meant more than words can express. I would like to thank Thao Nguyen (Dr. Papavassiliou PhD student at the time) who helped me out to get started with LAMMPS and coarse graining method. A heartfelt thank you to my academic pen pal, Dr. Carlos Jaime, author of one of my most-cited papers. He answered all my questions with incredible kindness and depth. Though we've never met in person, his guidance has meant so much to me. I'm deeply grateful for the friends who became like family during this journey. Saloni Bhatiani, Tannaz Sadri, Neda Bathae, and Hanieh Farsibaf, my sisters of more than ten years, thank you for always being there for me. Saloni, nothing could ever replace our chai breaks filled with

deep conversations, laughter, and the warmth of your presence. Those moments kept me grounded, and I will always cherish them. Tannaz, your constant care and love mean the world to me. you have always listened to me like a true sister. You cared so deeply and so genuinely, and I cannot put into words how much I appreciate and love you. Neda, the strong and graceful soul I will always look up to, your presence has been a blessing. You supported me through everything and even referred me to a job that now I have a second interview for, after graduation. I will never forget your kindness and strength. Hanieh, thank you for sharing both tears and laughter with me, through every moment I knew I could rely on you. Your friendship has been a steady light. I also sincerely thank Mojgan Padash and Mahbobeh Lesani , Nazli Rasouli and her caring family, for your genuine care, support and kindness. Tim Woodworth, who taught me how to drive when I first came to Norman, thank you.. OU has become my second home. Everyone I met truly cares. Debi Kolar Schoenberger and her warm hugs (and candy drawer!) were always a source of comfort. Cynthia, Hilary, and the entire Homer L. Dodge Physics Department, the Center for Quantum Research, and the College of Arts and Sciences, thank you for the opportunity and financial support. I also want to thank the Farzaneh family for their scholarships and support throughout this journey. I want to convey my deep appreciation and gratitude for Universidad Nacional de San Agustín de Arequipa and the PIs on this project, especially Dr. Rogers Harrison, for funding and supporting this work. I also want to thank the staff of the OU-Supercomputing center for always being helpful. I'd like to thank my friends and colleagues Hua Wang and Alex Kerr, who made this time more joyful. I also want to thank Joseph Choi, who has always been by my side throughout this journey, we even took ballet classes together! Thank you, Joseph, for your friendship and constant support. I'm also thankful for Rishab, Saesun, Geo, Tim Woodworth, Vincent White, Mitchel Yothers, Qimin zhang, Aaron Foster, Mahyar Esmaeelpour, Milad Nourbakhsh, Hadi Afshari, Jake pederson and many other colleagues whose names may not come to mind at the moment, but whose presence and help I will always carry in my heart. To all my colleagues, though I can't name everyone here, please

know I carry your kindness and support with me always. Most importantly, I want to thank my mother, Imandokht Mojaversoofi, and my father, Kamaloddin Nematollahi, who are my world. Their endless love, strength, and sacrifice allowed me to explore the world and chase my dreams, even though it meant being far away from their child for many years. Their support has been the foundation of everything I've accomplished. I'm also deeply grateful to my beloved siblings, Fatemeh, Hoori, and Javad—whose love has been a constant source of strength. And to my dear niece and nephew, Ava and Avash, who feel like my own children and who have filled our family with joy, thank you for being such bright lights in my life.

"At times our own light goes out and is rekindled by a spark from another person. Each of us has cause to think with deep gratitude of those who have lighted the flame within us."

—Albert Schweitzer

Abstract

This thesis presents the development of a mesoscopic simulation framework using energy-conserving Dissipative Particle Dynamics (eDPD) to investigate thermal transport phenomena at the interface between carbon nanotubes (CNTs) and biological materials in aqueous environments. We introduce a novel method for including Kapitza in resistance by tuning repulsion and heat exchange parameters within the eDPD framework, enabling accurate modeling of interfacial heat transfer between single-walled carbon nanotubes (SWCNTs) and water. In developing this method, we resolve some discrepancies in the eDPD algorithm as currently described in the literature.

We observed that thermal boundary resistance at a liquid interface can be increased by as much as ∼40% by increasing the interfacial repulsion. Furthermore, thermal rectification can be modeled by introducing asymmetry in the interfacial parameters, demonstrating that heat conduction through a carbon–fluid interface becomes direction-dependent under certain functionalization or temperature gradient conditions. This insight provides a foundation for designing the surfrace properties of materials with directional heat transport capabilities, which are relevant for thermal management and biomedical control.

We provide a systematic approach for selecting DPD parameters that reproduce realistic thermal and mechanical properties of carbon nanotubes and surrounding media. We applied our coarse-grained model to study the adsorption behavior of DSPE-PEG amphiphilic molecules near CNTs. By varying temperature and concentration, one can examine how these factors affect protein-like molecular anchoring to the CNT surface. Our model

captures essential features of polymer–nanotube interactions, including the number and spatial configuration of anchored molecules. Simulations indicate a competition between DSPE-PEG agglomeration and DSPE-PEG/CNT binding. We find that the binding of amphiphilic molecules to CNTs is not degraded by transient heating of CNTs, suggesting that pulsed radiation can be used in photothermal therapy.

Table of Contents

Acknowledgements v

Abstract x

List of Tables xiv

List of Figures xv

Chapter 1: Introduction 1

1.1 Motivation: The fight against cancer 1

1.2 Background: Carbon nanotubes 2

1.3 CNT and Cancer Therapy 5

1.4 Thesis outline 9

1.5 Summary 10

Chapter 2: Theory and Parametrization of Energy-Conserving Dissipative Particle Dynamics (DPDE) 11

2.1 Introduction to Dissipative Particle Dynamics (DPD) 11

2.1.1 The Dissipative Particle Dynamics (DPD) Simulation Method 13

2.2 Calibration of the Repulsion Parameter in DPD Simulations 20

2.2.1 Matching Compressibility 20

2.2.2 Mapping to Flory–Huggins Theory in Mixtures 21

2.2.3 Summary of Practical Guidelines 22

2.2.4 Advantages of DPD and Soft Potentials 22

2.3 Parametrization of DPD Models 24

2.3.1 Compressibility-Based Estimation of a_{ii} 24
2.3.2 Heterogeneous Repulsion via Flory–Huggins Parameter 24
2.3.3 Thermodynamic Matching of $\boldsymbol{\kappa_{ij}}$ & $\boldsymbol{a_{ij}}$ 25
2.4 Energy-Conserving Dissipative Particle Dynamics (DPDe) for Heat Transfer 25
2.4.1 Governing Equations 26
2.4.2 Heat Exchange Mechanisms; Connection Between Collisional Heat Flux and Macroscopic Thermal Conductivity 27
2.4.3 Fluctuation–Dissipation Consistency 33
2.4.4 Practical Parameter Choices 34
2.4.5 Applications and Summary 34
2.5 Timestep Selection for eDPD Simulations 34
2.6 Summary 44
Chapter 3: Coarse-Grained Model Development and Simulation Setup 46
3.1 Introduction 46
3.2 General simulation parameters 48
3.2.1 Length and Time Scale Mapping to Real Units 48
3.2.2 Lattice Geometry and Physical Basis 51
3.2.3 Soft-Repulsion Parameters 53
Chapter 4: LAMMPS-Based Modeling of SWCNT Mechanics and Kapitza Resistance 56
4.1 Introduction 56
4.1.1 Modelling and measuring thermal conductivity in LAMMPS 57
4.1.2 System Stability and Thermal Transport: Sensitivity to Bin Size and Timestep 67
4.1.3 Modeling thermal interface resistance in LAMMPS 73
4.2 Kapitza resistance between carbon and water 74
4.3 Effect of hydrophobicity on Kapitza resistance 76
4.4 Kapitza resistance comparison between cold and hot interfaces 79

4.5 Conclusion 79
Chapter 5: Mesoscale Simulation of SWCNT and DSPE-PEG Using eDPD 81
5.1 Introduction 81
5.2 Modeling Heat Transfer from a Single-Walled Carbon Nanotube (SWCNT) in Water 83
5.2.1 Simulation Setup 83
5.2.2 Thermal Initialization and Time Integration 83
5.2.3 Converting Volumetric Heat Capacity to Dimensionless Form in eDPD Simulations 85
5.3 DSPE-PEG Adsorption on SWCNT using eDPD 94
5.3.1 DSPE-PEG Coarse-Grained Model and Simulation Setup 96
5.3.2 Mass and Bead Types 97
5.3.3 Pairwise Repulsion Parameters a_{ij} 97
5.3.4 Bond and Angle Coefficients 97
5.3.5 Choosing γ and Dynamic Properties 98
5.4 Observables and Coating Efficiency 99
Chapter 6: Conclusion and Future Work 103
6.1 Summary of Findings 103
6.2 Quantitative Metrics 105
6.3 Scientific Implications 105
6.4 Future Work 105
6.5 Concluding Remarks 106
Appendix A: LAMMPS Simulation Input Script 108

List of Tables

2.1 Corrected eDPD parameters used in the simulation. 37

3.1 Soft repulsion parameters a_{ij} used in this article for a system composed of DMPC molecules, one SWCNT, and water. 54

5.1 Bead types and corresponding masses used in the simulation. 97

5.2 Repulsion parameters a_{ij} and dissipative coefficient γ between coarse-grained bead types. 98

5.3 Bond coefficients. 98

5.4 Angle coefficients used in the simulation. 98

List of Figures

1.1 Schematic illustrations of photothermal therapy. Top: Cartoon representation. Bottom: Realistic biological setup involving carbon nanotube targeting and tumor interaction.(*This figure was kindly provided and adapted with permission from Dr. Roger Harrison, whose support is sincerely appreciated.)* 3

1.2 Single-walled carbon nanotubes (SWNTs) are formed by rolling a graphene sheet into a cylinder. Depending on the direction of rolling, they are classified as *armchair* (m, m), *zigzag* $(n, 0)$, or *chiral* (n, m) nanotubes, where $n > m > 0$. (Feng 2015) 4

1.3 Schematic illustration of thermal boundary resistance (TBR) at the carbon nanotube (CNT)–water interface. An optical pump–probe technique is used to heat the CNT and monitor heat dissipation across the interface. The mismatch in vibrational (phonon) spectra between the CNT and surrounding water leads to a temperature discontinuity and limits heat flow, characterized as Kapitza resistance. (Casto et al. 2024) 7

2.1 Schematic representation of mesoscopic behavior in DPD simulations Li et al. (2017). 12

2.2 The pairwise interactions between two DPD particles consist of three components: a conservative force, modeled as a harmonic spring; a dissipative force, represented by a dashpot that dampens relative motion; and a random force, which simulates Brownian motion. Together, the dissipative and random forces form a Brownian dashpot, maintaining thermal equilibrium. (Santo and Neimark 2021). 14

3.1 The atomistic structure of DMPC and its corresponding coarse-grained model used in this study are shown. Lime-colored beads represent the hydrophobic components, while mauve-colored beads indicate the hydrophilic regions. . . 49

3.2 Schematic of the coarse-grained model used for carbon nanotubes (CNTs). The spheres represent the centers of mass of coarse-grained beads distributed along the CNT wall. Grey beads correspond to phenalene-like carbon structures, while red beads represent phenalene-like units functionalized with polar groups such as –OH or –COOH. (Valdivia and Jaime 2021) 52

4.1 VMD visualization of Computational setup in LAMMPS showing two distinct materials separated by an interface. The left region (pink) consists of one material, while the right region (teal) consists of a different material, enabling the study of Kapitza resistance at the interface. 59

4.2 Schematic of the model: heating and cooling regions at constant equal rates produce a temperature profile with the purpose of extracting the thermal conductivity. The system has periodic boundary conditions in x, y and z directions. 60

4.3 Plot showing the temperature as a function of position while varying the interfacial thermal conductivity k_{ij} and specific heat capacity C_V, while holding the product $k_{ij}C_V^2$ constant. The simulation was performed in a periodic box spanning $-20 \leq x \leq 20$, $-20 \leq y \leq 20$, and $-10 \leq z \leq 10$, filled with 128,000 energy-conserving DPD particles (64,000 of each type). Type 1 particles were assigned $C_V = 1.0 \times 10^5$, while Type 2 particles were assigned $C_V = \frac{1.0\times10^5}{\sqrt{\alpha}}$, and thermal conductivity scaled as $k = \alpha \cdot 1.45 \times 10^{-5}$ to preserve $k_{ij}C_V^2$. A fixed heat flux of ± 0.005 was applied at $x = \pm 10$, and temperature profiles were obtained after 100,000 timesteps using a timestep size of 0.01. Temperature was calculated per bead and averaged in 1D spatial bins of size 0.05. 62

4.4 Scaling of the slope $\frac{dT}{dx}$ as a function of α. The results suggest that $k_{i,j} \propto \tilde{\kappa}/C_V^2$ is not supported by the numerical data. 63

4.5 Temperature gradient variation with respect to $\tilde{\kappa}$ scaling, demonstrating a clear $\frac{1}{\alpha}$ relationship. 64

4.6 Temperature gradient variation with respect to C_v scaling, demonstrating a clear $\sqrt{\alpha}$ relationship. 65

4.7 Comparison of nonlinear (blue solid line) and linear (red dashed line) fits for the temperature gradient $\frac{dT}{dx}$ as a function of α under C_v scaling. The nonlinear fit, corresponding to $\sqrt{\alpha}$, shows better agreement with the data than the linear fit, suggesting that $\frac{dT}{dx} \propto \sqrt{\alpha}$ provides a more accurate description of the scaling behavior. 66

4.8 Temperature profile for two regions with identical heat capacities ($C_{V1} = C_{V2}$) using bin size 0.5. The simulation used timestep $\Delta t = 0.01$ and collapsed after 77,000 timesteps due to instability. 68

4.9 Temperature evolution from the original Li input file using $\Delta t = 0.01$. Simulation becomes unstable and fails at timestep 67,000. 69

4.10 Two-region simulation using Li's parameters with larger bin size (1.0) and smaller timestep ($\Delta t = 0.001$). The system remains stable for over 1,000,000 timesteps. The lower data points indicate that the system becomes unstable and produces unphysical temperature values. 70

4.11 shows the case where the values of C_V are different in the two regions, corresponding to a water–hypothetical material interface. 71

4.12 A temperature jump is observed at the water–carbon interface, indicating the presence of interfacial thermal resistance (Kapitza resistance) between the two materials. 75

4.13 Kapitza resistance R_K as a function of microscopic thermal conductivity parameter κ_{CW} for two cases: solid–liquid (red circles) and solid–solid (blue triangles) across a carbon–water interface. The resistance was extracted from simulations by linearly extrapolating the temperature profiles near the interface and calculating the temperature jump divided by the heat flux. The fits indicate a similar trend in both cases, with R_K values approximately in the range of 10^{-8} $\mathrm{Km^2/W}$, consistent with previous studies by Alexeev et al. (2015). This suggests that interfacial thermal resistance is governed primarily by the contrast in heat capacities and coupling coefficients, and is not strongly sensitive to whether the interface is between a solid and a liquid or two solids. 77

4.14 Direct correlation between the repulsive parameter and Kapitza resistance, demonstrating how fine-tuning the repulsive parameter can significantly impact interfacial heat transfer 78

4.15 Temperature profiles across a water–carbon interface for two opposite heat flow directions. The blue curve represents the case where heat flows from carbon (hot) to water (cold), while the red curve corresponds to the reverse situation where heat flows from water (hot) to carbon (cold). Linear fits are applied separately on either side of the interface to extract the temperature jump ΔT in each case, indicated by vertical arrows. The observed difference in ΔT highlights the asymmetry in Kapitza resistance depending on the direction of heat transfer. 80

5.1 VMD schematic of simulated SWCNT in water. 84

5.2 Exponential fit of the temperature decay profile of a heated single-walled carbon nanotube (SWCNT) immersed in water, as obtained from energy-conserving DPD (eDPD) simulations. The curve demonstrates the use of a lumped-capacitance model, which assumes uniform SWCNT temperature and radial heat dissipation to the surrounding fluid. The fitted exponential form allows extraction of the characteristic thermal relaxation time τ, which is then used to estimate the SWCNT's effective thermal conductivity κ. 90

5.3 Schematic representation of DSPE-PEG molecules interacting with a SWCNT. Some DSPE-PEG molecules exhibit adhesion by aligning their hydrophobic tails closely to the SWCNT surface, while others remain at various angles due to thermal motion or unfavorable orientation. The scissor-shaped DSPE structure is composed of two hydrophobic tails and a hydrophilic head, with the PEG chain extending in random directions. Molecules within a threshold angle or distance from the CNT are considered "stuck." 95

5.4 Probability histogram of minimum distances from DSPE tail beads to SWCNT surface. The peak at short distances (0–1 r_c) indicates strong and persistent adsorption. Bin width is 0.2. 101

5.5 Time evolution of the percentage of DSPE–PEG molecules with tail bead within 1.2 r_c of the SWCNT surface. The fitted curve shows rapid initial adsorption followed by saturation, reflecting stable long-term binding. 101

Chapter 1

Introduction

"Everything that living things do can be understood in terms of the jiggling and wiggling of atoms"

– Richard Feynman

1.1 Motivation: The fight against cancer

Fighting cancer cells has always been a challenging endeavor. Cancer encompasses a wide range of diseases marked by the uncontrolled growth and spread of abnormal cells, with more than 200 distinct types classified based on tissue origin. A significant proportion of cancer-related deaths are not caused by the primary tumor itself, but by metastases; secondary growths that invade distant tissues and disrupt vital organ function (Dillekås et al. 2019). According to the American Cancer Society, cancer is projected to cause approximately 611,720 deaths in the United States in 2024, making it the second leading cause of death, following heart disease (Siegel et al. 2024). Despite advances in treatment, the high mortality rate underscores the urgent need for improved therapeutic strategies. In recent years, nanotechnology has emerged as a promising field in oncology, offering innovative tools for targeted drug delivery, imaging, and minimally invasive therapy. Among various

nanomaterials, carbon nanotubes (CNTs) stand out due to their unique structural, electrical, and thermal properties. Their ability to absorb near-infrared light and convert it into heat makes them particularly attractive for photothermal therapy, a technique that can selectively ablate tumor cells with minimal impact on healthy tissue (Zhou et al. 2009). Additionally, CNTs can serve as vehicles for transporting therapeutic agents directly to cancerous sites. Current cancer treatments have serious side effects and can even be fatal. The goal of this thesis is to use computational physics to develop a deep understanding of the fundamental heat transfer phenomena involved in photothermal cancer treatment and to propose a holistic approach to manufacture nanobiomaterials that are effective agents for selectively killing cancer cells. We are developing a mesoscale model to fundamentally understand the energy transport of functionalized carbon nanotubes for tumor photothermal therapy. We are focusing on single-walled carbon nanotubes (SWCNTs) heated either by radiofrequency fields or near-infrared radiation. These SWCNTs will be functionalized with a target protein annexin AXNA5, and other molecules, to have the ability to selectively choose cancer cells while improving heat transfer to sick cells. SWCNTs with shorter lengths (between 100 and 1500 nm) are desired for clinical use; shorter nanotubes can be delivered more easily and will result in penetrations farther into tumors (Bui et al. 2011b). Figure 1 illustrates a schematic representation of the photothermal therapy process.

1.2 Background: Carbon nanotubes

Since carbon nanotubs (CNTs) were first discovered by Iijima in 1991 (Iijima 1991), they have gained extensive attention due to their unique characteristics: large surface area to volume ratio, ability to be functionalized, and stability (Bui et al. 2011b).

Because of their potential for functionalization and versatile surface chemistry, CNTs can have both large-scale and small-scale applications. Large-scale applications include

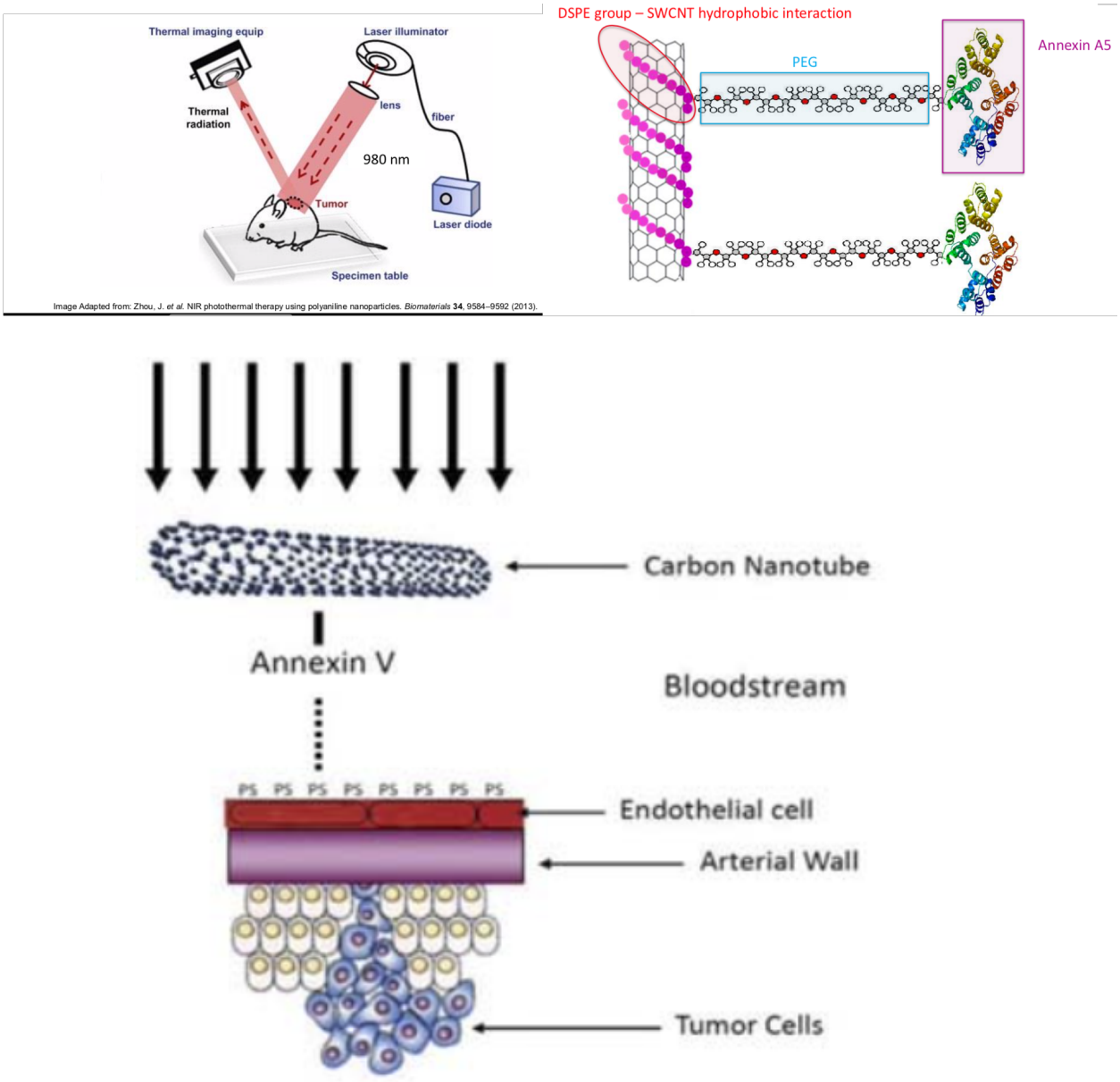


Figure 1.1 Schematic illustrations of photothermal therapy. Top: Cartoon representation. Bottom: Realistic biological setup involving carbon nanotube targeting and tumor interaction.(*This figure was kindly provided and adapted with permission from Dr. Roger Harrison, whose support is sincerely appreciated.)*

adsorbents, water purification, oil-spill clean ups, water purification, membranes, and chemical traps. Smaller-scale applications of CNTs include biosensors, medical devices and cancer therapy. CNTs can be used in cancer therapy due to their unique interactions

with different wavelengths of lights to generate heat and reactive oxygen species, and their versality as drug carriers (Bui et al. 2011b).

Carbon nanotubes are classified into two large categories: single-walled (SWCNTs) and multiwalled (MWCNTs) carbon nanotubes. A single graphene sheet rolled into a cylinder is called a SWCNT, while we can construct MWCNTs by rolling multiple graphene sheets into concentric cylinders. Diameters of SWCNTs are ranging from 0.4 to 2 nm, while MWCNTs diameters are from 1 to 100 nm with wall thickness 0.2 to 2 nm (Peters et al. 2008).

Another characteristic of nanotubes is their chirality (Figure 1.3), which determines whether

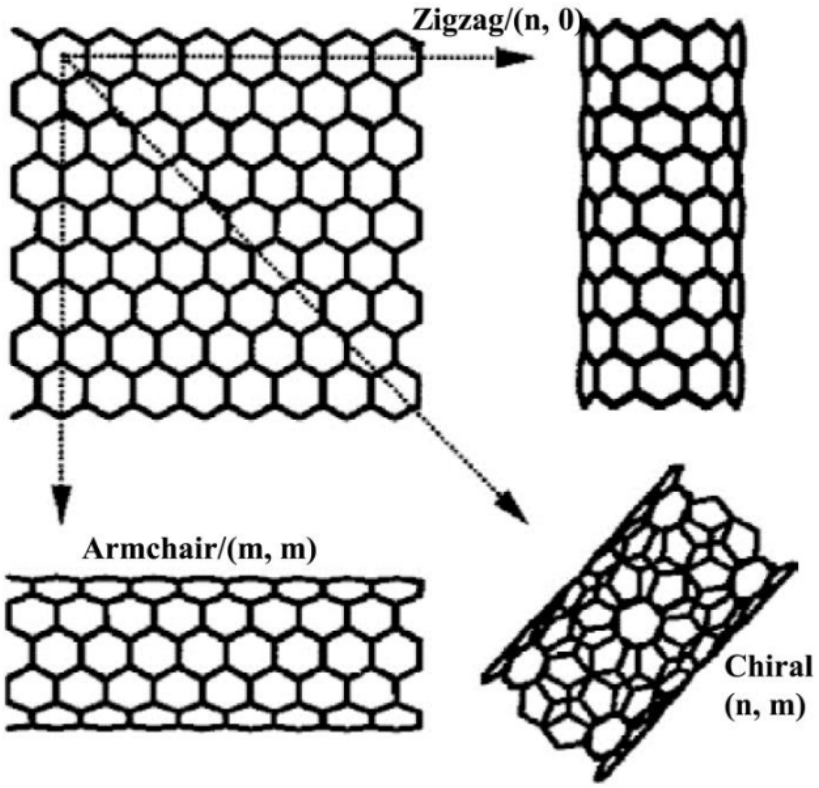


Figure 1.2 Single-walled carbon nanotubes (SWNTs) are formed by rolling a graphene sheet into a cylinder. Depending on the direction of rolling, they are classified as *armchair* (m, m), *zigzag* $(n, 0)$, or *chiral* (n, m) nanotubes, where $n > m > 0$. (Feng 2015)

a tube is metallic or semiconductor. The chirality of a nanotube can be chair-in-chair, zigzag-in-chair,ir, zigzag-in-chair, or chiral. We can define photothermal therapy as the ability of a substance to absorb near-infrared (NIR) light or radio frequency field energy and convert it

to heat. (Jakubinek et al. 2010).

I will discuss specifics of their heat transport properties in the next subsection.

1.3 CNT and Cancer Therapy

Biological systems are highly transparent to NIR light wavelength between 700-1000 nm (NIR can penetrate up to a few micrometers). Energy penetration by RF fields is also excellent but at relatively low frequencies (tens of MHz). (Son et al. 2016; Gannon et al. 2007). Compared to microwave frequencies, low frequency RF fields have a more effective penetration into biological tissue. However, RF fields are naturally less focused due to their longer wavelength. SWCNTs can fix this issue by providing material-based heating localization. If a cell temperature reaches 41-42 °C for a long period, it undergoes hyperthermia, which is basically cell death, increased sensitivity to chemotherapy and radiotherapy, and stimulation of immunogenicity. If the cell temperature goes above 47-60 °C, ablation occurs. Ablation is characterized by microvascular thrombosis, hypoxia, ischemia, protein denaturing, and plasma membrane destruction leading to cell death. (Jakubinek et al. 2010).

Kam et al, for the first time in 2005, showed that carbon nanotubes have a strong absorption of NIR light (Sanginario et al. 2017; Kam et al. 2005). In their study, they modified the surface of SWCNTs with either DNA or a folate moiety specifically targeted to tumors. They internalized the nanotubes into the cytoplasm of cervical cancer cells at 37 °C. Adding 808 nm NIR light at 168 Jcm^{-2} energy led to in vitro cell death. Even at high energies as 1050 Jcm^{-2}, they observed minimal damage in cells without nanotubes.

More in vitro studies were conducted with anti-HER2 targeted SWCNTs using the 808 nm NIR laser. In comparison with phosphate buffered saline solution temperature increase that was $< 0.5°C/min$ over a period of two minutes, the nanotube suspension solution temperature increased at a rate of $7°C/min$. Cell death rate in breast cancer cells treated with targeted nanotubes underwent a significant increase compared to untargeted nanotubes

with NIR radiation (Madani et al. 2011; Xiao et al. 2009).

There have been several other studies on treating various types of cancers, using SWCNTs and multi-walled carbon nanotubes (MWCNTs), since the initial work done by Kam et al. Most of the research on the use of CNTs for photothermal therapy of cancer has been done using NIR irradiation except by Gannon et al. in which an RF field was used on SWCNTs injected into liver tumors (Son et al. 2016). There was no attempt though in this study to determine the RF frequency at which there was maximum heating of SWCNTs.

Potential toxicity of carbon nanotubes is an important issue that needs to be investigated for them to be used in therapy.

Although both MWCNTs and SWCNTs can be degraded by enzymatic activation by members of the oxidase family in vivo, there is still a difference between their toxicity (Gannon et al. 2007; Kam et al. 2005). A CNT's size is its most important characteristic that contributes to toxicity. A CNT's length can range from a few nanometers to several micrometers. This length can determine whether the CNT is capable of interacting with biological systems on the nanoscale, as well as macroscopic scale. In general, the lowest toxicity belongs to very short ($<\sim 1\mu m$) nanotubes with aspect ratios (length/diameter) greater than ~ 1000 which are relatively flexible, such as SWCNTs (Xiao et al. 2009).

CNTs can be classified into "biologically stiff" and "biologically soft" groups. Generally, MWCNTs are classified as biologically stiff and toxic, while SWCNTs of any length belong to the biologically soft and non-toxic category. The other important characteristic that we are looking for in a nanotube to be used in photothermal therapy, is high thermal conductivity. CNTs have exceptionally high thermal conductivity ($\sim 3000\, Wm^{-1}K^{-1}$) for multi-walled CNTs (Teradal and Jelinek 2017), and up to ($\sim 6000\, Wm^{-1}K^{-1}$) for SWCNTs at room temperature(Wang et al. 2014; Helland et al. 2008). The exceptional thermal conductivity of CNTs arises from their crystalline, quasi-one-dimensional structure that enables long phonon mean free paths and ballistic heat transport. SWCNTs, free from interlayer interfaces, often conduct heat better than MWCNTs, which suffer from inter-wall scattering and structural

defects. Aggregation into bundles or networks further reduces conductivity due to intertube resistance and misalignment.

At about 0.2 vol % in a matrix material, CNTs form a percolating network. Based on their aspect ratio, we would expect orders of magnitude larger thermal conductivities for CNT-based composites. These are the type of material we desperately need to use in biological applications such as photothermal therapy.

We are looking for an increase in the CNT composite thermal conductivity, but unfortunately, due to experimental results it only increases 50-100% relative to the pristine material. (Andón et al. 2013; Zhu et al. 2016). Interfacial resistance at the nanotube-matrix interface is the main reason for these disappointing results. (Kitiyanan et al. 2000; Resasco 2009). The thermal boundary resistance (TBR) known as "Kapitza resistance" at the interface of CNTs and the surrounding matrix, represents a heat flow barrier caused by the differences in the phonon spectra and possible imperfect contacts at the interface (Kitiyanan et al. 2000).

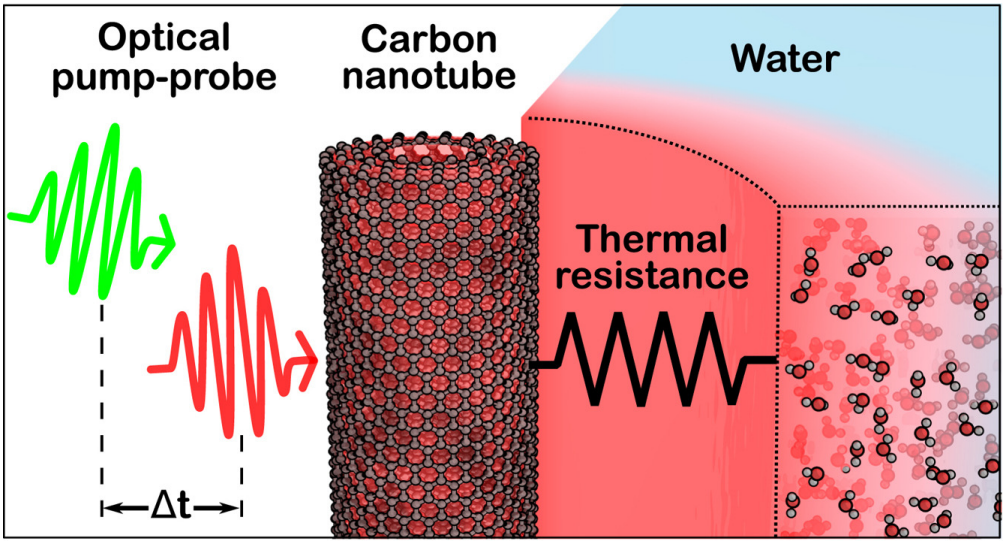


Figure 1.3 Schematic illustration of thermal boundary resistance (TBR) at the carbon nanotube (CNT)–water interface. An optical pump–probe technique is used to heat the CNT and monitor heat dissipation across the interface. The mismatch in vibrational (phonon) spectra between the CNT and surrounding water leads to a temperature discontinuity and limits heat flow, characterized as Kapitza resistance. (Casto et al. 2024)

The main issue now is to overcome TBR. One suggested way to improve the thermal properties of heat conducting CNT composites is the composite "densification" by increasing the volume fraction of the CNTs (Kitiyanan et al. 2000).

One other possibility is to modify the matrix-CNT interface by CNTs' functionalization. "Densification" turned out to be ineffective due to the tendency of nanotubes to form bundles. The reason is that CNT-CNT TBR is higher than the TBR between the CNT and the surrounding matrix (Bui et al. 2011b).

Functional groups, however, can significantly reduce the TBR between CNTs and between graphene sheets (Konatham and Striolo 2009; Fang et al. 2010).

Computational models for heat transfer in nanocomposites or suspensions can be classified into the three categories of macroscopic, mesoscopic and atomic level. In the macroscopic model, continuum-based approaches like finite element or finite volume methods are used and heat transfer around specific CNT configurations is simulated. A fine enough computational mesh is required to resolve the domain around individual CNTs [22]. In this method TBR is not considered explicitly. The second approach is the mesoscopic model, where Monte-Carlo (MC) based methods are used. An example of this is the study of heat transport in CNT composites with the thermal resistance at the matrix-nanotube interface (Duong et al. 2005) using an off-lattice MC simulation methodology. We can rely on this approach to estimate the thermal transport properties for SWCNT suspensions and for nanocomposites with SWNTs (Bui et al. 2011a). A third approach is the Molecular level simulation. For TBR calculations, we can use non-equilibrium Molecular Dynamics (NEMD) methods. There are two different ways to conduct NEMD simulations. In the first protocol, the system is initially at equilibrium with room conditions. Next we heat up the CNT and its temperature rises. CNT remains at that high temperature to equilibrate, and then we allow its temperature to decay (Shenogin et al. 2004; Neves et al. 2013). In summary, previous detailed computational studies are done on the two-phase systems in which the CNTs are suspended in a matrix

medium. We still need to investigate multiphase systems. We need to model CNTs in biological systems where the tissue is surrounding a cell membrane.

1.4 Thesis outline

This thesis is aimed at studying heat transfer through functionalized SWCNT in the cell environment.

Chapter 2 presents the theoretical background of Dissipative Particle Dynamics (DPD) and energy-conserving Dissipative Particle Dynamics (eDPD). It also describes the fundamental equations, force models, and integration schemes used in these mesoscopic simulation methods. We have used the energy conservation-Dissipative Particle Dynamics (eDPD) package from Large-scale Atomic/Molecular Massively Parallel Simulator (LAMMPS) software.

Chapter 3 outlines the development of the coarse-grained model used in this work. It includes the parameterization of single-walled carbon nanotubes (SWCNTs) and DSPE molecules, designed for accurate representation within the DPD/eDPD framework.

Chapter 4 focuses on the implementation challenges encountered when using the LAMMPS simulation package for this study. It includes simulations of the mechanical response of SWCNTs under applied strain, as well as investigations of Kapitza resistance at the carbon–water and SWCNT–water interfaces.

Chapter 5 investigates the interaction between DSPE molecules and SWCNTs in an aqueous environment. The chapter focuses on quantifying the percentage of DSPE molecules that remain attached to the nanotube surface and how temperature affects this attachment.

Chapter 6 summarizes the key findings of the thesis and offers perspectives for future work.

1.5 Summary

In this chapter, I introduced the motivation behind using functionalized carbon nanotubes for photothermal cancer therapy and provided an overview of their physical properties, potential for selective targeting, and mechanisms of heat transfer at the nanoscale. I also discussed the limitations of existing experimental and computational approaches, particularly in addressing the thermal boundary resistance (TBR) in biological environments. These challenges highlight the need for mesoscale modeling techniques capable of capturing both the physics of heat transport and the molecular-level interactions in biological systems. To address this, we have adopted the energy-conserving Dissipative Particle Dynamics (eDPD) method within the LAMMPS simulation framework. The following chapters detail the development, implementation, and application of this approach to model functionalized SWCNTs in aqueous and cellular environments, with the goal of advancing the design of efficient nanomaterials for photothermal therapy.

Chapter 2

Theory and Parametrization of Energy-Conserving Dissipative Particle Dynamics (DPDE)

In this chapter, we present a comprehensive overview of the theoretical foundations and practical implementation of the Energy-Conserving Dissipative Particle Dynamics (DPDE) method. We begin with a review of DPD and DPDE fundamentals, followed by a derivation of the DPDE algorithm, including the detailed role of Onsager coefficients and stochastic calculus. The chapter concludes with a discussion on DPD force field parametrization, including procedures for calculating repulsion parameters and thermodynamic consistency.

2.1 Introduction to Dissipative Particle Dynamics (DPD)

Many systems of academic and industrial relevance fall into the category of soft condensed matter, materials that are neither entirely solid nor purely liquid. These systems often exhibit structural and dynamical behaviors characteristic of the mesoscale, between the atomistic and macroscopic regimes. For example, in polymer gels, this mesoscopic scale is typically set by the distance between cross-links in the network, while in surfactant systems, the wavelength of lamellar bilayer undulations defines the relevant scale (Li et al. 2017).

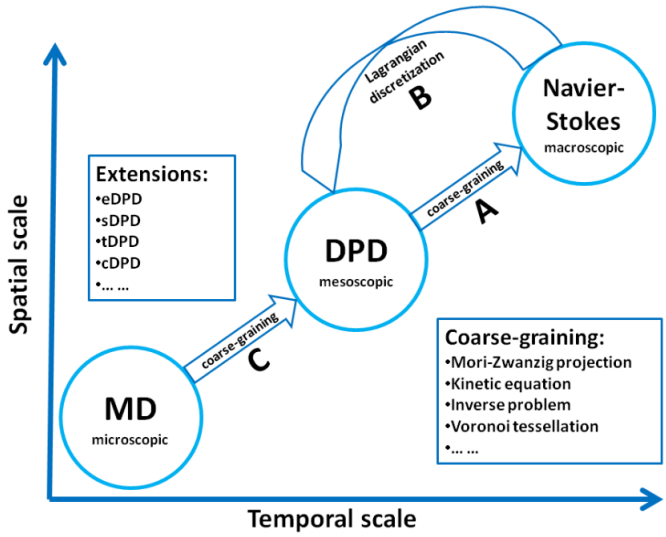


Figure 2.1 Schematic representation of mesoscopic behavior in DPD simulations Li et al. (2017).

Capturing the behavior of such systems requires simulation techniques capable of resolving mesoscale structures and dynamics without relying on full atomistic detail. Conventional methods such as lattice-based Monte Carlo simulations, self-consistent field theory, and dynamic density functional theory have provided valuable insight but are often limited in their ability to model complex architectures such as branched polymers, micelle-forming networks, and multiblock copolymers. Furthermore, these approaches typically neglect hydrodynamic interactions and assume fixed connectivity or associations, limiting their ability to predict self-assembly and dynamic restructuring.

To bridge this gap, Hoogerbrugge and Koelman introduced (Hoogerbrugge and Koelman 1992) Dissipative Particle Dynamics (DPD), a mesoscale simulation technique that models fluids using soft, interacting particles governed by conservative, dissipative, and stochastic forces. The key advantage of DPD lies in its ability to capture hydrodynamic behavior, simulate large time and length scales, and preserve essential thermodynamic properties such as temperature through a built-in fluctuation–dissipation balance.

Subsequent work by Español and Warren (Espanol and Warren 1995) formalized the DPD framework using the principles of non-equilibrium statistical mechanics. They demonstrated

that to recover the canonical ensemble, the dissipative and random forces must be related through the fluctuation–dissipation theorem. This ensured that DPD simulations could model systems at constant temperature while still allowing for realistic particle motion and momentum conservation.

Beyond reproducing hydrodynamics, DPD has become a powerful tool for modeling the self-organization of soft materials, including phase separation, micelle formation, and mesophase transitions. Its adaptability, combined with parametrization strategies grounded in thermodynamic theories such as Flory–Huggins, provides a pathway to connect atomistic detail (e.g., solubility parameters) to large-scale collective behaviors. In this chapter, we explain the theoretical foundations of the DPD method, highlight its thermodynamic consistency, and lay the foundation for its extension to energy-conserving models (DPDE) in the following sections (Groot and Warren 1997).

2.1.1 The Dissipative Particle Dynamics (DPD) Simulation Method

Understanding the behavior of multicomponent complex fluids, such as nanofluids and liquid-vapor mixtures, where the microstructure significantly affects macroscopic transport properties, is essential to thermal management. Traditional continuum methods, although effective at larger scales, often fail at interfaces, contact lines, or regions with sharp gradients, because of their inability to account for molecular-level physics. Molecular dynamics (MD) simulations, on the other hand, are atomistically accurate but limited by computational constraints to short timescales and small system sizes. Dissipative Particle Dynamics (DPD) (Schiller 2005; Santo and Neimark 2021) is a mesoscale method that bridges this gap.

DPD is a coarse-grained particle-based simulation method that models groups of atoms or molecules as mesoscopic particles called beads. The beads follow Newtonian mechanics using a discretized time algorithm that updates the i-th bead's position $\mathbf{r}_i$ and velocity $\mathbf{v}_i$ as

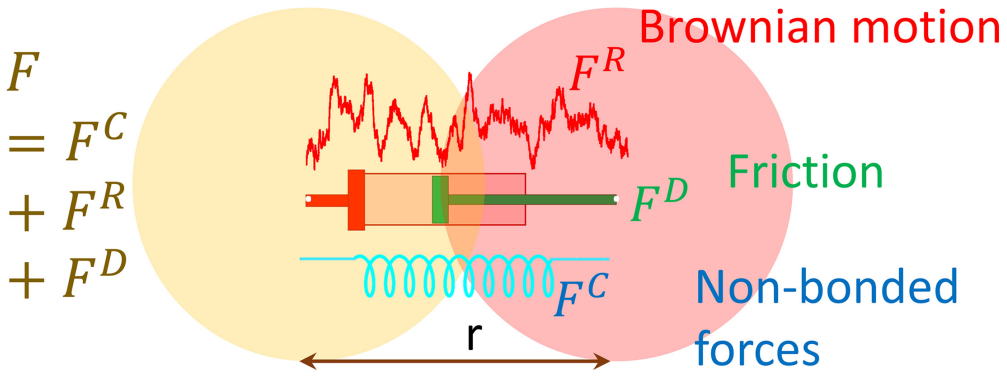


Figure 2.2 The pairwise interactions between two DPD particles consist of three components: a conservative force, modeled as a harmonic spring; a dissipative force, represented by a dashpot that dampens relative motion; and a random force, which simulates Brownian motion. Together, the dissipative and random forces form a Brownian dashpot, maintaining thermal equilibrium. (Santo and Neimark 2021).

determined by $\mathbf{F}^C$, $\mathbf{F}^D$ and $\mathbf{F}^R$ which are conservative, drag and random forces respectively.

The governing equations for this matter are:

$$\frac{d\mathbf{r}_i}{dt} = \mathbf{v}_i \tag{2.1}$$

$$m_i \frac{d\mathbf{v}_i}{dt} = \mathbf{f}_i = \sum_{j \neq i} \left(\mathbf{F}_{ij}^C + \mathbf{F}_{ij}^D + \mathbf{F}_{ij}^R \right) \tag{2.2}$$

$$\mathbf{F}_{ij}^C = \begin{cases} a_{ij} \left(1 - \frac{r_{ij}}{r_c}\right) \hat{\mathbf{r}}_{ij} & \text{for } r_{ij} < r_c \\ 0 & \text{for } r_{ij} \geq r_c \end{cases} \tag{2.3}$$

$$\mathbf{F}_{ij}^D = -\gamma w^D(r_{ij}) \left(\hat{\mathbf{r}}_{ij} \cdot \mathbf{v}_{ij}\right) \hat{\mathbf{r}}_{ij} \tag{2.4}$$

$$\mathbf{F}_{ij}^R = \sigma w^R(r_{ij}) \theta_{ij} \hat{\mathbf{r}}_{ij} \tag{2.5}$$

$$w^D(r_{ij}) = \begin{cases} (1 - \frac{r_{ij}}{r_c})^2 & \text{for } r_{ij} < r_c \\ 0 & \text{for } r_{ij} \geq r_c \end{cases} \tag{2.6}$$

in which:

$$w^D(r) = \left[w^R(r)\right]^2 \tag{2.7}$$

In these equations, r_{ij} represents the distance between particles i and j; $\hat{\mathbf{r}}_{ij}$ is the unit vector pointing from particle j to particle i; and $\mathbf{v}_{ij} = \mathbf{v}_i - \mathbf{v}_j$ denotes the relative velocity between the two particles. σ is the amplitudes of white noise, and γ is the damping or friction coefficient, capturing the resistance a particle experiences moving through a medium.

As shown both drag and random forces depend on the weight functions $w^D(r_{ij})$ and $w^R(r_{ij})$, effecting the particle motion within the cutoff radius r_c. The repulsion parameter a_{ij} determines the strength of the repulsive potential between bead types i and j.

The fluctuation dissipation theory requires that the Brownian motion and dissipation in physical systems satistfy:

$$\sigma^2 = 2\gamma k_B T \tag{2.8}$$

Here, Boltzmann's constant is represented by k_B, and T is the absolute temperature of the system in Kelvin.

In other words, random and dissipative force together act as a thermostat to keep the system at a constant temperature when the dissipative coefficient γ and the amplitudes of white noise σ satisfy the fluctuation–dissipation theorem (Li et al. 2017). As a result, DPD works well for isothermal systems, but is not effective for systems where the temperature varies in time and position, because the total energy is not conserved in the DPD method.

Integration Scheme and Algorithm

To integrate the equations of motion, a velocity-Verlet-like scheme is employed (Groot and Warren 1997). Compared to the simple Euler algorithm, the modified velocity-Verlet algorithm improves numerical stability while accounting for the velocity dependence of the dissipative force. The integration steps are:

$$\vec{r}_i(t+\Delta t) = \vec{r}_i(t) + \Delta t\, \vec{v}_i(t) + \frac{1}{2}\Delta t^2\, \vec{f}_i(t), \tag{2.9}$$

$$\tilde{\vec{v}}_i(t+\Delta t) = \vec{v}_i(t) + \lambda\, \Delta t\, \vec{f}_i(t), \tag{2.10}$$

$$\vec{f}_i(t+\Delta t) = \vec{f}_i(\vec{r}_i(t+\Delta t), \tilde{\vec{v}}_i(t+\Delta t)), \tag{2.11}$$

$$\vec{v}_i(t+\Delta t) = \vec{v}_i(t) + \frac{1}{2}\Delta t \left(\vec{f}_i(t) + \vec{f}_i(t+\Delta t)\right), \tag{2.12}$$

where λ is an empirical factor typically set to $\lambda = 1/2$. The random force contribution requires special treatment and is implemented as:

$$\vec{F}^R_{ij} = \sigma\, w_R(r_{ij})\, \zeta_{ij}\, \Delta t^{-1/2} \hat{r}_{ij}, \tag{2.13}$$

where ζ_{ij} is a normally distributed random number. The $\Delta t^{-1/2}$ dependence ensures correct scaling of noise in time-discretized stochastic dynamics.

Timestep and Noise Amplitude Selection in DPD

The methodology for choosing the timestep size and noise amplitude in Dissipative Particle Dynamics (DPD) was developed by Groot and Warren (Groot and Warren 1997). Selecting an appropriate timestep involves balancing simulation efficiency with the requirement of

maintaining thermodynamic equilibrium. This equilibrium is monitored by evaluating the system temperature, computed from the average particle velocities via:

$$k_B T = m\frac{\langle v^2 \rangle}{3}, \tag{2.14}$$

where $\langle \cdot \rangle$ denotes the average over all particles, and $k_B T$ is set to unity in reduced units.

In their studies, simulations were performed with 4000 particles in a $10 \times 10 \times 10$ box using a repulsion parameter $a = 25$ and noise amplitude $\sigma = 3$, testing both uniform and Gaussian noise. It was found that both noise types yielded statistically identical temperature results; hence, uniform noise was preferred due to its lower computational cost.

A key observation from their work is that the timestep Δt should be selected based on the allowable artificial increase in temperature. For a Verlet-type integration scheme (Eq. (9) in their work) with $\lambda = 0.5$, a timestep of $\Delta t = 0.04$ results in only a 2% temperature increase, while $\Delta t = 0.05$ leads to a 3% increase. Therefore, $\Delta t = 0.04$ is considered a safe choice, and $\Delta t = 0.05$ an upper practical limit.

By contrast, using the Euler-type algorithm (Eq. (7)), a timestep as small as $\Delta t \approx 0.001$ would be required to achieve similar accuracy—making the Verlet algorithm roughly 50 times more efficient. Moreover, it was found that omitting the $\frac{1}{2}(\Delta t)^2 f(t)$ acceleration term from the position update leads to poor temperature control, equivalent to the Euler algorithm's performance. Including this term, even in the Euler algorithm, improves accuracy to levels comparable to the Verlet algorithm without the term. Thus, both the inclusion of this acceleration term and adoption of the Verlet scheme are essential for maintaining accuracy while using a larger timestep.

This temperature stability was confirmed (Groot and Warren 1997) for $\sigma = 3$ and $\lambda = 0.5$. When the noise amplitude was reduced (e.g., $\sigma = 1$), the system's responsiveness to temperature perturbations decreased. For example, at $\rho = 3$ and $\Delta t = 0.04$, the system relaxes exponentially from $k_B T = 10$ to $k_B T = 1$ within approximately 10 timesteps for

$\sigma = 3$, whereas for $\sigma = 1$, the relaxation time extends to 90 timesteps due to the lower friction coefficient.

Exploring the temperature behavior as a function of noise amplitude revealed that k_BT increases slowly with σ until $\sigma \approx 8$, beyond which it rises rapidly and can lead to instability. As a result, $\sigma = 3$ is recommended as a compromise value, offering fast temperature equilibration, simulation stability, and physical realism.

Furthermore, the choice of the empirical parameter λ in the Verlet-type algorithm (Eq. (9)) can influence performance. For example, with $\rho = 3$ and $\sigma = 3$, an optimal value of $\lambda = 0.65$ allows the timestep to be increased to $\Delta t = 0.06$ without significant loss of temperature control. Nonetheless, for consistency and robustness, all remaining simulations reported by Groot and Warren were conducted with $\Delta t = 0.04$ and $\lambda = 0.5$.

Thermodynamic Equilibrium and Fluctuation–Dissipation

Español and Warren demonstrated that to preserve the canonical equilibrium distribution (Gibbs-Boltzmann), the fluctuation–dissipation balance must be satisfied. They derived the associated Fokker–Planck equation for the phase-space distribution $\rho(\vec{r}_i, \vec{p}_i, t)$:

$$\frac{\partial \rho}{\partial t} = \mathcal{L}_C \rho + \mathcal{L}_D \rho, \tag{2.15}$$

where $\mathcal{L}_C$ and $\mathcal{L}_D$ represent conservative and dissipative Liouvillean operators, respectively. Equilibrium is achieved when both components of the operator annihilate the distribution, i.e., $\mathcal{L}_C \rho_{\text{eq}} = \mathcal{L}_D \rho_{\text{eq}} = 0$. If the fluctuation–dissipation relation is violated, the simulation deviates from Gibbs–Boltzmann equilibrium, potentially yielding unphysical results.

Consequences of Violating the Fluctuation–Dissipation Relation

In DPD simulations, each pair of particles experiences a dissipative force that removes kinetic energy and a random force that injects thermal energy. These two forces must be carefully

balanced through the fluctuation–dissipation relation in order to maintain thermodynamic equilibrium. If this relation is not satisfied, the simulation may not correctly reproduce the equilibrium behavior of the system.

The reason for this can be understood by examining the Fokker–Planck equation, which governs the time evolution of the probability distribution $\rho(\{\vec{r}_i, \vec{p}_i\}, t)$ in phase space:

$$\frac{\partial \rho}{\partial t} = \mathcal{L}_C \rho + \mathcal{L}_D \rho. \tag{2.16}$$

Here, $\mathcal{L}_C$ is the Liouville operator representing the conservative (Hamiltonian) part of the dynamics, and $\mathcal{L}_D$ represents the contributions from dissipative and stochastic forces.

The system is said to be in thermodynamic equilibrium when its phase-space distribution becomes stationary and takes the form of the Gibbs–Boltzmann distribution:

$$\rho_{\mathrm{eq}}(\{\vec{r}_i, \vec{p}_i\}) = \frac{1}{Z} \exp\left(-\frac{H(\{\vec{r}_i, \vec{p}_i\})}{k_B T}\right), \tag{2.17}$$

where H is the Hamiltonian of the system, k_B is Boltzmann's constant, T is the temperature, and Z is the normalization constant (the partition function).

In order for this ρ_{eq} to be a valid stationary solution of the Fokker–Planck equation, both operators must vanish when applied to it:

$$\mathcal{L}_C \rho_{\mathrm{eq}} = 0, \quad \mathcal{L}_D \rho_{\mathrm{eq}} = 0. \tag{2.18}$$

The first condition is always satisfied due to conservation laws in Hamiltonian dynamics. The second condition, however, is only satisfied if the fluctuation–dissipation relation is enforced. Specifically, the strength σ of the random force and the friction coefficient γ in the dissipative force must obey:

$$\sigma^2 = 2\gamma k_B T, \quad w_D(r) = [w_R(r)]^2, \tag{2.19}$$

where $w_D(r)$ and $w_R(r)$ are the distance-dependent weight functions for dissipative and random forces, respectively. This ensures that the stochastic and dissipative effects precisely balance in a way that leads to the correct thermal fluctuations in velocity and momentum. If these relations are violated, the dissipative and random forces no longer balance correctly. As a result, $\mathcal{L}_D \rho_{\text{eq}} \neq 0$, and the system's probability distribution will evolve away from the Gibbs–Boltzmann form, even if the simulation reaches a steady state. This leads to unphysical results: the system may not maintain a consistent temperature, and derived thermodynamic properties such as pressure, compressibility, or diffusion coefficients can become unreliable or incorrect. Therefore, maintaining the fluctuation–dissipation balance is essential for the statistical mechanical validity of DPD simulations.

2.2 Calibration of the Repulsion Parameter in DPD Simulations

In Dissipative Particle Dynamics (DPD), the conservative repulsion parameter a_{ij} is the primary parameter controlling the equation of state of the fluid. A correct choice of a ensures that the compressibility and thermodynamic fluctuations of the simulated fluid are consistent with those of the target real fluid. This is crucial for simulating soft matter systems with physically meaningful pressure and density behavior.

2.2.1 Matching Compressibility

The compressibility of a fluid characterizes how much its volume changes in response to pressure. To model this correctly in DPD, the equation of state (EOS) must yield the

correct density fluctuations. Groot and Warren (1997) derived an empirical EOS for a DPD fluid with soft repulsion:

$$p = \rho k_B T + 0.101\, a\, \rho^2, \tag{2.20}$$

where p is pressure, ρ is number density, k_B is Boltzmann's constant, and T is temperature. The first term represents the ideal gas contribution, while the second term accounts for interactions between particles.

The dimensionless inverse compressibility is defined as:

$$\Pi = \frac{1}{\rho k_B T \kappa_T} = 1 + 0.2\, \frac{a\rho}{k_B T}, \tag{2.21}$$

where κ_T is the isothermal compressibility. For example, liquid water at room temperature ($T \approx 300$ K) has $\Pi \approx 15.98$. Plugging this into Eq. 2.21 gives:

$$0.2 \cdot \frac{a\rho}{k_B T} \approx 14.98 \quad \Rightarrow \quad \frac{a\rho}{k_B T} \approx 75.$$

Therefore, for a DPD fluid with $\rho = 3$, a good choice for the repulsion parameter is $a \approx 25\, k_B T$. This calibration ensures that the DPD fluid mimics the compressibility of water. For other densities, a can be scaled accordingly: for instance, $a \approx 15$ at $\rho = 5$.

2.2.2 Mapping to Flory–Huggins Theory in Mixtures

In multi-component systems, the difference in repulsion between unlike and like particles governs the mixing behavior. When $a_{AA} = a_{BB}$ and $a_{AB} > a_{AA}$, the mixture tends to phase-separate. This effect can be quantified through an effective Flory–Huggins χ parameter.

Groot and Warren (Groot and Warren (1997)) established a linear relationship between the repulsion difference $\Delta a = a_{AB} - a_{AA}$ and the Flory–Huggins parameter χ. For a system with number density $\rho = 3$, the relation is:

$$\chi \approx 0.286\,\Delta a. \tag{2.22}$$

At higher densities, this slope changes slightly (e.g., $\chi \approx 0.689\,\Delta a$ at $\rho = 5$), but Eq. 2.22 holds well for moderately segregating systems ($\chi \gtrsim 3$). This means that to model a binary mixture with $\chi = 5$, one should use $\Delta a \approx 17.5$.

2.2.3 Summary of Practical Guidelines

- Choose the number density ρ (commonly $\rho = 3$ for efficiency and thermodynamic accuracy).
- Set $a \approx 25$ (in DPD units) to match water-like compressibility at $\rho = 3$.
- For mixtures, determine $\Delta a = a_{AB} - a_{AA}$ using Eq. 2.22 to reflect the desired χ value.

This calibration strategy ensures that DPD simulations capture both the bulk thermodynamic behavior and the phase behavior of real systems, in line with continuum theories like Flory–Huggins.

2.2.4 Advantages of DPD and Soft Potentials

DPD's soft conservative forces enable the use of larger integration time steps compared to conventional molecular dynamics with Lennard-Jones potentials. The particles represent coarse-grained fluid elements rather than atoms, and their interactions are smoother and shorter ranged. This makes DPD especially suited for studying large-scale behavior of complex fluids, including polymer solutions, surfactants, and mesoscale phase transitions.

Moreover, DPD conserves momentum and includes hydrodynamic interactions intrinsically, giving it an advantage over diffusive-only methods like Monte Carlo or density functional theory when simulating flow, defect annealing, or phase ordering dynamics.

In this work, we use DPD as a base for energy-conserving extensions (DPDE), allowing the study of heat-transfer processes in soft matter systems.

One might ask why DPD is needed if other methods can simulate canonical ensembles. DPD can indeed be interpreted as a novel thermostat, but unlike purely diffusive techniques (e.g., dynamic density functional theory) or Monte Carlo methods, it also preserves hydrodynamics. Hydrodynamic effects can be essential in many mesoscale processes, such as the annealing of defects in ordered mesophases, making DPD uniquely valuable for such systems.

Compared to traditional molecular dynamics using, for example, Lennard-Jones potentials, DPD has the advantage of employing soft repulsive forces $\vec{F}^C$, which allow for significantly larger time steps. DPD particles represent fluid elements or coarse-grained molecular units rather than individual atoms, making the method efficient for mesoscopic simulations.

The question of how to relate atomistic and mesoscopic parameters is addressed in the following sections. While soft potentials could be used in standard MD or Monte Carlo approaches (with noise and friction turned off, i.e., $\sigma = \gamma = 0$), a bottom-up approach has been proposed by Forrest and Suter. They began with atomistic Lennard-Jones potentials and derived effective interactions between molecular centers of mass by averaging over fast atomic fluctuations.

Their effective potentials resemble the soft DPD force law (Eq. 2.3): they do not diverge at $r = 0$ and lack the characteristic minimum of the Lennard-Jones potential. This supports the use of soft repulsive interactions in DPD. However, their approach has some limitations. The computation of "time-averaged" potentials requires complex integrals similar to virial

coefficient calculations and yields no analytical form. Additionally, their method ignores time-dependent density correlations, which can be significant.

Because of these complexities, a more practical top-down strategy is adopted here. Rather than deriving interaction forces from atomistic models, DPD parameters are chosen to reproduce correct thermodynamic behavior at the mesoscopic scale. Length and mass scales are fixed by setting particle mass and cutoff distance to 1. We also choose simulation units such that $k_B T = 1$, setting the thermal velocity scale via the Maxwell–Boltzmann distribution.

With these units, conservative force parameters are naturally scaled by thermal energy, simplifying both parameterization and physical interpretation.

2.3 Parametrization of DPD Models

The conservative force in DPD is given by:

$$\vec{F}_{ij}^{C} = a_{ij} \left(1 - \frac{r_{ij}}{r_c}\right) \hat{r}_{ij}, \quad \text{for } r_{ij} < r_c \tag{2.23}$$

Here, a_{ij} is the repulsion parameter and r_c is the cutoff distance.

2.3.1 Compressibility-Based Estimation of a_{ii}

For a single-component fluid, a_{ii} can be estimated from the compressibility:

$$\kappa_T^{-1} = \rho \left(\frac{\partial P}{\partial \rho}\right)_T \approx a_{ii}\rho \tag{2.24}$$

2.3.2 Heterogeneous Repulsion via Flory–Huggins Parameter

For mixtures, the Flory–Huggins parameter χ_{ij} can be used to estimate cross-interactions:

$$a_{ij} = a_{ii} + 3.27\chi_{ij} \tag{2.25}$$

The parameter χ_{ij} can be obtained from:

$$\chi_{ij} = \frac{V_{\text{ref}}}{RT}(\delta_i - \delta_j)^2 \tag{2.26}$$

where δ_i and δ_j are solubility parameters of the components i and j, respectively, and V_{ref} is a chosen reference volume.

2.3.3 Thermodynamic Matching of κ_{ij} & a_{ij}

The parameter κ_{ij} relates to the stiffness of the system and can be approximated as:

$$\kappa_{ij} = \frac{a_{ij}}{\rho} \tag{2.27}$$

This serves to match the bulk modulus or compressibility of the modeled system.

2.4 Energy-Conserving Dissipative Particle Dynamics (DPDe) for Heat Transfer

In classical Dissipative Particle Dynamics (DPD), the system is maintained at a fixed temperature by a thermostat composed of dissipative and random forces. However, this method does not conserve total energy, making standard DPD suitable only for isothermal simulations (Groot and Warren (1997)). To overcome this limitation, the energy-conserving extension known as DPDe (or eDPD) was developed (Ripoll et al. 1998). In DPDe, each coarse-grained particle (or bead) is treated as a small thermodynamic subsystem characterized not only by its position $\mathbf{r}_i$ and momentum $\mathbf{p}_i$, but also by an internal energy variablee_i.

Thus, each DPDe particle behaves as a local equilibrium system with its own temperature T_i and internal energy $e_i = C_v T_i$, where C_v is the specific heat in constant volume. This internal energy evolves through interactions with neighboring particles, allowing simulation of temperature gradients and heat transfer at the mesoscale.

2.4.1 Governing Equations

The evolution of each particle is governed by stochastic differential equations that conserve both momentum and energy:

$$\frac{d\mathbf{r}_i}{dt} = \mathbf{v}_i, \tag{2.28}$$

$$\frac{d\mathbf{v}_i}{dt} = \frac{1}{m} \sum_{j \neq i} \left(\mathbf{F}_{ij}^C + \mathbf{F}_{ij}^D + \mathbf{F}*_{ij}^R \right), \tag{2.29}$$

$$C_v \frac{dT_i}{dt} = \sum_{j \neq i} \left(q_{ij}^C + q_{ij}^V + q_{ij}^R \right). \tag{2.30}$$

The forces are decomposed into conservative, dissipative, and random components:

$$\mathbf{F}_{ij}^C = \alpha_{ij}(T)\, \omega^C(r_{ij})\, \mathbf{e}_{ij}, \tag{2.31}$$

$$\mathbf{F}_{ij}^D = -\gamma_{ij}\, \omega^D(r_{ij}) (\mathbf{e}_{ij} \cdot \mathbf{v}_{ij})\, \mathbf{e}_{ij}, \tag{2.32}$$

$$\mathbf{F}_{ij}^R = \sigma_{ij}\, \omega^R(r_{ij})\, \xi_{ij}\, \mathbf{e}_{ij}, \tag{2.33}$$

where $\mathbf{v}_{ij} = \mathbf{v}_i - \mathbf{v}_j$, $r_{ij} = |\mathbf{r}_i - \mathbf{r}_j|$, and $\mathbf{e}_{ij} = (\mathbf{r}_i - \mathbf{r}_j)/r_{ij}$. The weight functions $\omega^C(r)$, $\omega^D(r)$, and $\omega^R(r)$ vanish at the cutoff radius r_C, ensuring short-range interactions.

2.4.2 Heat Exchange Mechanisms; Connection Between Collisional Heat Flux and Macroscopic Thermal Conductivity

The LAMMPS documentation and the paper on which it is based (Li et al. 2014), state that the energy flow from bead j to bead i based on collision is given by:

$$q_i^C = \sum_{j \neq i} k_{ij}\, \omega_{CT}(r_{ij}) \left(\frac{1}{T_i} - \frac{1}{T_j} \right)$$

To relate the mesoscopic collisional heat flux used in energy-conserving DPD (eDPD) simulations to the macroscopic thermal conductivity observed in experiments, we begin with Fourier's law for heat conduction:

$$\mathbf{J_Q} = -\kappa\, \nabla T \tag{2.34}$$

where $\mathbf{J_Q}$ is the heat flux density (units: $\mathrm{J}/(\mathrm{m}^2 \cdot \mathrm{s})$) and κ is the thermal conductivity (units: $\mathrm{J}/(\mathrm{K} \cdot \mathrm{m} \cdot \mathrm{s})$). From dimensional analysis:

$$[\mathbf{J_Q}] = \frac{\mathrm{J}}{\mathrm{m}^2 \cdot \mathrm{s}} = [\kappa] \cdot [\nabla T] = [\kappa] \frac{^\circ\mathrm{K}}{m}$$

$$[\kappa] = \frac{\mathrm{J}}{^\circ\mathrm{K} \cdot \mathrm{m} \cdot \mathrm{s}}$$

In particle-based models such as eDPD, the heat flux between particles i and j is expressed approximately as:

$$\dot{q}_{ij} \approx l^2 \mathbf{J_Q} = K_{ij} \left(\frac{1}{T_i} - \frac{1}{T_j} \right) = K_{ij} \cdot \frac{T_j - T_i}{T_i T_j} \tag{2.35}$$

Comparing the right hand side of equation 2.35, to 2.34, one can consider

$$\kappa \sim \frac{\kappa_{ij}}{T_i T_j} l$$

in order to get detailed balance we require:

$$\frac{\partial \kappa}{\partial E_i} = \frac{\partial \kappa}{\partial E_j}$$

based on (Ripoll et al. 1998; Espanol 1997), we can replace:

$$T_i T_j \sim (\frac{(T_i + T_j)}{2})^2$$

so that:

$$\mathbf{J_Q} = -\kappa_{ij} \cdot \frac{4}{\ell (T_i + T_j)^2} \left(-\frac{T_j - T_i}{\ell} \right) \approx -\kappa \cdot \nabla T$$

So,

$$\kappa_{ij} = \ell \cdot \frac{(T_i + T_j)^2}{4} \cdot \kappa$$

This is a bit qualitative. Mackie ((Mackie et al. 1999)) makes this a bit more rigorous — their Equation 2.15 needs:

$$\dot{q}_{ij}^{(q)} = L_{ij}^{(q)} \left(\frac{1}{\theta_i} - \frac{1}{\theta_j} \right) \quad \text{and} \quad \left[L_{ij}^{(q)} \right] = \frac{\mathrm{J}}{\mathrm{K} \cdot \mathrm{s}}$$

$$L_{ij}^{(q)} = \theta_i \theta_j \, \lambda_{ij} \quad \text{((Mackie et al. 1999) Eq. 2.19)}$$

where θ_i is the temperature.

$$\lambda_{ij} = L_0^{(q)} \cdot \frac{1}{\theta_i \theta_j} \left(1 - \frac{r_{ij}^2}{r_\lambda^2} \right) \quad \text{((Mackie et al. 1999) Eq. 3.25)}$$

Then they did an analytic calculation to connect this to the macroscopic thermal conductivity:

$$\lambda = \kappa = \frac{2\pi}{315} \cdot \frac{\rho^2}{T^2} \cdot L_0^{(q)} \cdot r_\lambda^5$$

Let's check that this is what we think it is.

Recall that the units of thermal conductivity are:

$$[\kappa] = \frac{J}{\mathrm{m} \cdot \mathrm{s} \cdot \mathrm{K}}$$

Then,

$$\frac{J}{\mathrm{m} \cdot \mathrm{s} \cdot \mathrm{K}} = \left[\frac{\rho^2 \cdot r^5}{T^2}\right] \cdot \left[L_0^{(q)} = \frac{1}{m^6} \frac{1}{^\circ K^2} m^5 L_0^{(q)}\right]$$

If we break down the units of $L_0^{(q)}$, we expect:

$$\left[L_0^{(q)}\right] = \frac{J \cdot \ ^\circ K}{s}$$

Which agrees! Then given a macroscopic κ, the LAMMPS κ_{ij} is the same as $L_0^{(q)}$ and:

$$\kappa_{ij} = \frac{T^2\, r_\lambda^5}{\rho^2} \kappa \qquad \text{or} \qquad \kappa_{ij} = \frac{(T_i + T_j)^2}{4} \cdot \frac{r_\lambda^5}{\rho^2} \cdot \kappa$$

Where κ here is the conventional macroscopic thermal conductivity.

Unfortunately, LAMMPS states in the "edpd" pair style documentation:

$$k_{ij} = \frac{C_v^2}{k_B} \cdot \kappa \cdot \left(\frac{T_i + T_j}{2}\right)^2$$

The factor of C_v^2 is confusing! First it does not follow from a microscopic derivation. Second, if we have two dissimilar beads, it is not clear which C_v we should use to calculate the heat transfer between them. Let's call this $\tilde{k}_{ij}$ to keep it straight. Then, according to LAMMPS:

$$[\dot{q}] = \left[\frac{J}{s}\right] = \left[C_v \cdot \frac{dT}{dt}\right] = [C_v] \cdot \left[\frac{^\circ K}{s}\right]$$

So,

$$[C_v] = \frac{J}{K} \quad \text{(thermal capacitance of a bead)}$$

But again, from the LAMMPS documentation:

$$[\dot{q}^c] = [\tilde{k_{ij}}] \cdot [\omega(r_{ij})] \cdot \left[\frac{1}{T_i} - \frac{1}{T_j}\right]$$

$$\frac{J}{s} = [\tilde{k_{ij}}] \cdot (1) \cdot K^{-1}$$

So that:

$$[\tilde{\kappa}_{ij}] = \frac{J \cdot K}{s}$$

But from above:

$$[\tilde{\kappa}_{ij}] = [C_v^2] \cdot [\kappa] \cdot \left[(T_i + T_j)^2\right] \cdot \frac{1}{[k_B]}$$

Substituting dimensions:

$$= \left(\frac{J}{K}\right)^2 \cdot \left(\frac{J}{K \cdot m \cdot s}\right) \cdot K^2 \cdot \frac{1}{J/K} = \frac{J^2}{K^2} \cdot \frac{J}{K \cdot m \cdot s} \cdot K^2 \cdot \frac{K}{J}$$

Simplifying:

$$= J \cdot K \cdot \frac{J}{K \cdot m \cdot s} = \frac{J^2}{m \cdot s}$$

Thus:

$$[\tilde{\kappa}_{ij}] = \frac{J \cdot K}{s}$$

So, surprisingly:

$$[\kappa] = \frac{1}{s} \quad (?!) \quad (\text{Recall: } [\kappa] = \frac{J}{K \cdot m \cdot s})$$

However, the LAMMPS documentation refers to this $\tilde{\kappa}$ as the "mesoscopic heat friction," which is not clearly defined. So, let us call this LAMMPS coefficient $\tilde{\kappa}_{ij}$ and consult the references for clarification.

This is from Li et al., which points to four other references. That is, it states:

$$k_{ij} = C_v \cdot \kappa \cdot \frac{(T_i + T_j)^2}{4k_B}$$

without any proof. It examines a single fluid or bead type, so there is no ambiguity about which C_v to use.

In that paper, η is used for the thermal conductivity, and it is stated that:

$$\eta = \frac{2\pi}{315} \cdot \frac{\rho^2}{k_B} \cdot C_v^2 \cdot r_c^5 \cdot \tilde{\kappa} \quad \text{(Eq. 14, (Li et al. 2014))}$$

Let's check the units:

We now verify the units of the macroscopic thermal conductivity η from Li et al.'s formulation:

$$[\eta] = [\rho^2] \cdot [C_v^2] \cdot [r_c^5] \cdot [\tilde{\kappa}] \cdot \frac{1}{[k_B]}$$

Substituting units:

$$= \left(\frac{1}{\mathrm{m}^6}\right) \cdot \left(\frac{J}{K}\right)^2 \cdot \mathrm{m}^5 \cdot \left(\frac{J \cdot K}{s}\right) \cdot \left(\frac{1}{J/K}\right)$$

Simplifying:

$$= \frac{1}{\mathrm{m}} \cdot \frac{J^2}{K^2} \cdot \frac{J \cdot K}{s} \cdot \frac{K}{J} = \frac{J}{\mathrm{m} \cdot \mathrm{s} \cdot \mathrm{K}} = [\kappa]$$

$$\Rightarrow \eta \text{ has the correct units of thermal conductivity.}$$

which confirms the consistency of units for macroscopic thermal conductivity.

Viscous heat flux (q^V) accounts for the conversion of kinetic energy to internal energy via friction and stochastic forces. This term is carefully constructed to ensure the conservation of energy.

$$q_i^V = \frac{1}{2C_v} \sum_{j \neq i} \left\{ \omega_D(r_{ij}) \left[\gamma_{ij} (\mathbf{e}_{ij} \cdot \mathbf{v}_{ij})^2 - \frac{\sigma_{ij}^2}{m} \right] - \sigma_{ij}\, \omega_R(r_{ij}) (\mathbf{e}_{ij} \cdot \mathbf{v}_{ij})\, \zeta_{ij} \right\}, \tag{2.36}$$

Random heat flux (q^R) represents stochastic thermal energy exchange:

$$q_i^R = \sum_{j \neq i} \beta_{ij}\, \omega_T^R(r_{ij})\, \zeta_{ij}, \tag{2.37}$$

where ζ_{ij} are symmetric Gaussian noise terms with $\langle \zeta_{ij} \zeta_{kl} \rangle = \delta_{ik}\delta_{jl}\, \delta(t - t')$.

2.4.3 Fluctuation–Dissipation Consistency

To ensure thermal equilibrium and detailed balance, the dissipative and random terms must satisfy fluctuation–dissipation relations:

$$\sigma_{ij}^2 = 4\gamma_{ij} k_B \frac{T_i T_j}{T_i + T_j}, \tag{2.38}$$

$$\omega^D(r) = [\omega^R(r)]^2, \tag{2.39}$$

$$\beta_{ij}^2 = 2k_B k_{ij}. \tag{2.40}$$

These conditions ensure that the system naturally equilibrates to the Maxwell–Boltzmann distribution and that energy exchange between internal and kinetic modes occurs without drift.

2.4.4 Practical Parameter Choices

To reproduce physical thermal transport properties, k_{ij} is typically defined as:

$$k_{ij} = \frac{C_v^2 \kappa (T_i + T_j)^2}{4k_B}, \tag{2.41}$$

where κ is a mesoscopic thermal conductivity (Li et al. 2017).

2.4.5 Applications and Summary

DPDe enables simulations of non-isothermal processes such as heat conduction, temperature equilibration, and natural convection. It bridges molecular dynamics and continuum heat transfer by conserving total energy and resolving mesoscopic temperature variations. The method has been validated to reproduce Fourier's law and accurate thermodynamic fluctuations in equilibrium.

2.5 Timestep Selection for eDPD Simulations

One of the advantages of Dissipative Particle Dynamics (DPD) over traditional molecular dynamics (MD) is its ability to employ larger time steps while maintaining numerical stability and physical accuracy. However, because DPD integrates stochastic differential equations, the choice of the time step Δt must still be made carefully to ensure that the system remains thermodynamically consistent and does not experience numerical instability. At the theoretical level, the evolution of the one-particle distribution function in DPD can be analyzed by examining its first and second moments. In the absence of conservative forces, and assuming a Gibbs equilibrium distribution for particle momenta, it has been shown that the second moment of the distribution evolves according to:

$$\Delta\langle p^2 \rangle = -2\gamma \Delta t \, k_B T \, n \langle w_D^2 \rangle + \sigma^2 \Delta t \langle w_R^2 \rangle + \mathcal{O}(\Delta t^2) \tag{2.42}$$

Here:

- γ: Dissipative force coefficient
- σ: Amplitude of the random force
- n: Number density
- $\langle w_D^2 \rangle, \langle w_R^2 \rangle$: Moments of the weight functions

At equilibrium and in the limit $\Delta t \to 0$, the fluctuation-dissipation theorem (FDT) ensures consistency:

$$\sigma^2 = 2\gamma k_B T \tag{2.43}$$

For finite timesteps, the effective kinetic temperature T increases with Δt, as described by the relation:

$$m k_B T = \frac{A_3}{A_1(2 - A_1 n \Delta t) - A_2 \Delta t} \tag{2.44}$$

with:

$$A_1 = \gamma \langle w_D^2 \rangle \tag{2.45}$$

$$A_2 = \frac{2\gamma^2}{m} \langle w_D^2 \rangle \tag{2.46}$$

$$A_3 = \sigma^2 \langle w_R^2 \rangle = 2\gamma k_B T \langle w_D^2 \rangle \tag{2.47}$$

This expression becomes undefined if the denominator becomes negative. Thus, the timestep must remain below the critical value:

$$\Delta t_c = \frac{2A_1}{n A_1^2 + A_2} \tag{2.48}$$

Substituting the definitions of A_1 and A_2, we obtain:

$$\Delta t_c = \frac{2\gamma\langle w_D^2\rangle}{n\gamma^2\langle w_D^2\rangle^2 + \frac{2\gamma^2}{m}\langle w_D^2\rangle} \tag{2.49}$$

Simplifying:

$$\Delta t_c = \frac{2}{\gamma} \cdot \frac{1}{n\langle w_D^2\rangle + \frac{2}{m}} \tag{2.50}$$

Numerical Example from Simulation Input

From the simulation input file, the eDPD parameters can be defined using the following command:

```
pair_coeff 1 1 25 4.5 0.41 1.58 1.41E-5 2.0 1.58
```

The above pair-coeff command is an example that specifies the interaction between type 1 particles, where:

- $a_{ij} = 25$ is the conservative force coefficient, representing soft repulsion between particles,
- $\gamma_{ij} = 4.5$ is the dissipative force coefficient, controlling viscous damping,
- $s = 0.41$ is the exponent in the weight function $\omega_D(r) = \omega_R^2(r) = \left(1 - \frac{r}{r_c}\right)^s$, which defines how the dissipative and random force magnitudes decay with distance. A smaller value of s results in a more gradual decay, influencing how momentum and energy are exchanged between particles as a function of separation distance.
- $r_c = 1.58$ is the cutoff radius for conservative, dissipative, and random forces,
- $\kappa_{ij} = 1.41 \times 10^{-5}$ is the thermal conductivity coefficient, governing the rate of internal energy exchange between particles,
- $s_T = 2.0$ is the exponent used in the thermal weight function $\omega_{CT}(r) = \omega_{RT}^2(r) = \left(1 - \frac{r}{r_{ct}}\right)^{s_T}$, which controls how the heat conduction term decays with distance between

particles. This parameter influences the spatial distribution of thermal interactions, with higher values leading to more localized heat transfer near the cutoff radius r_{ct}.

- $r_{ct} = 1.58$ is the cutoff radius used in the weighting function for thermal energy exchange.

These parameters together define the mechanical and thermal interactions in the system, ensuring correct momentum and energy transfer consistent with the fluctuation–dissipation theorem and the conservation of total energy in eDPD simulations.

Calculation of $\langle w_D^2 \rangle$

Symbol	Meaning	Value
a	repulsion parameter	25
σ	Random force amplitude (noise) computed from FDT	3.77
γ	Dissipative force coefficient	4.5
s or `power_f`	Exponent in the weight function $(1 - r/r_c)^s$	0.41
r_c	Cutoff radius for force interactions	1.58
κ	Thermal conductivity coefficient	1.42×10^{-5}
`power_T`	Exponent in temperature-dependent thermal conductivity	2.0
$r_{c,T}$	Cutoff radius for thermal interactions	1.58

Table 2.1 Corrected eDPD parameters used in the simulation.

The average squared weight function is computed in the following way. We previously used:

$$\langle w_D^2 \rangle = \frac{3}{r_c^3} \int_0^{r_c} r^2 \left(1 - \frac{r}{r_c}\right)^{2s} dr$$

With the substitution $x = \frac{r}{r_c}$, we get:

$$\langle w_D^2 \rangle = \frac{3}{r_c^3} \cdot r_c^4 \int_0^1 x^2 (1-x)^{2s} \, dx = 3 r_c \int_0^1 x^2 (1-x)^{2s} \, dx$$

This integral is a Beta function:

$$\int_0^1 x^2(1-x)^{2s}\,dx = B(3, 2s+1) = \frac{\Gamma(3)\Gamma(2s+1)}{\Gamma(2s+4)}$$

Thus:

$$\langle w_D^2 \rangle = 3r_c \cdot \frac{\Gamma(3)\Gamma(2s+1)}{\Gamma(2s+4)}$$

$$\langle w_D^2 \rangle = 3r_c \int_0^1 x^2(1-x)^{2s} dx = 3r_c \cdot B(3, 2s+1) = 3r_c \cdot \frac{\Gamma(3)\Gamma(2s+1)}{\Gamma(2s+4)} \approx 0.484$$

The random force amplitude σ is calculated from the following formula:

$$\sigma^2 = \frac{4\gamma k_B T_i T_j}{T_i + T_j} \Rightarrow \sigma \approx 3.77$$

$$A_1 = \gamma \langle w_D^2 \rangle = 4.5 \cdot 0.484 = 2.18$$

$$A_2 = \frac{2\gamma^2}{m} \langle w_D^2 \rangle = 2 \cdot 4.5^2 \cdot 0.484 \approx 19.58$$

$$A_3 = \sigma^2 \langle w_D^2 \rangle = (3.77)^2 \cdot 0.484 \approx 6.88$$

The critical time step is:

$$\Delta t_c = \frac{2A_1}{A_2(n+1)} = \frac{2 \cdot 2.18}{19.58 \cdot 4} \approx 0.0556$$

$$\boxed{\Delta t_c \approx 0.0556}$$

The simulation currently uses $\Delta t = 0.0005$, which is safely below the stability threshold and consistent with recommendations for eDPD simulations with conservative forces and energy transport.

In general one should notice that for a given set of input parameters of DPD $(\gamma, \sigma, w_D, w_R, n)$, the measured temperature of the system increases as the time step Δt becomes larger. Moreover, $\frac{1}{k_B T}$ is found to be a linearly monotonic function of Δt.

One standard way to measure the equilibrium temperature is through the averaged kinetic energy of particles. According to the equipartition theorem, the temperature can be estimated as:

$$k_B T = m \, \frac{\langle v^2 \rangle}{3}$$

where $\langle v^2 \rangle$ is the average of the squared velocities of the particles. Therefore, as Δt increases, this kinetic temperature deviates from the input target temperature due to numerical integration artifacts.

We set the number density to $\rho = 3$. This means that there are 3 DPD particles per unit volume in DPD units. To match this to the molecular density of liquid water, we calculate the physical length scale $[L]$ as follows:

Step 1: Real Water Number Density

At 300 K, the density of liquid water is:

$$\rho_{\text{mass}} = 997 \, \text{kg/m}^3$$

The molar mass of water is:

$$M = 18.015 \, \text{g/mol} = 0.018015 \, \text{kg/mol}$$

The number of moles of water per cubic meter is:

$$\rho_{\text{mol}} = \frac{997}{0.018015} \approx 55371 \, \text{mol/m}^3$$

Using Avogadro's number $N_A = 6.022 \times 10^{23}$, the number of water molecules per cubic meter is:

$$\rho_{\text{water molecules}} = 55371 \times 6.022 \times 10^{23} \approx 3.34 \times 10^{28} \,\text{molecules/m}^3$$

Step 2: DPD Number Density and Length Scale

In DPD, the number density is:

$$\rho_{\text{DPD}} = \frac{N_{\text{DPD}}}{[L]^3} = \frac{3}{[L]^3}$$

We want this to match the molecular number density of real water:

$$\frac{3}{[L]^3} = 3.34 \times 10^{28} \quad \Rightarrow \quad [L]^3 = \frac{3}{3.34 \times 10^{28}}$$

$$[L]^3 \approx 8.98 \times 10^{-29} \quad \Rightarrow \quad [L] \approx \left(8.98 \times 10^{-29}\right)^{1/3} \approx 4.48 \times 10^{-10}\,\text{m} = 0.448\,\text{nm}$$

Final Answer

$$\boxed{[L] = 0.448\,\text{nm}}$$

This is the physical length scale that ensures one DPD particle corresponds to three water molecules when the number density is $\rho = 3$.

Determining the Repulsion Parameter a from Compressibility

At high number densities ($\rho > 2$), the pressure of a DPD fluid can be approximated using the virial theorem as:

$$p = \rho k_B T + \alpha a \rho^2$$

where:

- ρ is the DPD number density (particles per unit volume),
- $k_B T$ is the thermal energy,
- a is the repulsion parameter (strength of conservative force),
- $\alpha \approx 0.101$ is a numerical prefactor determined from simulation data.

To connect this with thermodynamic properties, the (dimensionless) isothermal compressibility of a DPD fluid is defined as:

$$\kappa_c^{-1} = \frac{1}{k_B T} \left(\frac{\partial p}{\partial \rho} \right)$$

Taking the derivative of pressure:

$$\frac{\partial p}{\partial \rho} = k_B T + 2\alpha a \rho \quad \Rightarrow \quad \kappa_c^{-1} = 1 + \frac{2\alpha a \rho}{k_B T}$$

Solving for a, we obtain:

$$a = \frac{k_B T(\kappa_c^{-1} - 1)}{2\alpha \rho}$$

Matching to Real Water

To match the DPD fluid to the compressibility of real water at 300 K, we use:

- Isothermal compressibility: $\beta_T = 4.503 \times 10^{-10}\,\mathrm{m}^2/\mathrm{N}$,
- Thermal energy: $k_B T = 4.142 \times 10^{-21}\,\mathrm{J}$,
- DPD number density: $\rho = 3$,
- Length scale: $[L] = 0.448\,\mathrm{nm} = 4.48 \times 10^{-10}\,\mathrm{m}$.

The dimensionless compressibility of the DPD system is given by:

$$\kappa_c = \rho k_B T \beta_T / [L]^3 \quad \Rightarrow \quad \kappa_c^{-1} = \frac{[L]^3}{\rho k_B T \beta_T}$$

Substituting the given values:

$$[L]^3 = (4.48 \times 10^{-10})^3 = 8.98 \times 10^{-29}\,\mathrm{m}^3$$

$$\kappa_c^{-1} = \frac{8.98 \times 10^{-29}}{3 \cdot 4.142 \times 10^{-21} \cdot 4.503 \times 10^{-10}} \approx 16.0$$

Using this in the earlier equation for a:

$$a = \frac{4.142 \times 10^{-21} \cdot (16.0 - 1)}{2 \cdot 0.101 \cdot 3} = \frac{4.142 \times 10^{-21} \cdot 15}{0.606} \approx \frac{62.13 \times 10^{-21}}{0.606}$$

To express a in DPD units, divide by $k_B T$:

$$\frac{a}{k_B T} = \frac{15}{2\alpha\rho} = \frac{15}{2 \cdot 0.101 \cdot 3} \approx \boxed{\frac{75.0}{\rho}}$$

Final Result

The repulsion parameter is:

$$\boxed{a = \frac{75.0\, k_B T}{\rho}}$$

This value of a ensures that the DPD system has the same compressibility as liquid water at 300 K when the number density is $\rho = 3$ and the coarse grain length scale is $[L] = 0.448$ nm.

It is important to remember that if you change the level of coarse graining (that is, the number of molecules per DPD particle) or change the value of $[L]$, you must recompute a accordingly. Otherwise, the compressibility and sound speed of the fluid will no longer match the physical system.

Relation Between Dissipative Coefficient, Weight Function, and Viscosity

In Dissipative Particle Dynamics (DPD), the viscosity of the simulated fluid arises from two main sources: the dissipative interactions between particles and the diffusive motion of particles themselves. Both contributions are influenced by how energy and momentum are exchanged in the system.

The *dissipative force* acts as a frictional interaction between pairs of particles and is proportional to a coefficient γ and a spatial weighting function $w_D(r)$, which determines how strongly particles interact based on their separation distance. When particles move relative to each other, this dissipative force resists their motion and transfers momentum in a way that mimics viscous behavior.

The combined effect of the dissipative coefficient γ and the shape of the weight function $w_D(r)$ directly controls how much resistance the fluid exhibits to shear flow. As a result, these parameters play a central role in setting the *shear viscosity* of the fluid. For example:

- Increasing γ generally increases the viscosity, as it amplifies friction between particles.
- Choosing a broader or sharper $w_D(r)$ changes the range and strength of dissipation across different distances, also affecting the viscosity.

Additionally, because particles in DPD also undergo random motion, the relaxation of their velocities (which is controlled by γ and $w_D(r)$) contributes to viscosity through kinetic effects. Altogether, by tuning γ and the functional form of $w_D(r)$, one can match the viscosity of the DPD model to that of a real fluid of interest.

The total viscosity is given by the sum of the dissipative and kinetic contributions:

$$\eta = \eta_D + \eta_K$$

where:

- The *dissipative contribution* is

$$\eta_D = \frac{2\pi\gamma\rho^2}{15}\int_0^\infty dr\, r^4 w_D(r)$$

- The *kinetic contribution* is

$$\eta_K = \frac{\rho k_B T \tau}{m} \quad \text{with} \quad \frac{1}{\tau} = 4\pi\gamma\rho\int_0^\infty dr\, r^2 w_D(r)$$

Both contributions depend explicitly on γ, ρ, and the integrals over the weight function $w_D(r)$. These expressions allow direct control of the fluid's viscosity by adjusting simulation parameters.

2.6 Summary

In this chapter, we presented the theoretical foundations of Dissipative Particle Dynamics (DPD) and the Energy-Conserving Dissipative Particle Dynamics (eDPD) method. We described how the conservative, dissipative, and random forces are constructed to satisfy the fluctuation-dissipation theorem and maintain thermodynamic consistency. The stability conditions were analyzed through the evaluation of characteristic coefficients (A_1, A_2, and A_3), and a critical timestep was derived to ensure numerical accuracy. We also explored how the kinetic temperature depends on integration timestep, emphasizing the importance of choosing Δt well below the stability threshold. Furthermore, the DPD repulsion parameter a was derived from compressibility matching with real water at 300 K, and the coarse-graining length scale was determined using number density conversion from molecular to DPD units. Finally, we discussed how the dissipative coefficient γ and weight function $w_D(r)$ influence the fluid's viscosity and transport properties.

This theoretical framework forms the basis of the mesoscopic model used in the following chapters. In particular, Chapter 3 builds upon this foundation by detailing the coarse-

graining strategy and parameterization of single-walled carbon nanotubes (SWCNTs) and DSPE molecules. The modeling decisions in Chapter 3 rely critically on the physical consistency and numerical reliability established through the theory in this chapter.

Chapter 3

Coarse-Grained Model Development and Simulation Setup

3.1 Introduction

In this chapter, we describe the development and parameterization of coarse-grained models for single-walled carbon nanotubes (SWCNTs), DMPC lipid molecules, and DSPE-PEG conjugates in water. These components form the foundation of our simulations aimed at understanding the thermal, mechanical, and interfacial behavior of functionalized carbon nanotubes in biologically relevant environments.

As discussed in chapter two, at the mesoscopic scale, fully atomistic simulations become computationally expensive and often impractical for studying large systems over long timescales. Coarse-grained models, such as those based on dissipative particle dynamics (DPD) and energy-conserving DPD (eDPD), offer a powerful alternative by representing groups of atoms as single beads. These models preserve essential structural and thermodynamic properties while allowing for efficient simulation of collective phenomena such as dispersion, adsorption, and heat transfer.

In the following sections, we will first describe the general simulation parameters used in our system: parameters such as the time step, temperature, and interaction range.

We then continue by constructing a triangulated bead-spring model of the SWCNT based on a hexagonal lattice, with bond lengths and angles designed to replicate the mechanical rigidity of real nanotubes. To guide our approach, we followed the method developed by Aitor Valdivia and Carlos Jaime (Valdivia and Jaime 2021), who proposed a practical way to represent SWCNTs in coarse-grained simulations. Their method uses a triangular lattice pattern to construct the surface of the nanotube, which helps to maintain its shape and prevent unwanted gaps that water beads could penetrate. The mechanical reliability of the SWCNT model is verified by computing stress/strain responses and comparing them to known values from atomistic simulations and experimental literature. We also model water as a DPD fluid with a reduced density representation, and systematically tune the repulsion parameters (a_{ij}) between water and carbon beads to reproduce key hydrophobic and interfacial behaviors.

In parallel, we develop a coarse-grained representation of the DMPC molecule, following established models in the literature. The molecule is constructed to preserve its amphiphilic character, with a hydrophilic head and two hydrophobic tails. The interaction parameters are chosen to ensure realistic behavior in aqueous environments and near hydrophobic surfaces like carbon nanotubes.

This chapter also outlines the simulation setup, including the box dimensions, initial conditions, temperature control, unit system, and interaction potentials. Together, these models serve as the computational basis for simulating the thermal response and functionalization efficiency of SWCNTs in later chapters. The framework developed here enables us to investigate how molecules like DSPE-PEG interact with the nanotube surface and how such interactions influence dispersion, thermal conduction, and biological applicability.

3.2 General simulation parameters

In this thesis, we use reduced units throughout, unless explicitly mentioned otherwise. Using reduced units is a common practice in Dissipative Particle Dynamics (DPD) simulations because it allows us to work with simplified, dimensionless numbers instead of physical units like joules or meters. This makes the equations easier to handle and the results easier to interpret and compare across different studies or materials.

Following the setup introduced by Groot and Warren (1997), we define the unit of energy by setting $k_BT = 1$, where T represents the temperature and is taken to be 300 K for reference. In the same way, we choose the mass of a particle $m = 1$ and the interaction cutoff distance $r_c = 1$. This means that all other quantities, such as time, force, and pressure, are automatically scaled based on these reference values.

3.2.1 Length and Time Scale Mapping to Real Units

To relate DPD simulation units to physical quantities, we begin by defining the bead density ρ as the number of DPD particles N divided by the volume of the system V. This bead density allows us to map the length and time scales using experimental data from a reference substance, which is water in this case.

The molecular volume of a water molecule is approximately $30\mathring{A}^3$. If one DPD bead represents three water molecules, then each bead corresponds to a volume of $90\mathring{A}^3$. Given a reduced bead density of $\rho r^3 = 3$, this implies that a cubic region of volume r^3 contains 3 beads, which totals $270\mathring{A}^3$ in physical volume (Valdivia and Jaime 2021). Solving for the interaction cutoff radius gives the following:

$$r_c = (270\ \text{Å}^3)^{1/3} \approx 6.47\ \text{Å}.$$

This length scale can also be applied to DMPC lipids. The DMPC molecule can be divided into coarse-grained volumes of approximately $90\mathring{A}^3$, resulting in a model with 3 head beads and two tails composed of 5 beads each, as illustrated in Fig. 3.1.

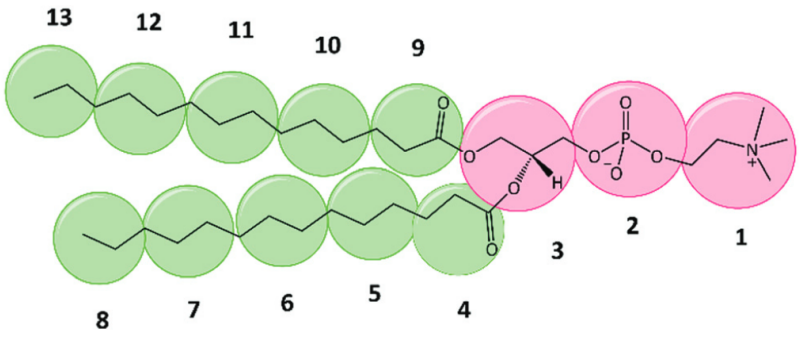


Figure 3.1 The atomistic structure of DMPC and its corresponding coarse-grained model used in this study are shown. Lime-colored beads represent the hydrophobic components, while mauve-colored beads indicate the hydrophilic regions.

To determine the time scale, we compare the self-diffusion behavior in DPD simulations with experimental data. The experimental self-diffusion constant of water at room temperature is $D_{\text{water}} = (2.43 \pm 0.01) \times 10^{-5}$ cm^2/s, as reported by Partington et al. (Partington et al. 1952). Groot (Groot 2003) showed that for a system with the repulsion parameter $a_{WW} = 25$, the mapping factor $N = 3$, and the bead density $\rho = 3$, the reduced time unit $\tau = 1$ corresponds to 160.4 ps. Let us walk through how Groot mapped the time unit in DPD via the diffusion coefficient.

To relate the DPD time unit to real physical time, we compare the self-diffusion coefficient of water in simulation and experiment.

Simulation Diffusivity

Groot's simulation results showed that the self-diffusion coefficient of water in reduced DPD units was:

$$D_{\text{water}}^{\text{DPD}} \approx 0.064$$

as reported in Groot and Warren (1997), for a system with repulsion parameter $a_{WW} = 25$, bead density $\rho = 3$, and mapping factor $N = 3$.

Matching Simulation to Experiment

To find the physical time scale corresponding to one DPD time unit, we match the diffusivity from simulation to the experimentally measured self-diffusion coefficient of water at room temperature, given by:

$$D_{\text{water}}^{\text{exp}} = 2.43 \times 10^{-5} \text{ cm}^2/\text{s}$$

The Einstein relation gives:

$$D = \frac{\langle \Delta r^2 \rangle}{6\tau}$$

We aim to find how much real time τ corresponds to one unit of reduced DPD time such that:

$$D_{\text{water}}^{\text{DPD}} \cdot \left(\frac{r_c^2}{\tau} \right) = D_{\text{water}}^{\text{exp}}$$

where r_c is the DPD cutoff length (typically mapped to $r_c \approx 0.645$ nm).

Result

From this relationship, and using the known values of $D_{\text{water}}^{\text{DPD}} \approx 0.064$, $r_c = 0.645$ nm $= 6.45 \times 10^{-8}$ cm, and $D_{\text{water}}^{\text{exp}} = 2.43 \times 10^{-5}$ cm^2/s, Groot found that:

$$\tau = 160.4 \text{ ps}$$

Thus, one unit of reduced time in the DPD simulation corresponds to approximately 160.4 picoseconds of physical time.

In this work, we use time steps of $\delta t = 0.05\tau$ and $\delta t = 0.005\tau$, which correspond to approximately 4.8 ps and 9.6 ps, respectively.

All simulations were conducted using the LAMMPS energy conservative dissipative particle dynamics package (Li et al. 2017).

By working in this normalized system of units, we avoid the need to constantly convert between different physical scales and can focus more directly on the behavior and trends in the simulation.

3.2.2 Lattice Geometry and Physical Basis

Because DPDE is not an atom-based simulation, the model of a CNT does not have to be a honeycomb lattice. The CG model is based on a triangular bead lattice that wraps around a cylindrical geometry to approximate the surface of an SWCNT. Each bead in the lattice represents a phenalene-like molecular fragment, chosen for its structural and hydrophobic similarity to the carbon nanotube wall (Valdivia and Jaime 2021). The equilibrium bond length between adjacent beads is set to $r_0 = 0.77$ in reduced units, corresponding to approximately 4.99 Å. This spacing matches the length of one phenalene unit along the nanotube axis Valdivia and Jaime (2021). The cutoff distance is set to $r_c = 1.0$ (approximately 6.46 Å). This distance defines the maximum range within which the beads interact via the conservative repulsive force. The beads separated by a distance greater than r_c do not exert any conservative force on each other.

To eliminate gaps between adjacent bead rings that can allow water to pass through, each ring is rotated at an angle $\theta_{\text{rot}} = 360°/n$, where n is the number of beads in the ring. This forms a **staggered triangular lattice** across the surface of the tube, effectively closing the open paths between rings and mimicking the impermeable nature of the real SWCNT walls.

To ensure that the cylindrical structure of the coarse-grained single-walled carbon nanotube (SWCNT) remains stable throughout the simulation while still allowing for realistic flexibility and thermal motion, a system of harmonic bonds and angular potentials is employed.

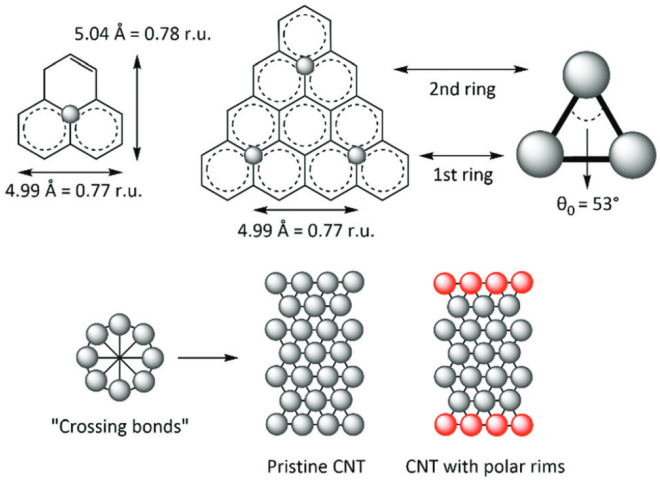


Figure 3.2 Schematic of the coarse-grained model used for carbon nanotubes (CNTs). The spheres represent the centers of mass of coarse-grained beads distributed along the CNT wall. Grey beads correspond to phenalene-like carbon structures, while red beads represent phenalene-like units functionalized with polar groups such as –OH or –COOH. (Valdivia and Jaime 2021)

Each bead in the SWCNT is connected to its nearest neighbors via harmonic bonds defined by the following potential:

$$U_{\text{bond}}(r) = \frac{1}{2} K_r (r - r_0)^2$$

where: r is the instantaneous distance between two bonded beads, r_0 is the equilibrium bond length (typically equal to the lattice spacing), and K_r is the bond spring constant, controlling the stiffness of the bond (units: energy/distance^2).

In our model, crossing bonds are added between diametrically or angularly opposed beads within the same ring of the nanotube. These bonds help maintain the circular symmetry of each ring and prevent lateral deformation, effectively reinforcing the cylindrical structure of the SWCNT.

To further maintain the curvature and cylindrical geometry of the nanotube, "harmonic angle potentials" are defined between triplets of connected beads. The angular potential is given by:

$$U_{\text{angle}}(\theta) = \frac{1}{2} K_\theta (\theta - \theta_0)^2$$

where: θ is the instantaneous angle between two consecutive bonds, θ_0 is the equilibrium angle, K_θ is the angular spring constant (units: energy/radian^2).

Although θ_0 is specified in degrees in the LAMMPS input (e.g., 53°), LAMMPS internally converts this to radians for computation. The prefactor K_θ thus determines the energy cost of deviating from the preferred curvature.

In this work, the following parameter values were used:

- Bond spring constant: $K_r = 180$
- Angular spring constant: $K_\theta = 55$
- Equilibrium angle: $\theta_0 = 53°$
- Equilibrium distance: $r_0 = 0.77$

These parameters were chosen to balance the mechanical rigidity and flexibility of the nanotube, allowing it to undergo realistic thermal fluctuations and moderate bending without collapsing or deviating significantly from its intended cylindrical form. This approach ensures that the coarse-grained SWCNT behaves analogously to real carbon nanotubes, which are known for their high axial stiffness and moderate flexibility under lateral forces.

3.2.3 Soft-Repulsion Parameters

The complete set of soft-repulsion parameters used in this study is summarized in **Table 1**. The coarse-grained (CG) model for DMPC lipids consists of only two bead types: *head beads* (H) and *tail beads* (t).

A standard value of $a_{\mathrm{WW}} = 25$ was adopted for water–water interactions, following the work by Groot (Groot and Warren 1997). Although the DMPC molecule contains three distinct headgroup fragments, all were treated as identical in this model. The average solvation energy of these fragments was used to estimate the water-head interaction parameter, which yields $a_{\mathrm{HW}} = 15$.

For the lipid tails, which are strongly hydrophobic, a higher repulsion parameter was used to reflect their poor solvation in water: $a_{\mathrm{tW}} = 80$.

The calculated solvation energy of *single-walled carbon nanotubes* (SWCNT) in water leads to an estimated water–CNT interaction parameter of $a_{\mathrm{CNTW}} = 75$ (Valdivia and Jaime 2021). The interactions between SWCNTs and the DMPC bilayer were parameterized as follows:

- For the **head bead–CNT interaction**, $a_{\mathrm{CNTH}} = 75$, matching the repulsion between water and CNTs.

- Since lipid tails and CNT walls are both highly hydrophobic, the **tail bead–CNT interaction** was modeled based on a slightly higher water affinity of phenalene compared to lipid tails (estimated using propane solvation energy). With $a_{\mathrm{tt}} = 25$ and a difference of 5 between $a_{\mathrm{tW}} = 80$ and $a_{\mathrm{CNTW}} = 75$, the value for the tail–CNT interaction was set to $a_{\mathrm{CNTt}} = 30$.

a_{ij}	W	t	H	CNT
W	25	80	15	75
t		25	80	30
H			35	75
CNT				25

Table 3.1 Soft repulsion parameters a_{ij} used in this article for a system composed of DMPC molecules, one SWCNT, and water.

Summary

This chapter presented the parameterization and structural setup of our coarse-grained model, built for energy-conserving dissipative particle dynamics (eDPD) simulations. We began by adopting the standard dimensionless unit system proposed by Groot and Warren (1997), in which energy, mass, and length are normalized as $k_BT = 1$, $m = 1$, and $r_c = 1$, respectively. This approach simplifies the model formulation and facilitates comparison across simulation studies.

We then mapped these dimensionless quantities to physical units using water as a reference fluid. A bead density of $\rho = 3$ and a coarse-graining level of 3 water molecules per bead led to an interaction cutoff radius of $r_c \approx 0.645$ nm and a time unit of $\tau \approx 160.4$ ps, based on the experimental self-diffusion coefficient of water.

Next, we described the cylindrical lattice geometry used to model single-walled carbon nanotubes (SWCNTs), where each bead represents a phenalene-like segment. Harmonic bond and angular potentials were implemented to preserve cylindrical symmetry and mechanical stability while allowing for thermal fluctuations.

The chapter concluded with a discussion of the soft-repulsion parameters used to model non-bonded interactions between water, lipid head and tail groups, and CNT walls. These interaction strengths were derived based on solvation energy comparisons and were chosen to reproduce the expected hydrophilic and hydrophobic behavior in aqueous environments.

Together, these physical mappings, structural definitions, and interaction parameters establish a robust simulation framework for investigating the mechanics and thermodynamics of CNT–biomolecule systems. In the following chapter, the developed model is employed to simulate the mechanical response of carbon nanotubes (CNTs) under applied strain and stress, validating their deformation behavior against known physical properties of real SWCNTs. Additionally, we investigate heat transfer across CNT–water interfaces, with a particular focus on quantifying the Kapitza resistance.

Chapter 4

LAMMPS-Based Modeling of SWCNT Mechanics and Kapitza Resistance

4.1 Introduction

In previous chapters, we discussed the theoretical foundations of Dissipative Particle Dynamics (DPD) and its energy-conserving extension (eDPD). In this chapter, we shift our focus to the implementation and application of these models within the LAMMPS simulation package, specifically for studying interfacial heat transfer and Kapitza resistance in nanostructured systems.

Kapitza resistance, or thermal boundary resistance, arises at interfaces between materials with mismatched phonon spectra and manifests itself as a temperature discontinuity under constant heat flux (Opsal and Pollack 1974). This phenomenon is critical in various applications including drug delivery, lubrication, nanoelectronics, and photothermal therapy, where accurate thermal management at interfaces is essential. Traditional continuum methods lack the resolution to capture these effects, while molecular dynamics (MD) simulations are often too computationally intensive. The eDPD method offers a mesoscopic alternative that balances resolution with efficiency, but its ability to capture thermal boundary resistance in systems with heterogeneous material properties remains an open question.

This chapter documents our approach to modeling Kapitza resistance in LAMMPS, beginning with an assessment of how LAMMPS handles energy exchange between materials with differing transport coefficients. We then apply this understanding to simulate heat transfer across idealized and realistic interfaces in the carbon–water system. These studies include the effects of hydrophobicity, thermal rectification, and the role of interfacial parameter tuning on thermal resistance.

By resolving these implementation challenges and validating results against known behavior, we establish a reliable methodology for investigating interfacial heat transfer in complex nanostructured systems using eDPD in LAMMPS.

4.1.1 Modelling and measuring thermal conductivity in LAMMPS

During the modeling of thermal conductivity, we observed a discrepancy in the LAMMPS documentation. I would like to present the problem and a series of experiments that we performed to better understand the behavior of the eDPD package.

LAMMPS documentation gives the following formula for the heat per unit time conducted from particle j to particle i:

$$q_i^C = k_{ij}\,\omega(r_{ij})\,(T_i - T_j)$$

where

$$k_{ij} = \frac{C_v^2\,\tilde{\kappa}\,(T_i + T_j)}{4k_B}$$

and ω is a dimensionless weight function. (We use the symbol $\tilde{\kappa}$ instead of κ to distinguish the LAMMPS parameter from the standard thermal conductivity.)

The documentation states that $\tilde{\kappa}$ has "thermal conductivity units" but does not identify it as the actual thermal conductivity of the material. According to LAMMPS, $\tilde{\kappa}$ is the "mesoscopic heat friction" for which the following formula is given:

$$\tilde{\kappa} = \frac{315 k_B \, \nu}{2\pi c_V r_c^5 \, \mathrm{Pr}}$$

where ν is the kinematic viscosity and Pr is the dimensionless Prandtl number. However, the dimensions of this expression do not match the units required for $\tilde{\kappa}$ if q_i^C is to have units of energy per time (J/s).

The connection between the heat conduction equation and the coefficient k_{ij} was developed in an earlier discussion. Our derivation, which relates to the heat current equation q_i^C, differs from the LAMMPS result by a factor of C_v^2, as our derivation used κ, the actual thermal conductivity.

Furthermore, it is unclear how to handle the LAMMPS formula when heat is transferred between dissimilar beads. The documentation incorrectly treats $\tilde{\kappa}$ as a scalar rather than a pairwise parameter $\tilde{\kappa}_{ij}$. Also, it is not clear which C_v (the bead heat capacity, defined in the bead parameters) should be used. Since energy conservation requires $q_{ij} = -q_{ji}$, we cannot simply choose C_v of one bead over the other.

We have performed several simulation runs and calculated the slope $\frac{dT}{dx}$ for a fixed heat flux through the system. Since

$$\Phi_{\mathrm{heat}} = J_{\mathrm{heat}} A = \left(\sigma_{\mathrm{therm}} \frac{dT}{dx} \right) A$$

we can also use this relationship to investigate the scaling behavior of $\frac{dT}{dx}$ as a function of κ_{ij} and C_v. We can check the scaling of the slope as a function of κ_{ij} and C_V. If the LAMMPS documentation is correct, then scaling κ by some constant α and C_V by $1/\sqrt{\alpha}$ should result in no change in the heat transferred and thus the thermal conductivity. (Recall that the user specifies the exact values of these parameters at the start of the simulation.)
We now outline the simulation setup and the series of experiments carried out to explore this discrepancy.

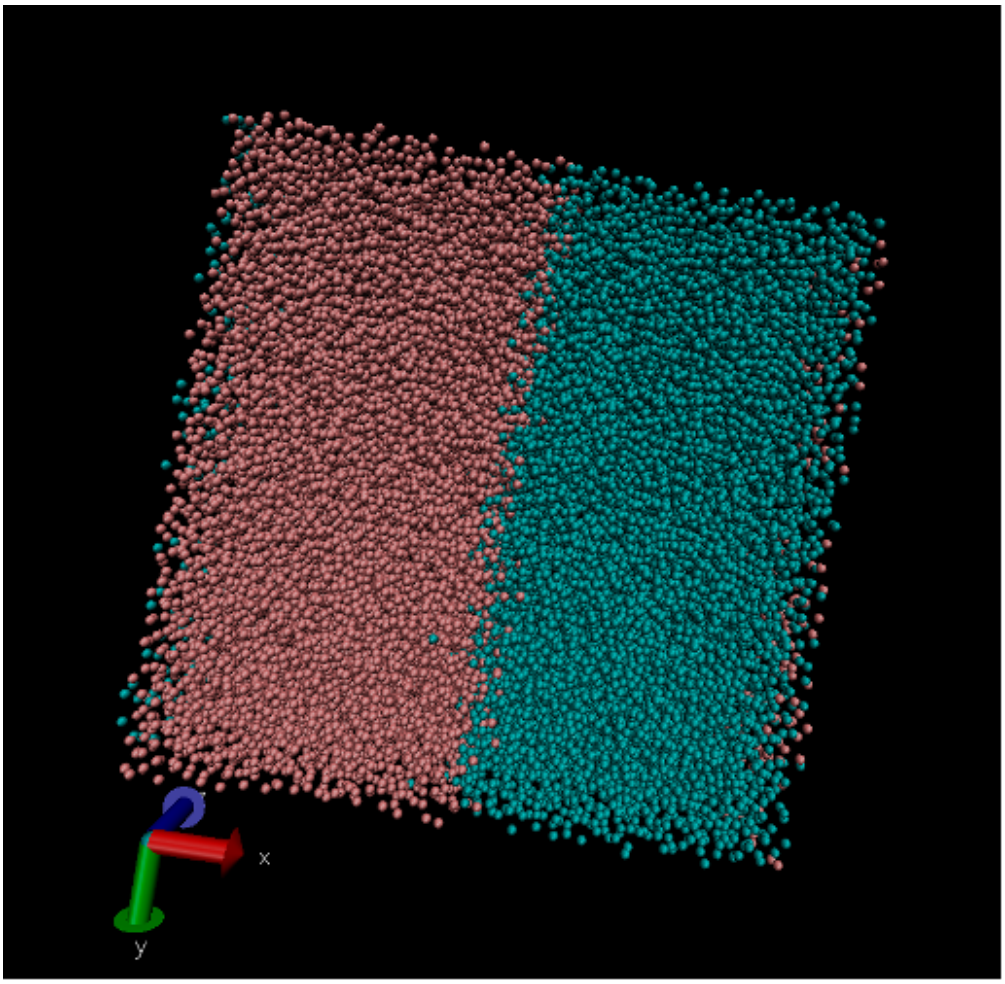


Figure 4.1 VMD visualization of Computational setup in LAMMPS showing two distinct materials separated by an interface. The left region (pink) consists of one material, while the right region (teal) consists of a different material, enabling the study of Kapitza resistance at the interface.

We first define a rectangular simulation volume with periodic boundary conditions and divide it into two equal halves. We fill the region on the left with beads of one type and the right with beads of a second, which can have different simulation parameters (Fig. 4.1). We fix the beads on the left at rigid positions in space, forming a solid slab, while those on the right can either be fixed or allowed to flow, depending upon the goals of the simulation.

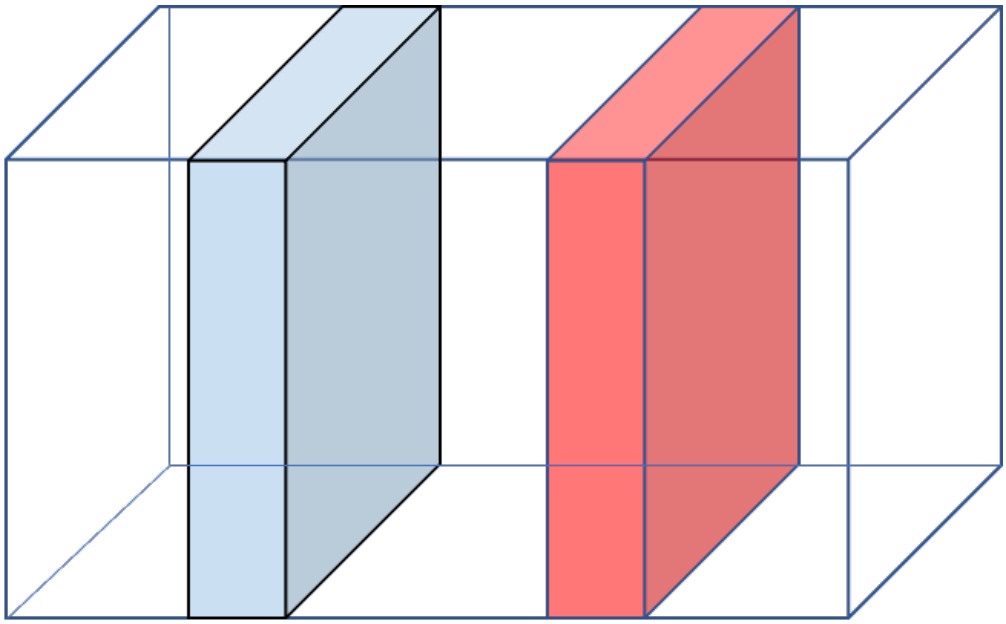


Figure 4.2 Schematic of the model: heating and cooling regions at constant equal rates produce a temperature profile with the purpose of extracting the thermal conductivity. The system has periodic boundary conditions in x, y and z directions.

As shown in Fig. 4.2, a heat source was applied to the center of one region, while a heat sink was applied to the center of the other region. This imposed a steady-state heat flux across the system, allowing a steady state temperature profile to develop over time. The temperature was sampled across the simulation domain in the direction of heat flow, averaging across a plane perpendicular to the flux.

To better understand how LAMMPS handles themal conductivity between dissimilar materials, it is necessary first to understand how the simulation behaves with uniform parameters. In Fig. 4.3, we show a plot of the temperature as a function of position for fixed heat flux. In these runs, we choose the medium to be uniform, with all material parameters identical on the left and right sides. We choose the heat capacity to be $C_V = C_0/\sqrt{\alpha}$, and $\tilde{\kappa}_{ij} = \alpha\kappa_0$ ($\tilde{\kappa}_{ij}$ is the mesoscopic heat friction), where α is a parameter that allows us to scale the specific heat and thermal diffusivity but keep the product $\tilde{\kappa}_{ij}C_V^2$ constant. This choice would imply, from eq.(4.1.1) that the temperature profiles should be identical for all values

of α.

$$K_{ij} = \frac{C^2 \tilde{\kappa}_{ij}}{4k_B} \cdot (T_i + T_j)^2 \tag{4.1}$$

Here, C_V is the volumetric heat capacity, $\tilde{\kappa}_{ij}$ is the microscopic (mesoscopic) heat friction coefficient, and k_B is the Boltzmann constant.

To investigate the temperature profiles for different values α, we developed a simulation model that is described in detail below, and the corresponding code is provided in the appendix. We define a rectangular simulation domain that extends from $-20 \leq x \leq 20$, $-20 \leq y \leq 20$, and $-10 \leq z \leq 10$, with periodic boundary conditions applied in the three spatial directions. This domain is divided along the x axis into two equal regions: `edpd1` (left half) and `edpd2` (right half), each containing 64,000 randomly distributed eDPD particles of types 1 and 2, respectively. Both materials have a mass of 1.0, but their volumetric heat capacities differ: Type 1 beads are assigned $C_v = 1.0 \times 10^5$, and type 2 beads have $C_v = 1.0 \times 10^5/\sqrt{\alpha}$, with $\alpha = 1$ in this case. Pairwise interactions use the energy-conserving DPD force field (eDPD) with a cutoff of 1.58 and consistent coefficients for all combination types, including temperature-dependent conductivity terms via the `power` and `kappa` options. The nominal thermal conductivity for the homogeneous media (types 1 and 2) is set to $k = 1.45 \times 10^{-5}$, while the cross-type heat friction coefficient k_{12} is derived using the harmonic mean formula to ensure a significant interfacial resistance. A heat source is applied at $x = -10$ and a heat sink at $x = +10$, each depositing or removing energy at a rate of ± 0.005 in reduced units. The simulation is performed with a timestep of 0.01 using the `mvv/edpd` integrator, and the system evolves for 100,000 steps after an initial transient of 500 steps. The temperature is computed at the atomic level using `compute edpd/temp/atom` and averaged spatially along the x-axis using `chunk/atom bin/1d` with a bin size of 0.05. The resulting temperature profiles allow for quantifying the thermal boundary resistance

(Kapitza resistance) that arises at the interface between the two materials.

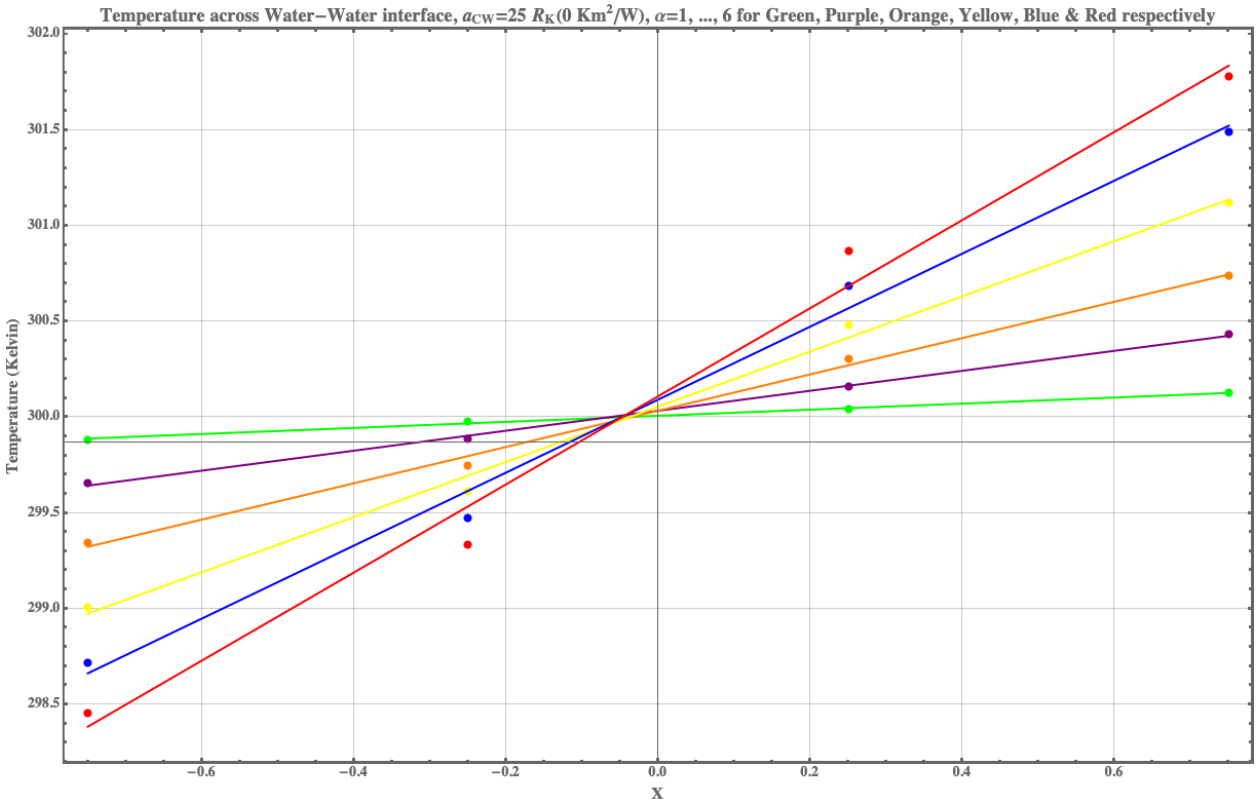


Figure 4.3 Plot showing the temperature as a function of position while varying the interfacial thermal conductivity k_{ij} and specific heat capacity C_V, while holding the product $k_{ij}C_V^2$ constant. The simulation was performed in a periodic box spanning $-20 \leq x \leq 20$, $-20 \leq y \leq 20$, and $-10 \leq z \leq 10$, filled with 128,000 energy-conserving DPD particles (64,000 of each type). Type 1 particles were assigned $C_V = 1.0 \times 10^5$, while Type 2 particles were assigned $C_V = \frac{1.0\times10^5}{\sqrt{\alpha}}$, and thermal conductivity scaled as $k = \alpha \cdot 1.45 \times 10^{-5}$ to preserve $k_{ij}C_V^2$. A fixed heat flux of ± 0.005 was applied at $x = \pm 10$, and temperature profiles were obtained after 100,000 timesteps using a timestep size of 0.01. Temperature was calculated per bead and averaged in 1D spatial bins of size 0.05.

As we discussed, according to Eq. (4.1.1), if the product $\tilde{\kappa}_{ij}C_V^2$ remains constant, one would expect the thermal conductivity K_{ij} to also remain constant for a uniform temperature

field, and consequently, the steady-state temperature profiles under fixed heat flux should be identical. However, the simulation results in Figure 4.3 show a clear deviation from this expectation. Although the product $\tilde{\kappa}_{ij}C_V^2$ is kept constant, the resulting temperature gradients vary significantly with α.

To investigate this problem, we checked the scaling of the slope as a function of $\kappa_{i,j}$ and C_V separately to investigate the cause. As you know by now, We had hypothesize that since

$$k_{i,j} \propto \tilde{\kappa} C_V^2$$

scaling $\tilde{\kappa}$ by a factor α, and C_V by $1/\sqrt{\alpha}$, would keep $k_{i,j}$ unchanged. However, since our results did not confirm this, we decided to investigate this change. In Fig.4.4 we show the change in the temperature gradient with respect to different values of α.

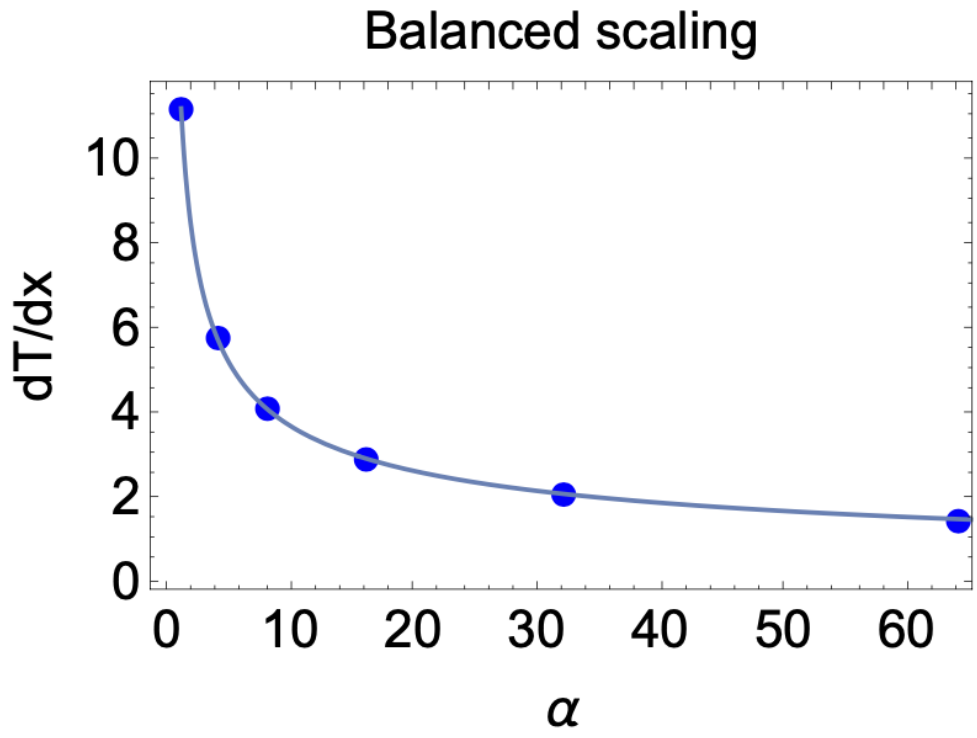


Figure 4.4 Scaling of the slope $\frac{dT}{dx}$ as a function of α. The results suggest that $k_{i,j} \propto \tilde{\kappa}/C_V^2$ is not supported by the numerical data.

Although we expect no change in the temperature gradient, we see that the data fit the scaling of $1/\sqrt{\alpha}$ very well! How can this happen? Let us check the scaling for $\tilde{\kappa}$ and C_v separately to investigate how each one of them affect the thermal conductivity.

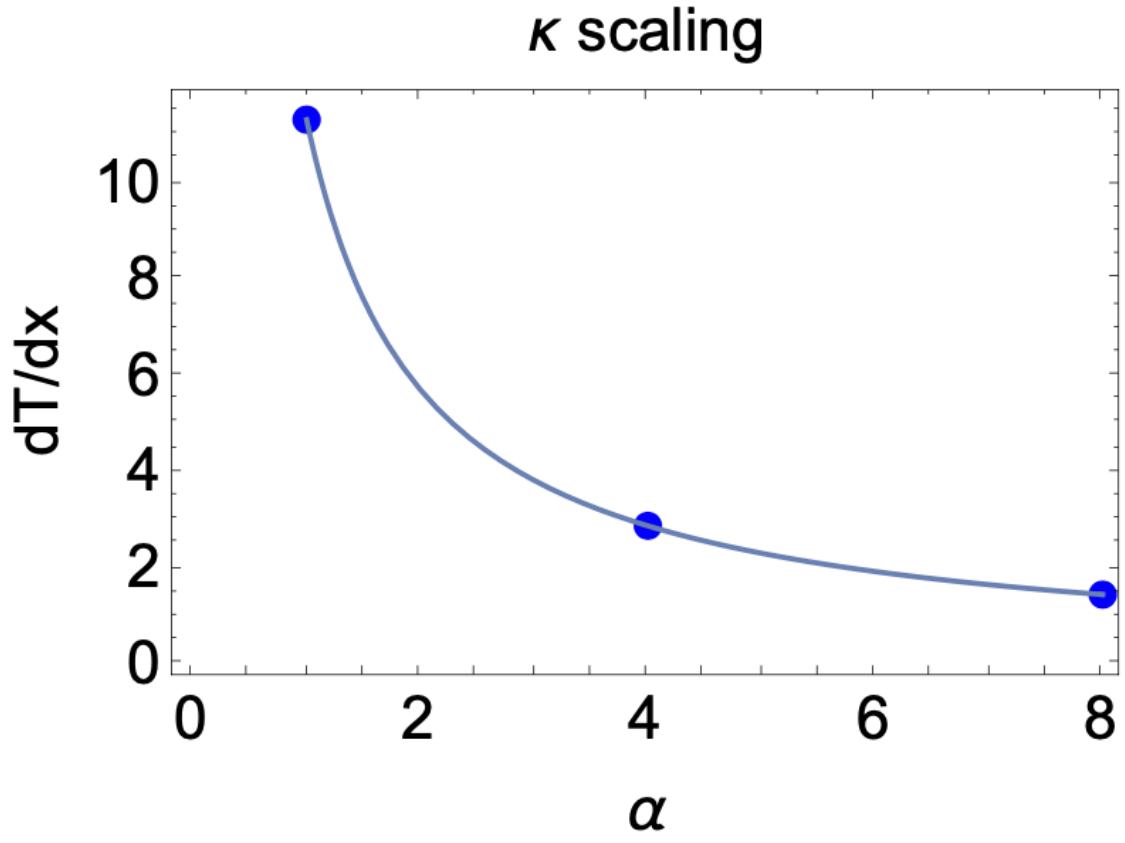


Figure 4.5 Temperature gradient variation with respect to $\tilde{\kappa}$ scaling, demonstrating a clear $\frac{1}{\alpha}$ relationship.

It is important to note that we scaled $\tilde{\kappa} \propto \alpha$, and the resulting data clearly demonstrate a direct proportionality to $\frac{1}{\alpha}$. Next, we examine the plot where only C_v is scaled.

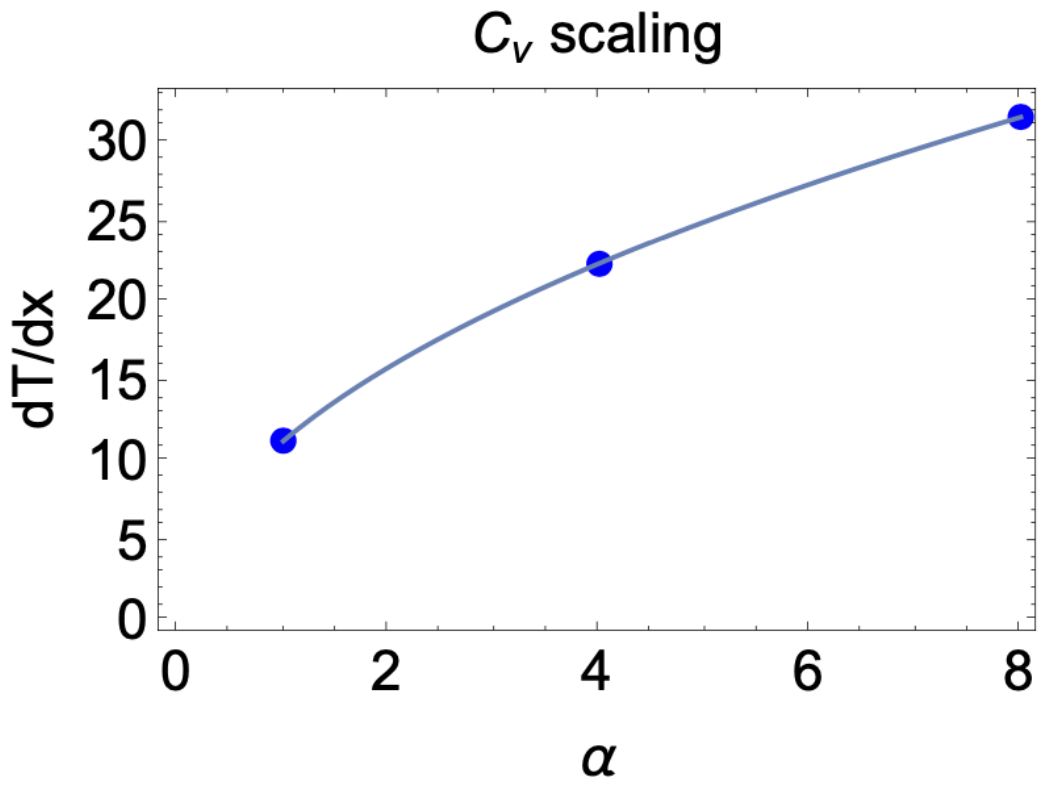


Figure 4.6 Temperature gradient variation with respect to C_v scaling, demonstrating a clear $\sqrt{\alpha}$ relationship.

From the C_v scaling plot, one can observe that $\sqrt{\alpha}$ provides a good fit. However, to verify this behavior, we also apply a linear fit for comparison.

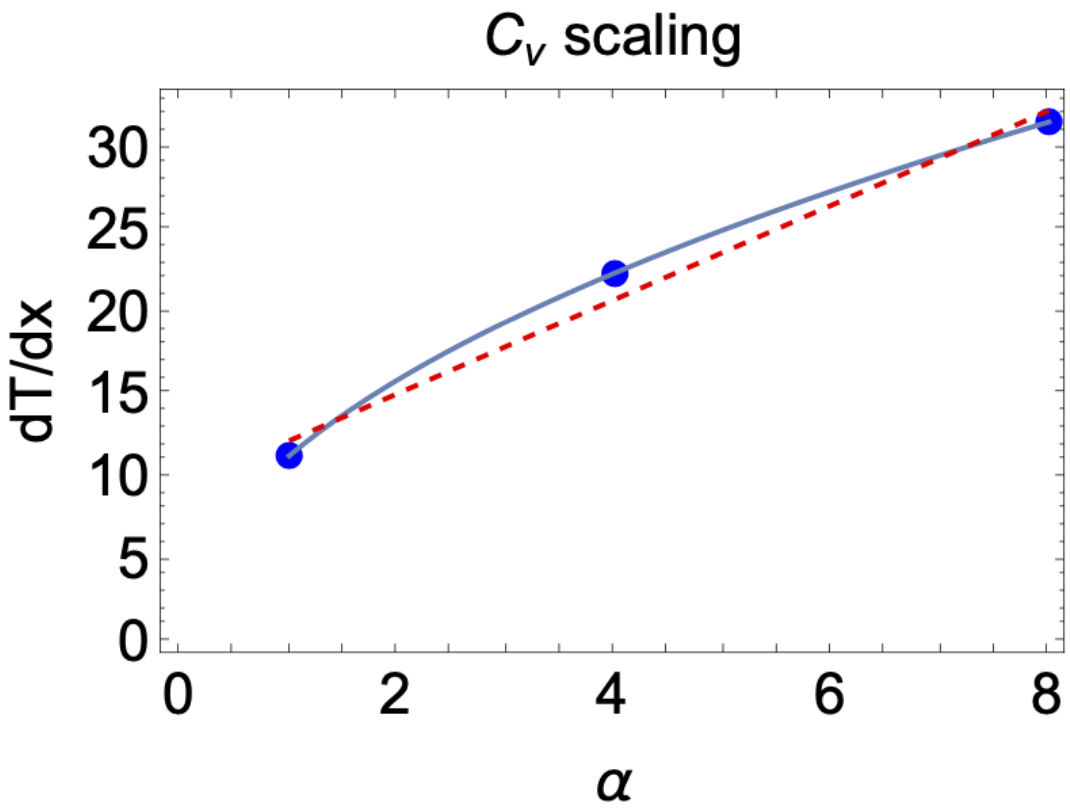


Figure 4.7 Comparison of nonlinear (blue solid line) and linear (red dashed line) fits for the temperature gradient $\frac{dT}{dx}$ as a function of α under C_v scaling. The nonlinear fit, corresponding to $\sqrt{\alpha}$, shows better agreement with the data than the linear fit, suggesting that $\frac{dT}{dx} \propto \sqrt{\alpha}$ provides a more accurate description of the scaling behavior.

What does this imply? If C_v is scaled to decrease as $\frac{1}{\sqrt{\alpha}}$, then an increase proportional to $\sqrt{\alpha}$ leads to a temperature gradient $\frac{dT}{dx}$ that is inversely proportional to C_v.

To conclude, the runs and analysis above show that the slope $\frac{dT}{dx}$ decreases as $\frac{1}{\tilde{\kappa}}$, which is reasonable. The better the thermal diffusivity, the better the thermal conductivity, and the smaller the slope. They also show that the slope $\frac{dT}{dx}$ decreases as $\frac{1}{C_v}$.

The above results make sense if we assume again that the LAMMPS documentation is incorrect, and instead use:

$$K_{ij} = \frac{C_v \tilde{\kappa}_{ij} \left(T_i + T_j\right)^2}{4k_B}$$

and assume that

$$\tilde{\kappa} = \frac{\kappa}{C_v}$$

where C_v is the heat capacity of a bead. This is not unreasonable. The kinematic viscosity is defined from dynamic viscosity by dividing by the mass/volume (in eDPD this works out to be the mass/bead). Here we are taking the ratio of the conductivity to the heat/bead.

4.1.2 System Stability and Thermal Transport: Sensitivity to Bin Size and Timestep

Prior to modeling the thermal conductivity between carbon and water, using eDPD, we examined the stability and accuracy of eDPD simulations across interfaces with differing heat capacities, we used a modified version of the setup from Li et al. (Li et al. 2014). We tested both single- and two-region configurations with identical and differing specific heat capacities (C_V).

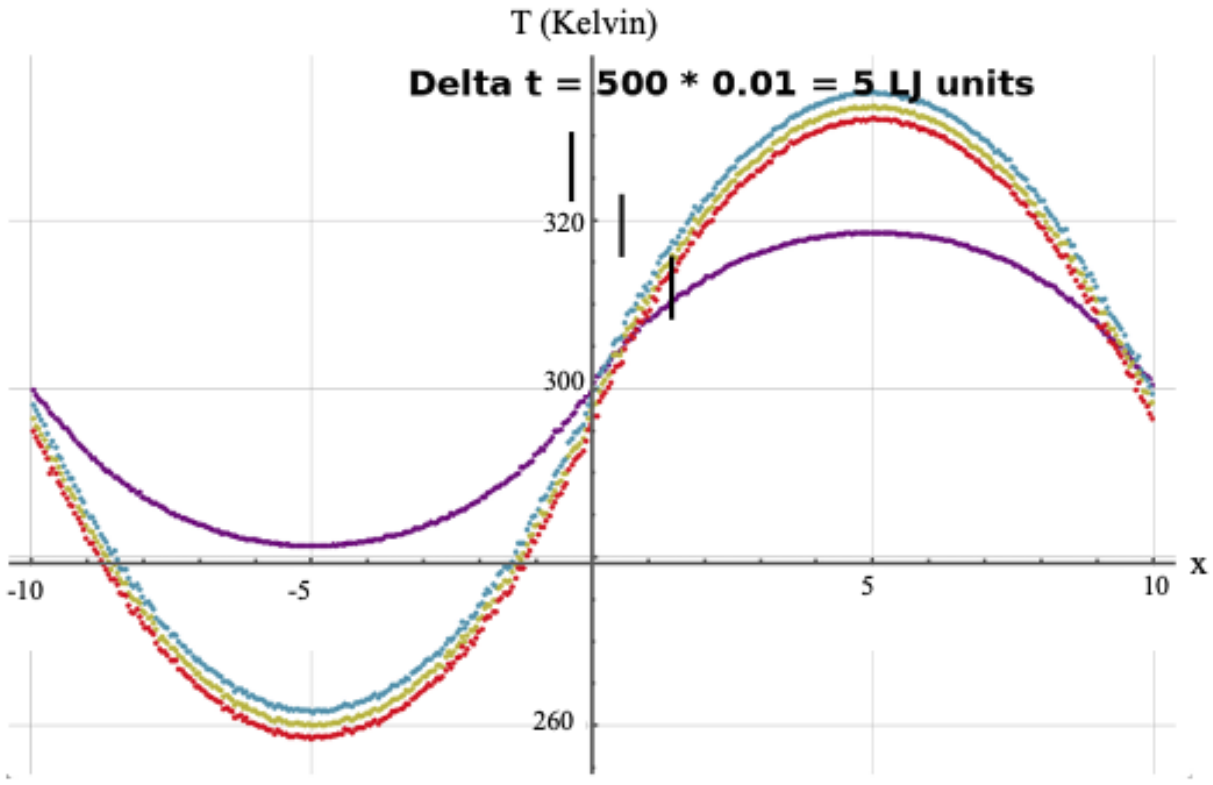


Figure 4.8 Temperature profile for two regions with identical heat capacities ($C_{V1} = C_{V2}$) using bin size 0.5. The simulation used timestep $\Delta t = 0.01$ and collapsed after 77,000 timesteps due to instability.

Figure 4.8 illustrates the temperature profile obtained from a two-region simulation in which both regions contain eDPD particles with identical physical properties, corresponding to water. Although the left and right halves of the simulation box are assigned different atom types (type 1 and type 2), they are parameterized identically, serving as a control to test whether the interface alone induces numerical artifacts. The simulation uses parameters originally proposed by Li et al. (Li et al. 2014), including a number density $\rho = 4.0$ and a characteristic length scale $L^* = 11$ nm. In this model, the volumetric heat capacity of water at 300 K, $C_v^* = 4.167 \times 10^6$ J·m^{-3}·K^{-1}, is scaled by using the Boltzmann constant $k_B = 1.381 \times 10^{-23}$ J·K^{-1}, resulting in a dimensionless heat capacity $C_v = 1.0 \times 10^5$.
Despite the thermodynamic uniformity of the system, the simulation becomes numerically

unstable and collapses after 77,000 time steps when a time step of $\Delta t = 0.01$ is used in conjunction with a small bin size of 0.5 for spatial averaging. This is attributed to the noise in temperature estimation, exacerbated by insufficient averaging due to the small bin width. The 'fix ave/chunk' command, which computes spatially averaged quantities such as temperature, may introduce fluctuations when the averaging region is too small to contain enough particles. As a result, the temperature data become noisy, triggering instability in the integrator. This example underscores the importance of carefully tuning both timestep and spatial resolution in eDPD simulations, even when modeling physically homogeneous systems.

Figure 4.9 shows the behavior of the original Li setup (but bin size changed to 0.5) in the

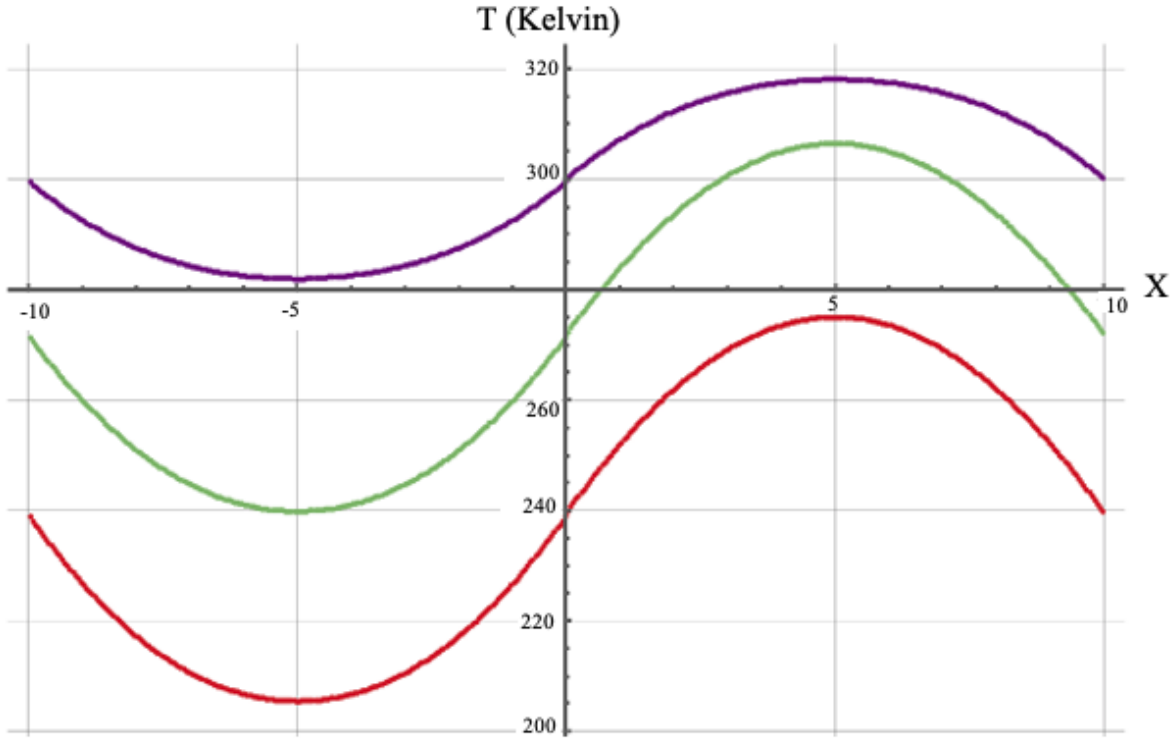


Figure 4.9 Temperature evolution from the original Li input file using $\Delta t = 0.01$. Simulation becomes unstable and fails at timestep 67,000.

same timestep as in 0.01. The system also becomes unstable after approximately 67,000 steps. This supports the hypothesis that the choice of timestep is critical for the stability of

eDPD simulations. Figure 4.10 demonstrates that increasing the bin size to 1.0 and reducing

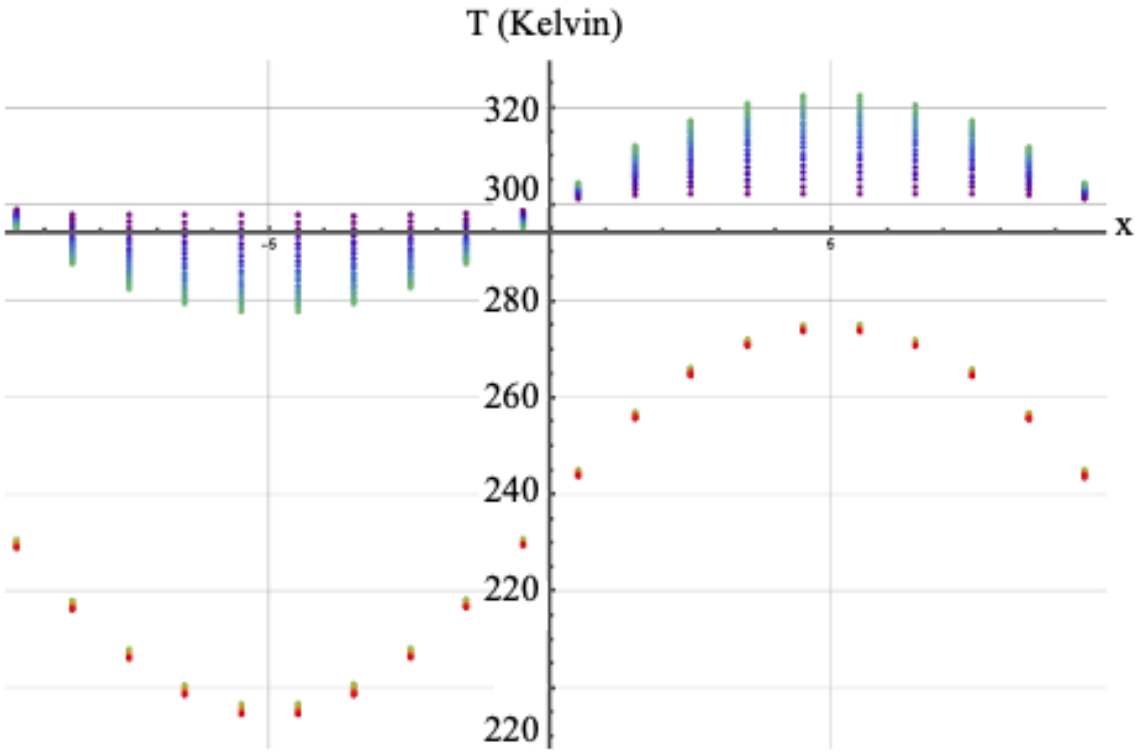


Figure 4.10 Two-region simulation using Li's parameters with larger bin size (1.0) and smaller timestep ($\Delta t = 0.001$). The system remains stable for over 1,000,000 timesteps. The lower data points indicate that the system becomes unstable and produces unphysical temperature values.

the timestep to 0.001 significantly improves stability. This supports the findings of Groot and Warren (Groot and Warren 1997), who emphasize the importance of small time step and adequate averaging for temperature computation.

Figure 4.11 shows the temperature profile for a two-region eDPD system where the heat capacities C_V differ between the left and right regions, while all other physical properties are held constant. In this case, the simulation uses a reduced timestep $\Delta t = 0.001$ and a relatively large bin size of 1.0 to minimize noise in temperature averaging. Despite

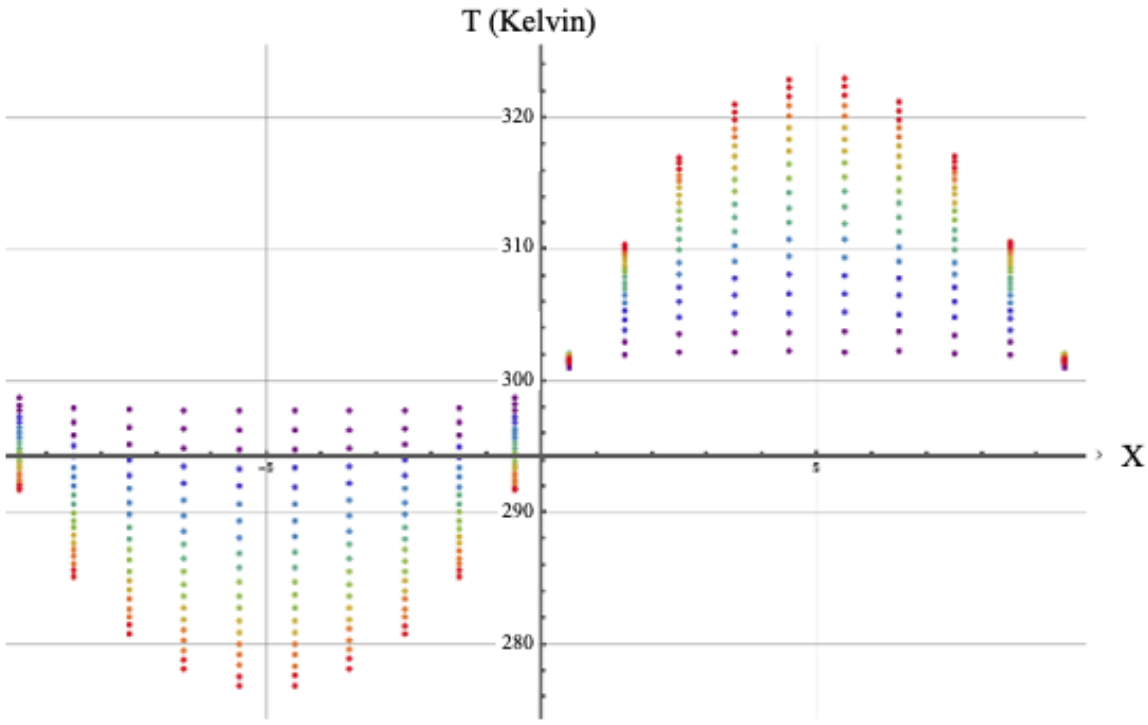


Figure 4.11 shows the case where the values of C_V are different in the two regions, corresponding to a water–hypothetical material interface.

these conservative numerical choices, the simulation eventually becomes unstable, collapsing around timestep 253,000 with the error message:

```
ERROR on proc 4:  Non-numeric atom coords - simulation unstable
(src/OPENMP/domain_omp.cpp:58)
```

This behavior suggests that the presence of a material contrast, specifically, a mismatch in C_V, introduces additional numerical challenges. One likely explanation is that the temperature gradients across the interface between the two materials become too steep, leading to strong energy fluxes that the eDPD integrator cannot stably resolve over long timescales.

Even with a small timestep and sufficient spatial averaging, energy mismatches between regions with different thermal storage capacities can induce oscillations in local temperature or pressure fields. These instabilities may accumulate gradually, eventually resulting in

nonphysical coordinates or velocities. The fact that the error occurs after a relatively long run-time indicates that, for heterogeneous systems, the total simulation time must also be chosen carefully to avoid divergence.

This highlights a key limitation of energy-conserving DPD methods: while suitable for capturing mesoscale thermal transport, they are sensitive to numerical noise and material discontinuities, especially under strong heat flux. Adaptive time-stepping, localized damping, or multiscale coupling strategies may be needed in future work to simulate such systems over longer durations reliably.

Discussion: These experiments confirm that eDPD simulations are highly sensitive to both timestep and spatial averaging settings. Specifically:
- A smaller timestep ($\Delta t = 0.001$) is essential for avoiding non-physical temperature spikes and ensuring numerical stability.
- Larger bin sizes (e.g., 1.0) help average out local noise in temperature estimation and reduce spurious instability.
- Even when C_V and κ are varied such that the product $C_V^2\kappa$ remains constant (to keep mesoscopic k_{ij} constant), the practical stability of the system may still depend on absolute values and their interaction with other system parameters such as interfacial friction and thermal noise.

This supports the interpretation that while the theoretical expression for mesoscopic thermal conductivity is invariant under specific parameter scaling, the numerical behavior of LAMMPS is not. Special care is required in setting both physical and numerical parameters to effectively model Kapitza resistance.

4.1.3 Modeling thermal interface resistance in LAMMPS

Given the understanding of how LAMMPS behaves with a uniform system, we can now explore interfacial resistance between dissimilar materials. The simulation procedure is the same as above. The temperature profiles near each side of the boundary were extended linearly to the boundary, and the slopes and the jump in temperature, ΔT were determined. The Kapitza resistance (R_K) was then calculated using the relation:

$$R_K = \frac{\Delta T}{J}$$

where J represents the heat flux obtained from the energy exchange rates at the thermostats.

For a given choice of specific heat, mass and thermal diffusivity, there may be a jump in the temperature at the interface, but given that eDPD is *not* a microscopic model, there is no reason to expect that it will be the experimentally observed value. Moreover, we have a free parameter, κ_{ij} the thermal diffusivity between the two materials, that needs to be specified. If we assume that the thermal diffusivity of the bulk materials, κ_{11} and κ_{22} are known, a reasonable starting point is to choose the harmonic mean:

$$\kappa_{12}^{(0)} = \frac{2\kappa_{11}\kappa_{22}}{\kappa_{11} + \kappa_{22}}$$

This formula served as a baseline. It acts correctly in the limits of $\kappa_{11} \sim 0$ or $\kappa 22 \sim 0$ and $\kappa_{11} = \kappa 22$ as well. We can adjust the value of κ_{12} around this initial estimate to find the most suitable coefficients that produce realistic Kapitza resistance in the simulation.

In the next section, we will demonstrate a practical example involving water and carbon to calculate the Kapitza resistance.

4.2 Kapitza resistance between carbon and water

The methodology outlined above was employed to calculate the Kapitza resistance at the water-carbon interface. The simulation box was divided into two regions: the right region (blue) represented water, while the left region (red) represented carbon. The total box size was chosen as $(40 \times 40 \times 20)$, with a bead density of $\rho = 3$, resulting in 48,000 carbon beads and 48000 water beads.

In this simulation, dimensionless variables were used, consistent with Lennard-Jones (LJ) units in LAMMPS terminology. The temperature was scaled using $T = 300\,\mathrm{K}$. The unitless heat capacity for both carbon and water was calculated using the equation:

$$C_v^* = \frac{C_v L^3}{\rho k_B},$$

where C_v is the volumetric heat capacity of the fluid, L is the reference length scale, and ρ is the number density of eDPD particles, as previously mentioned. For example, for water at $300\,\mathrm{K}$,

$$C_v = 4.167 \times 10^6\,\mathrm{Jm^{-3}K^{-1}},$$

and

$$k_B = 1.381 \times 10^{-23}\,\mathrm{JK^{-1}}.$$

Using a length scale of $L = 64\,\mathrm{nm}$ and $\rho = 3$, the unitless heat capacity for water was approximated to

$$C_v^* = 1.0 \times 10^5.$$

Similarly, the heat capacity in LJ units for carbon was calculated as

$$C_v^* = 3.877 \times 10^3.$$

The unitless mass of water was set to $m_w = 1$, while for carbon, it was $m_c = 2.2$. Additionally, the heat friction coefficient values were calculated as

$$\kappa_{ww} = 8 \times 10^{-6},$$

and

$$\kappa_{cc} = 5.56 \times 10^{-4}.$$

In the simulation, a cubic region of size $(6 \times 40 \times 20)$ at the center of the carbon region was heated, while an identical region at the center of the water region was cooled. Once equilibrium was reached, a temperature jump was observed at the water-carbon interface, signifying the presence of Kapitza resistance. This phenomenon is depicted in (Fig. 4.12).

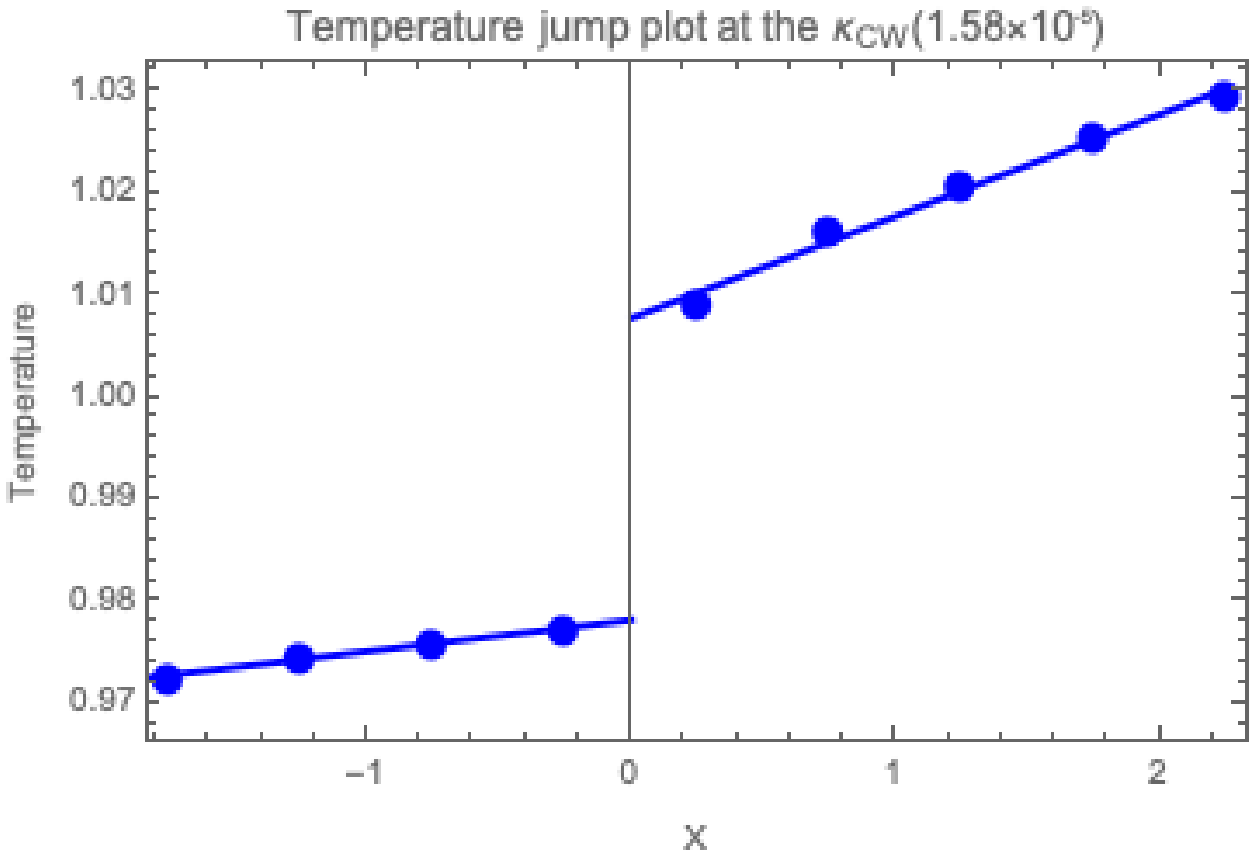


Figure 4.12 A temperature jump is observed at the water–carbon interface, indicating the presence of interfacial thermal resistance (Kapitza resistance) between the two materials.

Kapitza resistance is calculated based on the heat flux and the temperature difference at the carbon-water interface. The external heat flux, defined as energy per unit time, is applied to each bead within the heating cuboid domain as an input. By accounting for the total heating volume, the total energy transfer rate within the region can be determined. The total heat flux across the interface is then obtained by dividing the energy transfer rate by the interface area.

We can then tune the mesoscopic heat friction value at the water-carbon interface to observe how the Kapitza resistance changes with respect to κ_{CW} . Fig. 4.13 shows the Kapitza resistance values with respect to microscopic heat friction between two materials across two regions. The calculated Kapitza resistance is approximately in the range of $10^{-8} Km^2/W$ which is consistent the simulated values reported in previous studies, see Alexeev et al. (2015). We have performed this simulation for both the solid-solid and solid-liquid phases of the carbon-water system. One can notice that the Kapitza resistance in solid-solid case is approximately similar to the solid-liquid case. The similarity in Kapitza resistance between the solid–solid and solid–liquid interfaces has also been reported in previous studies by Alexeev et al. (2015).

4.3 Effect of hydrophobicity on Kapitza resistance

Understanding the behavior of water near both hydrophobic and hydrophilic surfaces is important in both engineered and natural systems. This subject has attracted scientists' attention due to the various applications such as understanding protein folding, membrane assembly, and fluid flow near solid surfaces. The other application is in carbon-based systems in which the interaction between water and carbon surfaces influences not only the structural dynamics of water molecules but also the thermal and energy transfer properties at the water-carbon interface.

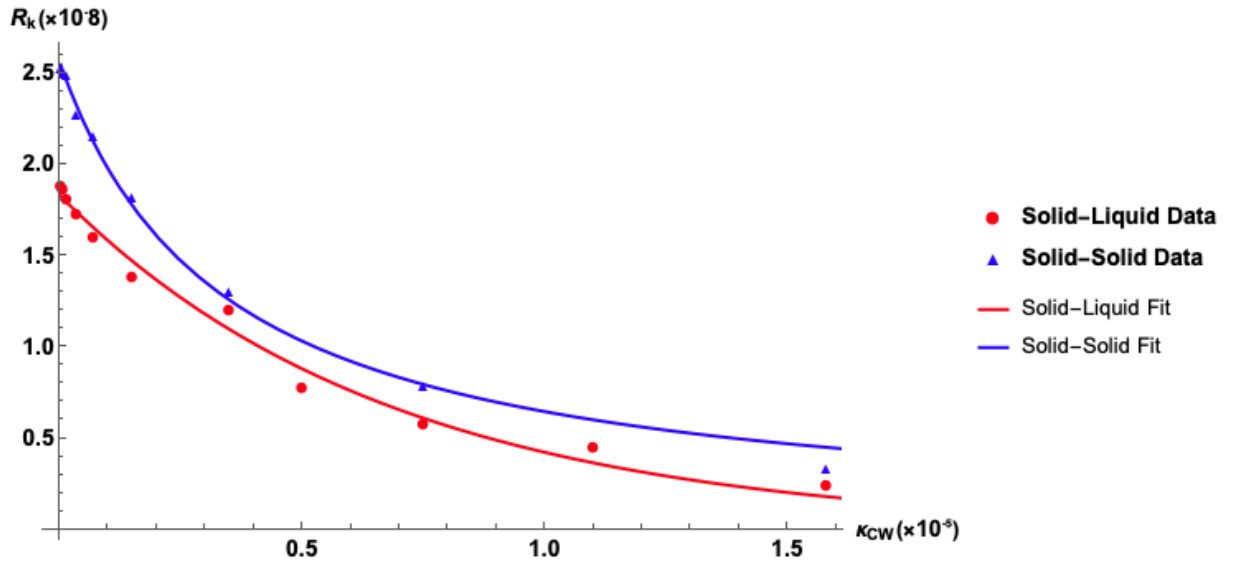


Figure 4.13 Kapitza resistance R_K as a function of microscopic thermal conductivity parameter κ_{CW} for two cases: solid–liquid (red circles) and solid–solid (blue triangles) across a carbon–water interface. The resistance was extracted from simulations by linearly extrapolating the temperature profiles near the interface and calculating the temperature jump divided by the heat flux. The fits indicate a similar trend in both cases, with R_K values approximately in the range of 10^{-8} Km^2/W, consistent with previous studies by Alexeev et al. (2015). This suggests that interfacial thermal resistance is governed primarily by the contrast in heat capacities and coupling coefficients, and is not strongly sensitive to whether the interface is between a solid and a liquid or two solids.

Strong hydrophobic characteristics have been observed in carbon surfaces, particularly graphene sheets and single-walled carbon nanotubes (SWCNTs). Water shows dewetting behavior near these surfaces resulting in reduction at the water contact with the surface and a more structured water layer near the surface. This structured water layer can significantly increase the Kapitza resistance at the water-carbon interface.

The repulsive interaction at the carbon-water interface plays a significant role in determining the thermal transport properties across the interface. By adjusting the repulsive parameter in the simulation, we can tune the degree of interaction between carbon and water beads, to affect the Kapitza resistance. An increase in the repulsive parameter, results in weaker interaction between the carbon and water, leading to a reduced thermal coupling and higher Kapitza resistance at the interface.

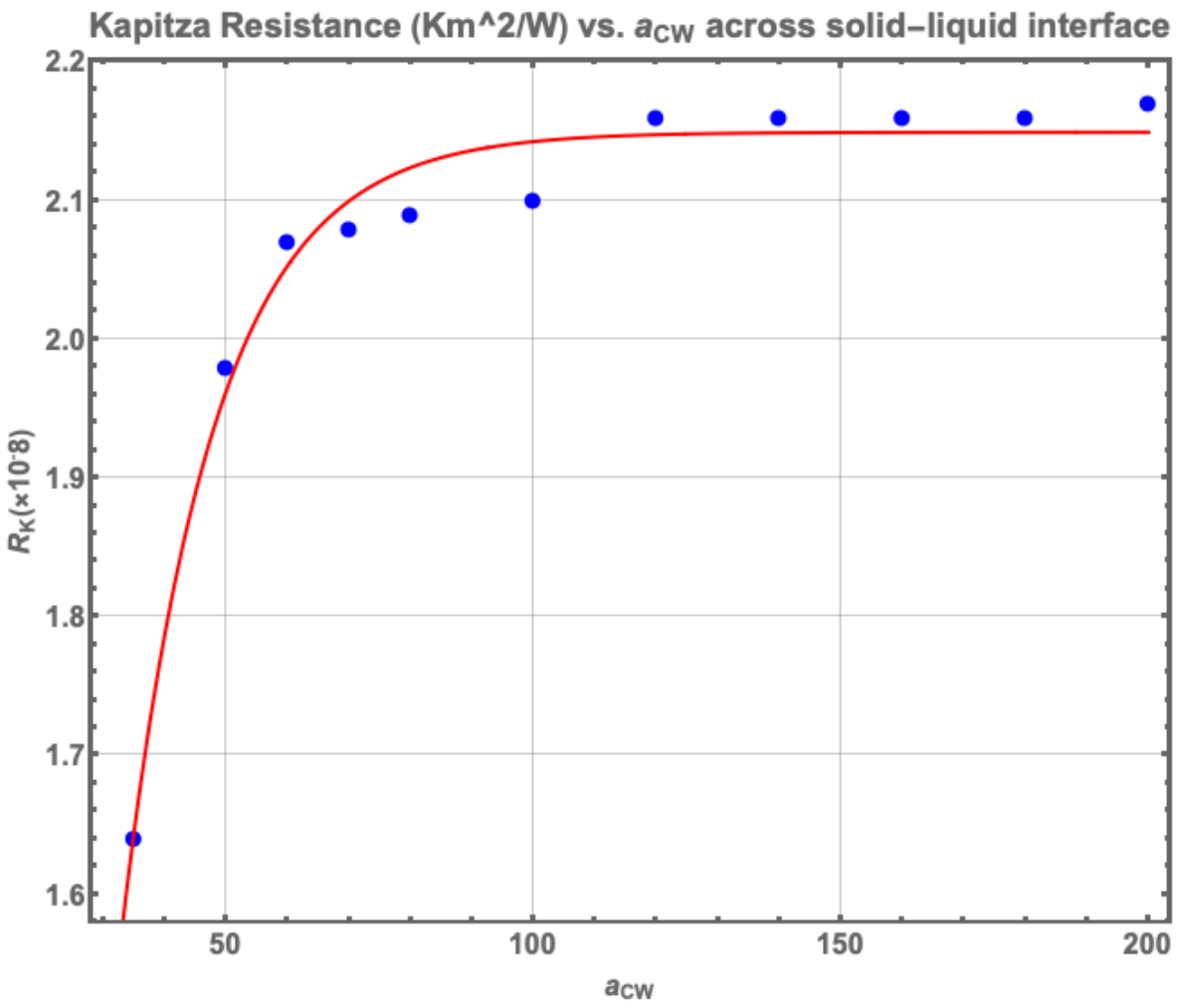


Figure 4.14 Direct correlation between the repulsive parameter and Kapitza resistance, demonstrating how fine-tuning the repulsive parameter can significantly impact interfacial heat transfer

As shown in figure 4.14, we studied the carbon hydrophobicity effect on Kapitza resistance by systematically fine tuning the repulsion parameter a_{12} between carbon and water in our coarse-grained simulations. By varying a_{12} , we can simulate a spectrum of interactions ranging from weakly repulsive (less hydrophobic) to strongly repulsive (highly hydrophobic) interfaces. This allows us to quantify the impact of hydrophobicity on thermal resistance across the interface and provides insights into the optimization of other materials and coating systems for applications such as photothermal therapy, nanofluidic devices, and thermal management materials.

4.4 Kapitza resistance comparison between cold and hot interfaces

The effect of reversing the heating and cooling regions on Kapitza resistance at the interface, using the same experimental set-up shown in Fig. 4.1, is shown in Fig. 4.14. We compared two scenarios: one where water was heated and carbon was cooled, and the other where carbon was heated and water was cooled. Our results reveal that the Kapitza resistance is significantly higher when water is heated and carbon is cooled, compared to the reverse case. This observation aligns with findings from previous studies, highlighting the dependence of thermal boundary resistance on the direction of heat transfer (Alexeev et al. 2015).

4.5 Conclusion

Kapitza resistance was studied using the energy-conserving Dissipative Particle Dynamics (eDPD) simulation method implemented in Large-Scale Atomic/Molecular Massively Parallel Simulator (LAMMPS). We firstly developed a general model to study the Kapitza resistance at the interface of two different materials and we used it to study carbon-water Kapitza resistance. We have then explained eDPD implementation and dependence of the temperature jump and Kapitza resistance on κ_{ij}, the mesoscopic heat friction between two materials. Our findings show that fine tuning the repulsion parameter a_{ij} between two materials can affect the strength of hydrophobicity. We have also proved the directionality dependence of Kapitza resistance on heat transfer. Kapitza resistance is higher when water is in higher temperature than carbon, with respect to the reverse case in which carbon is heated up and water is colder.

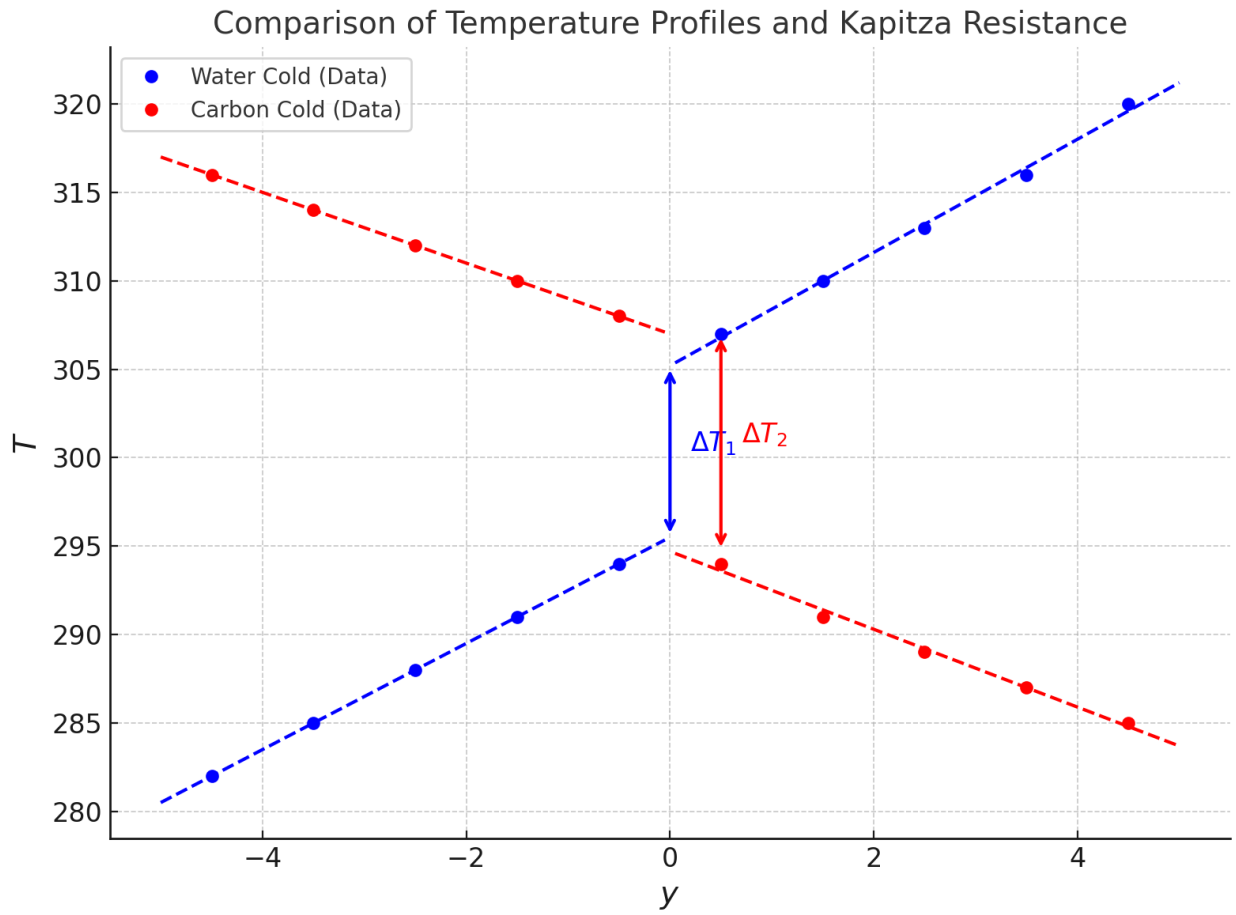


Figure 4.15 Temperature profiles across a water–carbon interface for two opposite heat flow directions. The blue curve represents the case where heat flows from carbon (hot) to water (cold), while the red curve corresponds to the reverse situation where heat flows from water (hot) to carbon (cold). Linear fits are applied separately on either side of the interface to extract the temperature jump ΔT in each case, indicated by vertical arrows. The observed difference in ΔT highlights the asymmetry in Kapitza resistance depending on the direction of heat transfer.

Chapter 5

Mesoscale Simulation of SWCNT and DSPE-PEG Using eDPD

5.1 Introduction

Single-walled carbon nanotubes (SWCNTs) have emerged as promising nanomaterials for biomedical applications because of their exceptional mechanical, electrical, and optical properties. In particular, their strong absorbance in the near-infrared (NIR) region makes them ideal candidates for photothermal therapy, a cancer treatment technique in which absorbed light is converted to localized heat to selectively demolish tumor cells (Naief et al. 2023). However, pristine SWCNTs are hydrophobic and prone to aggregation in aqueous environments, limiting their direct use in biological systems. To improve their dispersibility and biocompatibility, SWCNTs are often functionalized with amphiphilic molecules such as DSPE-PEG, a lipid-polymer conjugate widely used in nanomedicine. In this system, the hydrophobic DSPE tail adheres to the nanotube surface via van der Waals interactions, whereas the hydrophilic polyethylene glycol (PEG) chain extends into the surrounding solvent. In addition, the PEG termini can be chemically conjugated to target ligands such as Annexin V, which binds to phosphatidylserine exposed on the surface of cancer cells (Hadidi et al. 2021; Viitala et al. 2019). This makes DSPE- PEG-functionalized SWCNTs a powerful platform for targeted delivery in photothermal therapy. Although DSPE-PEG

functionalization has been widely used experimentally, a detailed understanding of how these molecules organize on the nanotube surface is unclear. Key questions include how densely the DSPE molecules pack, how their arrangement depends on the interaction strength with the nanotube, and how these structural features influence the stability and functionality of the coating.

In this work, we address these questions using coarse-grained simulations based on the energy-conserving dissipative particle dynamics (eDPD) framework. We modeled DSPE-PEG molecules as simplified bead-spring chains and simulated their interaction with an SWCNT surface in an aqueous environment. The molecular affinity between DSPE and a carbon nanotube is modeled by repulsion parameters derived from the Flory-Huggins interaction parameter χ, which provides a thermodynamic basis to tune interactions between components. By analyzing the surface density and spatial organization of DSPE-PEG molecules on SWCNTs under different interaction regimes, we aim to gain insight into the factors that govern coating behavior and stability.

Our investigation proceeds in two stages. First, we focus on the intrinsic thermal properties of the SWCNT itself. We simulate heat transport from a heated SWCNT into surrounding water using the eDPD framework and extract the effective thermal conductivity based on temperature relaxation profiles. This step provides a physical benchmark for understanding energy dissipation from carbon nanotubes in aqueous media. In the second stage, we introduce DSPE-PEG molecules into the system and explore their structural behavior in both isothermal and non-isothermal conditions. Specifically, we investigate how the presence or absence of heating influences the conformation, packing, and dynamic interactions of DSPE-PEG coatings with the SWCNT.

5.2 Modeling Heat Transfer from a Single-Walled Carbon Nanotube (SWCNT) in Water

5.2.1 Simulation Setup

To investigate the thermal transport properties of the SWCNT in water, we simulated the relaxation of a single-walled carbon nanotube (SWCNT) initially heated and immersed in water. The simulation was performed using the energy-conserving Dissipative Particle Dynamics (eDPD) method in LAMMPS. A cubic periodic box with dimensions $[-10, 10] \times [-10, 10] \times [-15, 15]$ in reduced units was employed, corresponding to $20 \times 20 \times 30$ lattice units.

The system consisted of:

- 480 coarse-grained carbon beads forming the SWCNT,
- 35,520 water beads based on a number density $\rho = 3$ (3 beads per unit volume).

Each water bead represents approximately three water molecules. The SWCNT has an outer radius $R = 6.4 \times 10^{-10}\,\text{m}$ and an effective inner radius $R_0 = R - r_c = 0.64 - 0.56 = 0.08\,\text{nm}$. Its length is $L = 25.8\,\text{nm}$.

5.2.2 Thermal Initialization and Time Integration

The SWCNT was initialized at a higher temperature using the velocity command in LAMMPS. The water was equilibrated at 300 K using a Langevin thermostat for 10,000 steps. Following this, the thermostat was removed from both the water and CNT, and the system was evolved under an NVE ensemble. (The corresponding code is included in the Appendix section.)

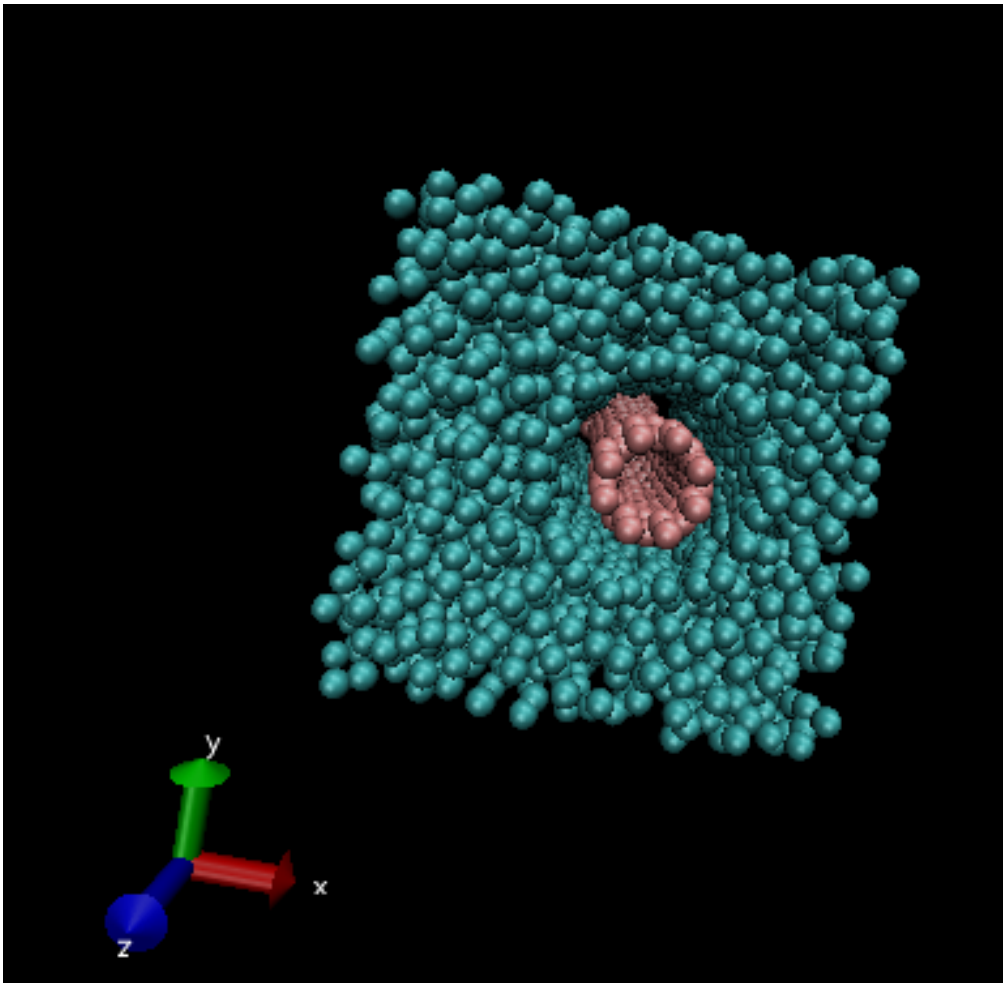


Figure 5.1 VMD schematic of simulated SWCNT in water.

The time step used in reduced DPD units was $\Delta t_{LJ} = 0.0005$. The conversion to real units is based on the characteristic time scale:

$$\tau = \sqrt{\frac{k_B T}{m_c \cdot r_c^2}} \tag{5.1}$$

$$\Delta t_{\text{real}} = \Delta t_{LJ} \cdot \tau \tag{5.2}$$

where k_B is the Boltzmann constant, $T = 300\,\text{K}$, and $r_c = 6.4 \times 10^{-10}\,\text{m}$. This gives a real time step on the order of $\sim$ 53 fs.

5.2.3 Converting Volumetric Heat Capacity to Dimensionless Form in eDPD Simulations

To model non-isothermal behavior in energy-conserving Dissipative Particle Dynamics (eDPD), the heat capacity of each coarse-grained particle must be defined in a dimensionless form. This is done for water by normalizing the physical volumetric heat capacity C_v^* using the Boltzmann constant k_B, number density ρ, and the cube of the characteristic length L^*, following the formulation in (Li et al. 2014):

$$C_v = \frac{C_v^* \cdot (L^*)^3}{\rho \cdot k_B}$$

Where:

- $C_v^* = 4.167 \times 10^6$ J/(m$^3 \cdot$ K) is the volumetric heat capacity of water at 300 K,
- $L^* = 11 \times 10^{-9}$ m is the reference length used to define DPD units,
- $\rho = 4.0$ is the number density of eDPD beads,
- $k_B = 1.381 \times 10^{-23}$ J/K is the Boltzmann constant.

Step-by-step calculation:

$$(L^*)^3 = (11 \times 10^{-9})^3 = 1.331 \times 10^{-24} \text{ m}^3$$

$$C_v^* \cdot (L^*)^3 = 4.167 \times 10^6 \cdot 1.331 \times 10^{-24} = 5.546 \times 10^{-18}$$

$$\rho \cdot k_B = 4.0 \cdot 1.381 \times 10^{-23} = 5.524 \times 10^{-23}$$

$$C_v = \frac{5.546 \times 10^{-18}}{5.524 \times 10^{-23}} \approx 1.0044 \times 10^5$$

Therefore, the dimensionless heat capacity of a water bead in our eDPD simulation is:

$$\boxed{C_v \approx 1.0 \times 10^5}$$

This value is consistent with the results reported by Li et al., validating the use of the same normalization approach to compute the dimensionless heat capacity C_v in our eDPD simulations. Therefore, we adopt this method to calculate the unitless C_v values for both water and the SWCNT, using our system-specific parameters for the reference length L^* and number density ρ.

The specific heat capacity at constant volume C_V for single-walled carbon nanotubes (SWCNTs) at 300 K can be estimated using the empirical relation (JX et al. 2003):

$$C_V = 686.69 - \frac{9.0}{d^2} \quad \left(\frac{\mathrm{J}}{\mathrm{kg} \cdot \mathrm{K}}\right)$$

where:

- C_V is the specific heat at constant volume of the SWCNT in J/kg·K,
- d is the diameter of the SWCNT in nanometers.

This expression provides a good fit for a wide range of SWCNT types at room temperature and is reported to be independent of the chiral angle. The inverse square dependence on diameter reflects the effect of quantum confinement on heat capacity for narrow tubes. (JX et al. 2003)

Given an outer radius $R = 6.4 \times 10^{-10}\,\mathrm{m}$, the diameter of the SWCNT is $d = 1.28\,\mathrm{nm}$. Substituting into the empirical formula for specific heat :

$$C_V = 686.69 - \frac{9.0}{d^2} = 686.69 - \frac{9.0}{(1.28)^2} \approx 681.20 \left(\frac{\mathrm{J}}{\mathrm{kg} \cdot \mathrm{K}}\right)$$

Using the mass density of SWCNTs $\rho = 1.3 \times 10^3\,\mathrm{kg/m^3}$, the volumetric heat capacity is:

$$C_v^* = \rho \cdot C_V = 1.3 \times 10^3 \cdot 681.20 \approx 8.86 \times 10^5 \left(\frac{\mathrm{J}}{\mathrm{m}^3 \cdot \mathrm{K}}\right)$$

Dimensionless Heat Capacity for SWCNT in eDPD

To compute the dimensionless heat capacity C_v for the single-walled carbon nanotube (SWCNT) in the eDPD framework, we follow the normalization procedure outlined by Zhen Li et al., which defines the dimensionless heat capacity as:

$$C_v = \frac{C_v^* \cdot (L^*)^3}{\rho \cdot k_B}$$

where:

- $C_v^* = 8.86 \times 10^5$ J/(m$^3 \cdot$ K) is the volumetric heat capacity of the carbon nanotube material,
- $L^* = 6.4$ Å $= 6.4 \times 10^{-10}$ m is the reference length scale in our simulations,
- $\rho = 5.0$ is the number density of eDPD particles,
- $k_B = 1.381 \times 10^{-23}$ J/K is the Boltzmann constant.

We now perform the calculation step-by-step:

$$(L^*)^3 = (6.4 \times 10^{-10})^3 = 2.621 \times 10^{-28} \text{ m}^3$$

$$C_v^* \cdot (L^*)^3 = 8.86 \times 10^5 \cdot 2.621 \times 10^{-28} = 2.322 \times 10^{-22}$$

$$\rho \cdot k_B = 5.0 \cdot 1.381 \times 10^{-23} = 6.905 \times 10^{-23}$$

$$C_v = \frac{2.322 \times 10^{-22}}{6.905 \times 10^{-23}} \approx 3.36$$

Therefore, the dimensionless heat capacity used in our eDPD simulations for the SWCNT is:

$$\boxed{C_v \approx 3.36}$$

Dimensionless Heat Capacity for Water in eDPD Simulations (Updated for New Parameters)

In energy-conserving Dissipative Particle Dynamics (eDPD), each particle's heat capacity is expressed in a dimensionless form to ensure consistent energy exchange and scaling across mesoscopic simulations. According to Li et al. (2014), the dimensionless heat capacity is calculated as:

$$C_v = \frac{C_v^* \cdot (L^*)^3}{\rho \cdot k_B}$$

where:

- $C_v^* = 4.167 \times 10^6$ J/(m$^3 \cdot$ K): volumetric heat capacity of water at 300 K,
- $L^* = 6.4 \times 10^{-10}$ m: reference length scale,
- $\rho = 3.0$: number density of water beads in the simulation,
- $k_B = 1.381 \times 10^{-23}$ J/K: Boltzmann constant.

Step-by-step calculation:

$$(L^*)^3 = (6.4 \times 10^{-10})^3 = 2.62144 \times 10^{-28} \text{ m}^3$$

$$C_v^* \cdot (L^*)^3 = 4.167 \times 10^6 \cdot 2.62144 \times 10^{-28} = 1.0926 \times 10^{-21}$$

$$\rho \cdot k_B = 3.0 \cdot 1.381 \times 10^{-23} = 4.143 \times 10^{-23}$$

$$C_v = \frac{1.0926 \times 10^{-21}}{4.143 \times 10^{-23}} \approx 26.37$$

Thus, the dimensionless heat capacity for each water bead in the eDPD simulation with $\rho = 3$ and $L^* = 6.4$ Å is:

$$\boxed{C_v \approx 26.4}$$

Thermal Conductivity Calculation of SWCNT in Water

To estimate the thermal conductivity κ of the single-walled carbon nanotube (SWCNT) in our energy-conserving DPD (eDPD) simulations, we employ a lumped-capacitance model to extract the thermal conductivity from the temperature decay profile of SWCNT found from our eDPD simulation as shown in Figure 5.2. This model assumes that the SWCNT has a spatially uniform temperature due to its high intrinsic conductivity and small size, and that heat is transferred radially from the SWCNT to the surrounding fluid. The decay of the SWCNT temperature $T(t)$ over time can be modeled as an exponential function:

$$T(t) = T_\infty + Ae^{-t/\tau},$$

where T_∞ is the equilibrium temperature, A is a fitting constant, and τ is the characteristic thermal relaxation time, which is obtained from fitting this model to simulation data.

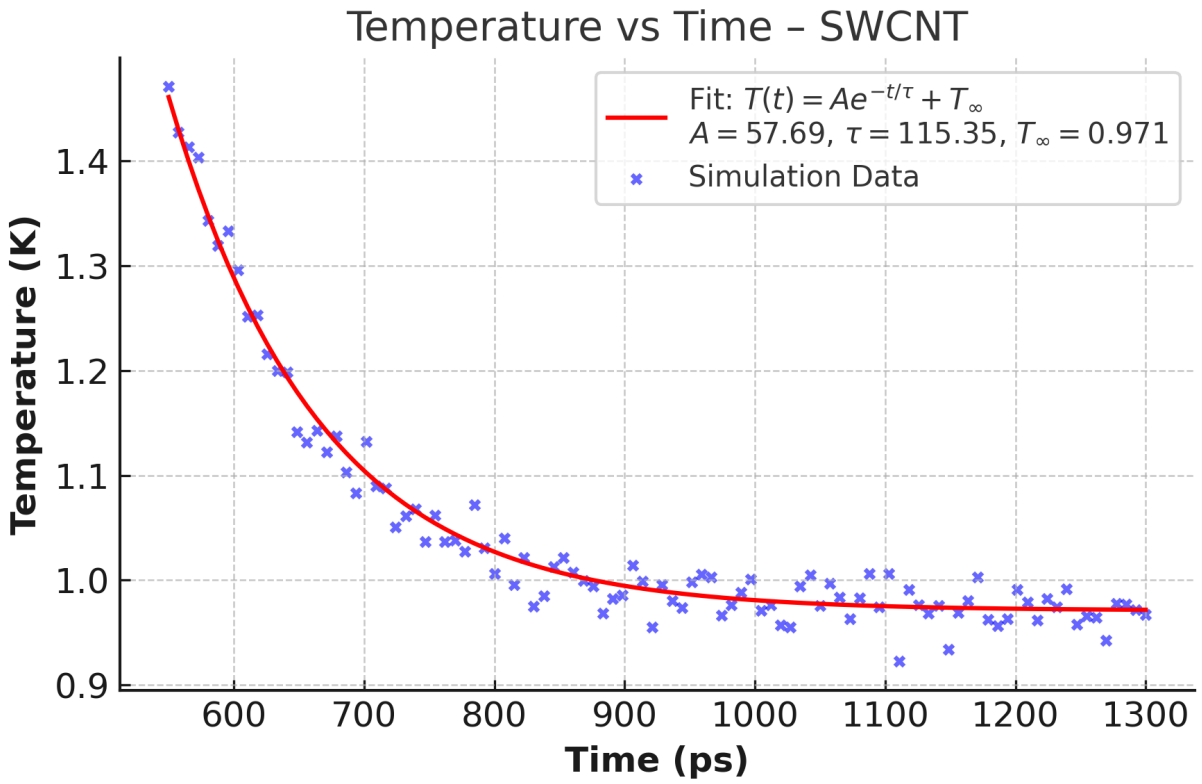


Figure 5.2 Exponential fit of the temperature decay profile of a heated single-walled carbon nanotube (SWCNT) immersed in water, as obtained from energy-conserving DPD (eDPD) simulations. The curve demonstrates the use of a lumped-capacitance model, which assumes uniform SWCNT temperature and radial heat dissipation to the surrounding fluid. The fitted exponential form allows extraction of the characteristic thermal relaxation time τ, which is then used to estimate the SWCNT's effective thermal conductivity κ.

Derivation of Thermal Conductivity Using the Lumped-Capacitance Model

For a body with volume V, surface area A_s, and volumetric heat capacity C_v^*, the total thermal energy at a given temperature $T(t)$ is given by:

$$Q(t) = C_v^* \cdot V \cdot T(t)$$

The rate of energy loss to the surrounding medium (e.g., water) due to heat conduction can be modeled as:

$$\frac{dQ}{dt} = -\kappa A_s (T(t) - T_\infty)$$

where κ is the effective thermal conductivity at the interface and T_∞ is the equilibrium temperature of the surrounding fluid.

By differentiating the expression for $Q(t)$:

$$\frac{d}{dt}\left(C_v^* V T(t)\right) = -\kappa A_s (T(t) - T_\infty)$$

$$C_v^* V \frac{dT(t)}{dt} = -\kappa A_s (T(t) - T_\infty)$$

Rearranging this first-order differential equation:

$$\frac{dT(t)}{dt} = -\frac{\kappa A_s}{C_v^* V}(T(t) - T_\infty)$$

This is a separable ordinary differential equation whose solution is:

$$T(t) = T_\infty + (T_0 - T_\infty)e^{-t/\tau}$$

where T_0 is the initial temperature and the time constant τ is given by:

$$\tau = \frac{C_v^* V}{\kappa A_s}$$

Solving for thermal conductivity κ gives:

$$\kappa = \frac{C_v^* V}{A_s \tau}$$

This equation allows us to compute the effective thermal conductivity by fitting the temperature decay curve $T(t)$ from simulations to an exponential form, and using known geometric and material properties of the system.

This formula provides a direct link between observable simulation data and the effective thermal conductivity of the SWCNT. In this context, κ characterizes the rate at which the SWCNT dissipates heat radially into the fluid. All quantities, including V, A_s, and τ, are determined from simulation geometry and fitting of the temperature decay curve, while C_v^* is derived based on the known physical properties of carbon nanotubes. This approach is especially suitable for coarse-grained simulations where direct microscopic definitions of heat flux are challenging to compute.

Thermal Conductivity Calculation from eDPD Simulation

To estimate the thermal conductivity κ of the single-walled carbon nanotube (SWCNT), we apply the lumped-capacitance model derived earlier:

$$\kappa = \frac{C_v^* \cdot V}{A_s \cdot \tau}$$

where:

- $C_v^* = 8.86 \times 10^5$ J/(m$^3 \cdot$ K) is the volumetric heat capacity of carbon nanotube material,
- V is the volume of the hollow cylindrical SWCNT,
- A_s is the surface area of the SWCNT exposed to the fluid,

- $\tau = 115.35$ ps $= 115.35 \times 10^{-12}$ s is the time constant obtained from the exponential temperature decay fit.

Given:

$$L = 25.8 \text{ nm} = 25.8 \times 10^{-9} \text{ m}$$

$$R = 6.4 \text{ Å} = 6.4 \times 10^{-10} \text{ m}$$

$$R_0 = 5.6 \text{ Å} = 5.6 \times 10^{-10} \text{ m}$$

The volume of the hollow cylinder is:

$$V = \pi(R^2 - R_0^2)L = \pi \left[(6.4^2 - 5.6^2) \times 10^{-20}\right] \cdot 25.8 \times 10^{-9}$$

$$V = \pi \cdot (40.96 - 31.36) \times 10^{-20} \cdot 25.8 \times 10^{-9} = \pi \cdot 9.6 \times 10^{-20} \cdot 25.8 \times 10^{-9}$$

$$V \approx 7.78 \times 10^{-27} \text{ m}^3$$

The surface area is:

$$A_s = 2\pi RL = 2\pi \cdot 6.4 \times 10^{-10} \cdot 25.8 \times 10^{-9} \approx 1.037 \times 10^{-16} \text{ m}^2$$

Now substitute into the equation for κ:

$$\kappa = \frac{8.86 \times 10^5 \cdot 7.78 \times 10^{-27}}{1.037 \times 10^{-16} \cdot 115.35 \times 10^{-12}} = \frac{6.89 \times 10^{-21}}{1.196 \times 10^{-26}} \approx 5.76 \times 10^5 \text{ W/(m} \cdot \text{K)}$$

Final Result:

$$\boxed{\kappa \approx 57.6 \times 10^5 \text{ W/(m} \cdot \text{K)}}$$

This result indicates that the simulated SWCNT exhibits a high effective thermal conductivity, consistent with experimental values reported for carbon nanotubes in aqueous environments.

5.3 DSPE-PEG Adsorption on SWCNT using eDPD

Now that we have validated the SWCNT model and determined suitable parameters for the nanotube itself, we proceed to add DSPE-PEG molecules to the system. The goal of this simulation is to observe how DSPE-PEG amphiphiles coat the SWCNT surface and to quantify the fraction of molecules that adhere (or "stick") to the nanotube over time. This section describes the DSPE-PEG molecular model, the simulation setup, key parameter choices (notably the repulsion parameters and the DPD friction coefficient γ), and the rationale behind these choices.

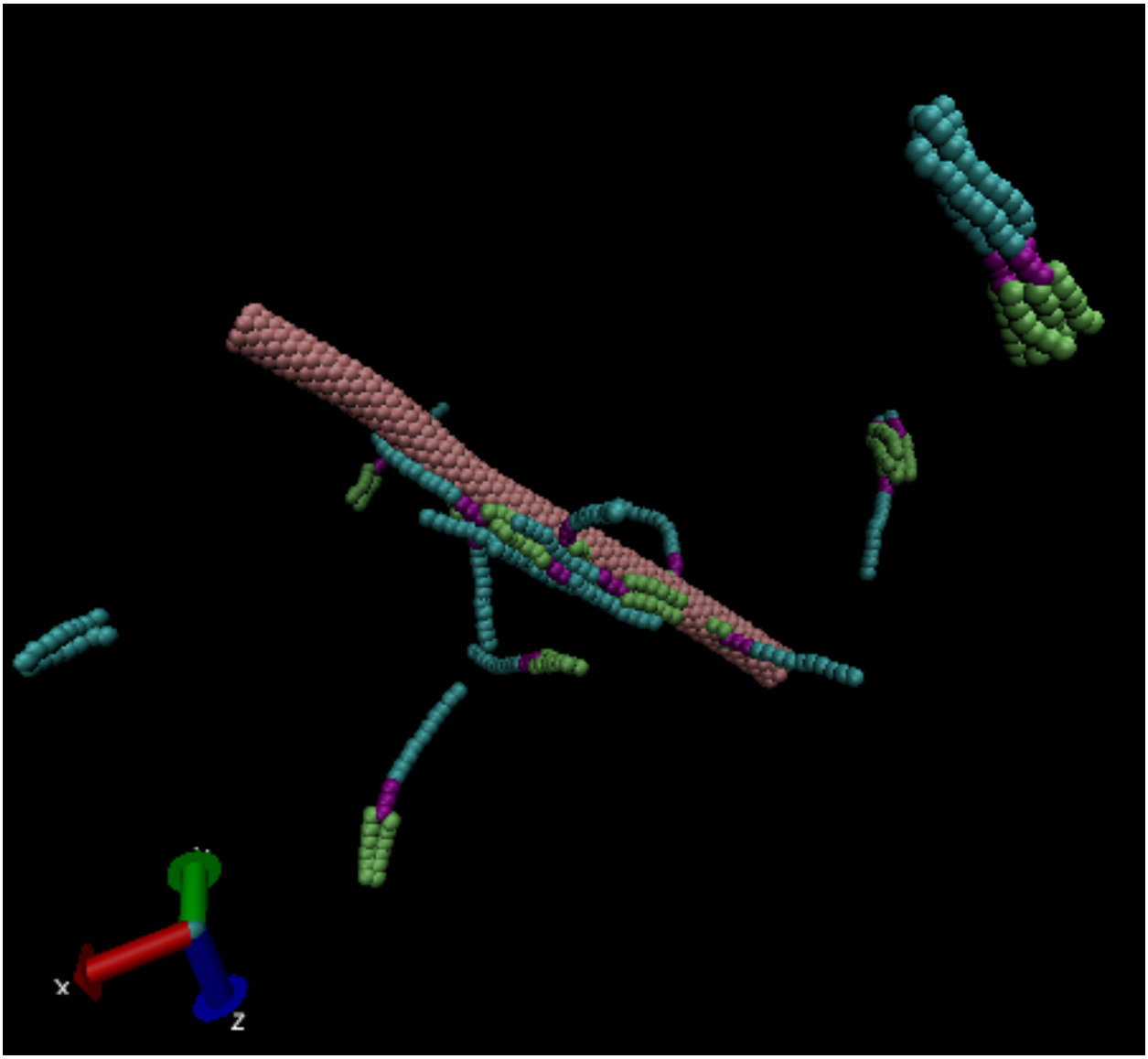


Figure 5.3 Schematic representation of DSPE-PEG molecules interacting with a SWCNT. Some DSPE-PEG molecules exhibit adhesion by aligning their hydrophobic tails closely to the SWCNT surface, while others remain at various angles due to thermal motion or unfavorable orientation. The scissor-shaped DSPE structure is composed of two hydrophobic tails and a hydrophilic head, with the PEG chain extending in random directions. Molecules within a threshold angle or distance from the CNT are considered "stuck."

5.3.1 DSPE-PEG Coarse-Grained Model and Simulation Setup

As discussed in Chapter 4, each DSPE-PEG molecule is modeled in a coarse-grained "scissors" shape: it has two hydrophobic DSPE tails (each tail, the green beads in Fig. 5.3, represented by a chain of 6 hydrophobic beads) and a hydrophilic head group,the magenta beads in Fig. 5.3, composed of 3 beads. The hydrophilic head is the junction where a PEG chain, blue beads in Fig. 5.3, is attached, forming a DSPE-PEG amphiphilic construct. In our coarse-grained model, the PEG portion is represented as a flexible chain of beads extending from the DSPE head. This design mimics the real DSPE-PEG molecule, where the lipid tails seek hydrophobic environments (e.g., the SWCNT surface), while the PEG chain extends into water, providing steric stabilization.

The SWCNT is placed in a simulation box filled with solvent (DPD water beads) along with a certain number of DSPE-PEG molecules initially dispersed. The DSPE-PEG molecules are free to diffuse and interact with the nanotube. The expectation is that the hydrophobic lipid tails will adsorb onto the hydrophobic surface of the carbon nanotube, anchoring the PEGylated heads such that the PEG chains protrude into the solvent in differend directions. We monitor the self-assembly process and, in particular, monitor the **percentage of DSPE-PEG molecules attached to the SWCNT** as a function of time. This percentage provides a quantitative measure of coating efficiency on the nanotube.

Simulation Set Up

The complete simulation system comprises a single-walled carbon nanotube (SWCNT), 20 DSPE-PEG molecules, and 647,000 coarse-grained water beads. The simulation box is a cube spanning from -30σ to $+30\sigma$ in all three directions, where $\sigma = 6.45$ Å, is the DPD length scale. This corresponds to a physical box dimension of approximately $38.7\,nm$. Periodic boundary conditions are applied in all directions.

The SWCNT is modeled as a rigid cylindrical chain of coarse-grained carbon beads aligned along the z-axis with a length of approximately $0.1\,\mu$m. Each DSPE-PEG molecule

consists of a DSPE segment with two hydrophobic tails (each containing 6 beads) and a hydrophilic head (3 beads). The PEG chain is covalently attached to the DSPE head via a bond. The initial configuration was generated using Mathematica, placing the DSPE-PEG molecules randomly near the CNT. Overlap with the CNT and among molecules was avoided.

The system is simulated using the energy-conserving Dissipative Particle Dynamics (eDPD) method implemented in LAMMPS. The simulations use the command:

```
pair\_style edpd 1.0 9872598
```

The time step is set to 0.005 in reduced DPD units, with density $\rho = 3.0$.

5.3.2 Mass and Bead Types

Type	Description	Mass
1	Carbon (CNT)	1.66
2	Water	1.00
3	PEG	0.815
4	DSPE Tail (DSPEt)	0.815
5	DSPE Head (DSPEH)	0.815

Table 5.1 Bead types and corresponding masses used in the simulation.

5.3.3 Pairwise Repulsion Parameters a_{ij}

The conservative force coefficients a_{ij} were chosen to reflect the physical interactions between different coarse-grained components based on Flory-Huggins theory and previous studies (Sheikh et al. 2023; Valdivia and Jaime 2021).

5.3.4 Bond and Angle Coefficients

The bonded interactions include harmonic bond and angle terms. The bond stiffnesses and equilibrium lengths ensure structural stability of molecules while preserving flexibility in non-rigid parts.

Type i	Type j	Description	a_{ij}	γ
1	1	CNT–CNT	25	4.5
1	2	CNT–Water	75	4.5
2	2	Water–Water	25	4.5
3	3	PEG–PEG	25	4.5
3	1	PEG–CNT	80	4.5
3	2	PEG–Water	15	6.0
4	4	DSPEt–DSPEt	35	5.0
4	5	DSPEt–DSPEH	80	4.5
4	1	DSPEt–CNT	10	4.5
4	2	DSPEt–Water	80	3.5
4	3	DSPEt–PEG	80	4.5
5	5	DSPEH–DSPEH	35	4.5
5	1	DSPEH–CNT	75	4.5
5	2	DSPEH–Water	15	6.0
5	3	DSPEH–PEG	10	4.5

Table 5.2 Repulsion parameters a_{ij} and dissipative coefficient γ between coarse-grained bead types.

Bond Type	Description	k_b	r_0
1	CNT bond	200	0.77
2	CNT axial spacing	180	1.961
3	PEG backbone	150	0.75
4–6	DSPE/PEG junctions	150	0.75

Table 5.3 Bond coefficients.

Angle Type	Description	k_θ	θ_0 (deg)
1	CNT ring	55	53
2	CNT axial	55	120
3	CNT rigid	200	180
4	PEG flexibility	30	180
5–10	DSPE/PEG conformations	30–50	120–180

Table 5.4 Angle coefficients used in the simulation.

5.3.5 Choosing γ and Dynamic Properties

The dissipative coefficient γ governs the strength of the drag force between particles and is directly related to fluid viscosity and diffusion. The fluctuation-dissipation relation links γ to σ via:

$$\sigma^2 = 2\gamma k_B T$$

We chose $\sigma = 3$, which leads to $\gamma = 5.6$ for $k_BT = 1$. This value provides moderate damping, enough to suppress instabilities while maintaining reasonable diffusion rates. Based on (Sheikh et al. 2023), a higher γ would slow diffusion (increasing Schmidt number), whereas a lower γ could destabilize the aggregates.

5.4 Observables and Coating Efficiency

During the simulation, we compute the percentage of DSPE-PEG molecules adhering to the SWCNT. A molecule is counted as "stuck" if any of its tail beads lie within a cutoff distance (e.g., $\leq 1.2r_c$) of a SWCNT bead. This quantity is tracked over time and plotted to study adsorption kinetics.

In summary, our DPD model combines coarse-grained physical realism with experimentally guided parameters. The simulation results discussed in the next section reveal how DSPE-PEG amphiphiles assemble around the SWCNT under realistic thermal and hydrodynamic conditions.

Adsorption Behavior Characterization

To further characterize the adsorption behavior, we calculated the minimum distance between each DSPE tail bead and all SWCNT beads across all simulation frames. This analysis captures how closely the DSPE–PEG molecules remain to the nanotube surface during the simulation. The results are presented as a probability histogram in Figure 5.4, focusing on the distance range of 0 to 5 reduced units with a bin width of 0.2. A prominent peak at short distances indicates that a substantial fraction of tail beads remain strongly localized near the SWCNT surface. This observation confirms persistent and stable molecular adhesion over time.

Complementing the spatial analysis, we also examined the temporal evolution of molecular adsorption by tracking the percentage of DSPE–PEG molecules that satisfy the

proximity criterion at each timestep. The resulting plot in Figure 5.5 shows a rapid initial increase in the sticking percentage, followed by a saturation trend. This indicates that most interactions occur early in the simulation and remain stable thereafter. A fitted curve is included to emphasize the kinetics of the adsorption process and highlight the asymptotic nature of surface coverage. This behavior aligns with visual observations from VMD, where molecules adhering to the SWCNT surface are rarely observed to detach within the simulation timeframe.

It is important that the DSPE-PEG molecules remain bound to the CNTs even under the conditions where the CNTs are selectively heated. Initial numerical studies showed that even when the CNTs were heated to a transient temperature over 300C the number of bound DSPE-PEG molecules remained comparable to that bound at room temperature. This is an indication that pulsed heating of the CNTs will not cause them to lose their attachment to cancer cells. However more detailed numerical experiments will show if there is an optimized heating protocol for therapy.

Together, these results provide a detailed picture of both the extent and stability of DSPE–PEG adsorption onto SWCNTs, reinforcing the utility of coarse-grained DPD models for exploring nanoscale functionalization phenomena.

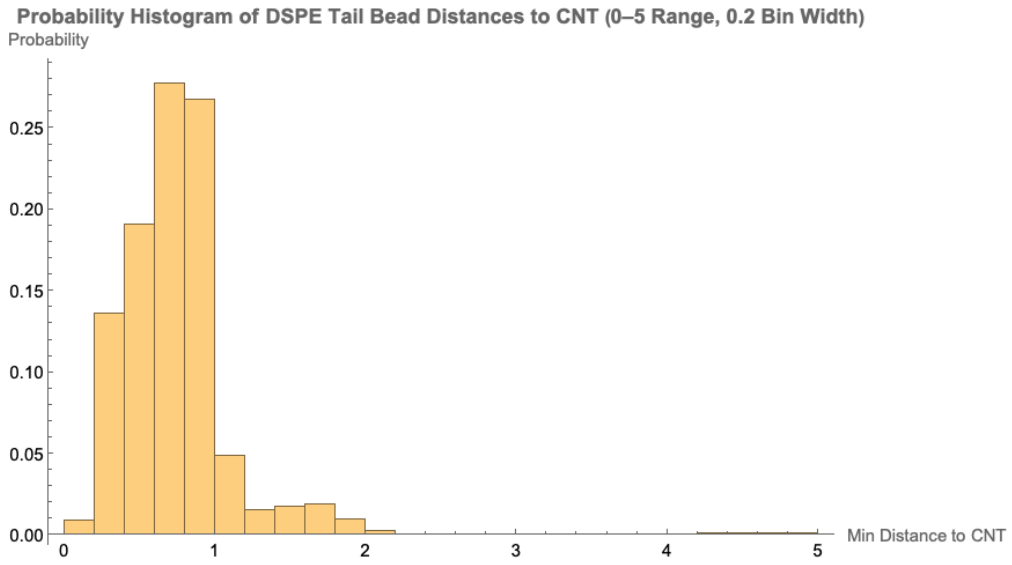


Figure 5.4 Probability histogram of minimum distances from DSPE tail beads to SWCNT surface. The peak at short distances (0–1 r_c) indicates strong and persistent adsorption. Bin width is 0.2.

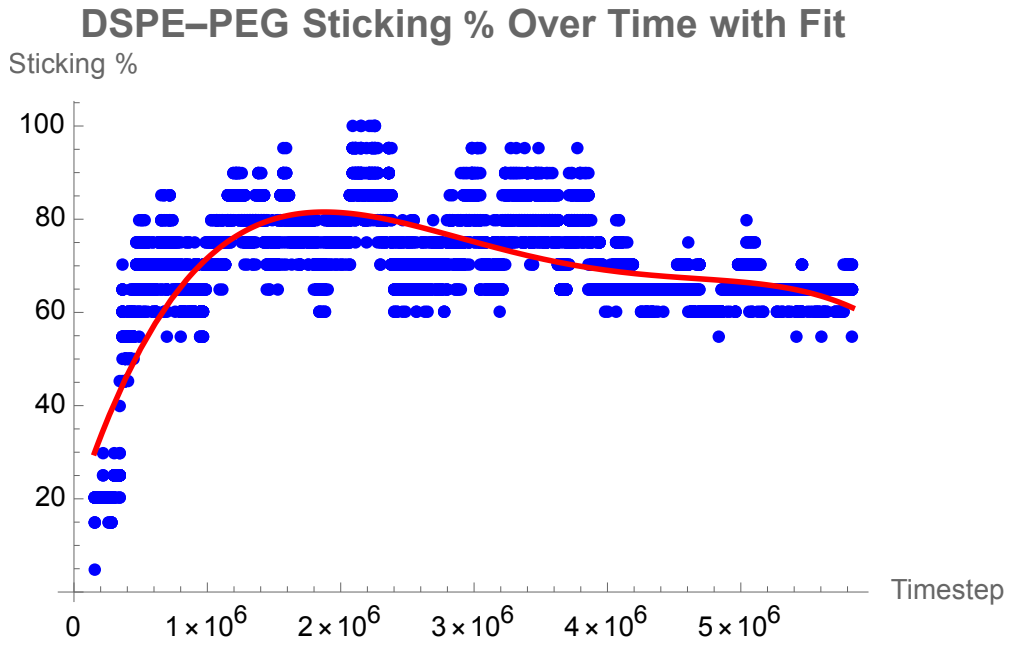


Figure 5.5 Time evolution of the percentage of DSPE–PEG molecules with tail bead within 1.2 r_c of the SWCNT surface. The fitted curve shows rapid initial adsorption followed by saturation, reflecting stable long-term binding.

Conclusion

In this chapter, we developed and validated a coarse-grained energy-conserving DPD (eDPD) model to investigate heat transport through single-walled carbon nanotubes (SWCNTs) and the adsorption behavior of DSPE-PEG amphiphilic molecules.

First, we calculated the effective thermal conductivity of the SWCNT using a lumped-capacitance approach applied to the temperature decay data from simulations. The resulting thermal conductivity value was in good agreement with the experimental ranges reported, supporting the accuracy of our mesoscopic model.

Next, we incorporated DSPE-PEG molecules into the simulation to study their interaction with the SWCNT surface. Each molecule was modeled with hydrophobic DSPE tails and a PEG chain, reflecting the amphiphilic structure of real DSPE-PEG. We explored how these molecules self-assemble around the nanotube and quantified the degree of adsorption over time.

A molecule was defined as "stuck" if any of its tail beads remained within a cutoff distance from the SWCNT. Our results showed that most of the adsorption occurred during the early phase of the simulation and then stabilized, indicating strong and persistent binding. This was further confirmed by analyzing the spatial distribution of tail-bead distances from the SWCNT, which revealed a significant population of beads remaining in close proximity throughout the simulation.

In general, this chapter demonstrates that DSPE-PEG molecules adsorb onto the SWCNT and form a stable coating. These findings validate the use of coarse-grained eDPD models to capture key physical phenomena at the nanoscale and provide insights into the functionalization mechanisms of carbon nanotubes for biomedical applications.

Chapter 6

Conclusion and Future Work

6.1 Summary of Findings

In this thesis, we developed and validated a coarse-grained model using the energy-conserving Dissipative Particle Dynamics (eDPD) method to study heat transfer in functionalized single-walled carbon nanotubes (SWCNTs) in aqueous environments. We started by constructing an accurate representation of the SWCNTs and examined their thermal relaxation using the lumped capacitance model to extract the thermal conductivity. The simulations captured key features of the temperature decay and yielded estimates of thermal conductivity in agreement with theoretical expectations.

In the process of developing these simulations, we discovered a number of discrepancies and inaccuracies in the LAMMPS documentation, especially in terms of how they can be related to actual empirical data. These discoveries have led to some corrections of the LAMMPS software and will also aid future researchers in including experimental parameters in their simulations.

We also developed a simulation model in eDPD to reproduce the interfacial thermal resistance. Currently there is no accepted procedure to handle interfacial thermal resistance in LAMMPS. We developed a method to map empirical results to the correct LAMMPS parameter. By systematically tuning the repulsion and heat exchange parameters within

the eDPD model, we established a practical method to quantify the Kapitza resistance, capturing the thermal boundary behavior at the CNT–water interface.

We further demonstrated that thermal rectification, asymmetric heat conduction depending on the direction of thermal gradients, can be effectively modeled within this framework by introducing structural or interactional asymmetry. This result has implications for the design of directional heat transport systems at the nanoscale. We found that by increasing the water/interface repulsion parameter we could tune thermal boundary resistance by nearly 40%. This is important in that by coating a surface with a hydrophobic or hydrophilic material we can tune the thermal conductivity.

We then incorporated DSPE-PEG molecules to study their interaction with SWCNTs. Using a custom-designed coarse-grained molecular architecture for DSPE-PEG with appropriate bonded and nonbonded interactions, we investigated how these amphiphilic molecules anchor onto the nanotube surface. Parameters such as repulsion coefficients (derived from Flory-Huggins theory and empirical studies) and dissipative coefficients (γ) were systematically tuned to ensure stability and realistic interfacial behavior. Our simulations showed successful self-assembly and adsorption of DSPE tails onto the CNT surface, consistent with expectations from molecular design and hydrophobic interactions.

In addition to finding the fraction of bound DSPE-PEG molecules bound to a CNT, we were able to show in the simulations the geometry of how they are bound to the CNT and the competition between CNT/DSPE-PEG bonding DSPE-PEG aggolomeration. Finally by briefly and selectively heating the CNT we found that the DSPE-PEG do not desorb from the CNT. While this is preliminarly, it shows that this simulation can explore heating protocols for optimal therapy.

6.2 Quantitative Metrics

We quantified the percentage of DSPE-PEG molecules that adhered to the SWCNT over time, using center-of-mass distance criteria. Time-resolved plots of sticking percentages were used to evaluate the stability and behavior of the functionalized layer. The results showed a stable pattern of adsorption after an initial equilibration phase, with approximately 70% of the DSPE-PEG sticking to the CNT surface.

6.3 Scientific Implications

This work provides a mesoscopic insight into the thermodynamic and kinetic factors that govern polymer-functionalized CNT systems. The approach lays a foundation for tuning molecular architectures and interaction parameters to optimize thermal and structural behavior for applications in biomedicine and nanotechnology, such as drug delivery or photothermal therapy.

6.4 Future Work

Building upon the results of this study, several avenues can be pursued to deepen our understanding of bio-nano interactions and enhance the performance of carbon nanotube-based systems in biomedical applications:

- *Studying the Effect of Heating on DSPE-PEG Binding:* Future simulations can explore how increased temperature,representing photothermal heating, affects the stability, anchoring, and desorption of DSPE-PEG molecules on the CNT surface.

- *Incorporating Annexin V into the System:* To model early-stage apoptotic signaling or targeted molecular binding, Annexin V can be added to the system and studied for its interaction with DSPE-PEG-coated CNTs. Understanding its binding behavior and mobility could extend the model to more complex biological scenarios.

- *Modeling a Membrane as a Simplified 2D Surface:* A coarse-grained lipid membrane can be introduced as a two-dimensional flexible surface to represent a simplified cell interface. This would allow for the investigation of CNT–membrane penetration, heat transfer through the interface, and potential membrane deformation or disruption.

- *Improving RF Absorption of SWCNTs:* Further studies can explore how the geometry, alignment, or functionalization of SWCNTs affects their ability to absorb radio-frequency (RF) energy. This could involve modeling electromagnetic interactions at a coarse-grained level or coupling eDPD with electromagnetic field simulations to optimize SWCNT designs for more efficient thermal delivery.

These directions aim to bridge the gap between molecular-level simulations and practical biomedical applications, offering a pathway toward more targeted, tunable, and multifunctional nanomaterial systems.

6.5 Concluding Remarks

This research highlights the utility of the eDPD method for bridging microscopic interactions and macroscopic behavior in complex soft matter systems. Through careful modeling and validation, we demonstrated how simulation can guide the design and interpretation of nanotube functionalization strategies in aqueous environments. The methodologies and findings of this thesis contribute to the broader effort to use computational tools to inform nanoscale engineering for biomedical applications.

Appendices

Appendix A

LAMMPS Simulation Input Script

```
units lj
dimension 3
boundary p p p
neighbor 0.2 bin
neigh_modify every 1 delay 0 check yes
neigh_modify one 1500

atom_style hybrid edpd full
bond_style harmonic
angle_style harmonic
pair_style edpd 1.0 9872598

region mybox block -10 10 -10 10 -15 15 units box

read_data cnt30.dat
create_atoms 2 random 35520 276438 NULL

include parmcnt.lammps
bond_coeff 1 200 0.77
bond_coeff 2 180 1.9607888988921507

group CNT type 1
```

```
group liquid type 2

set type 1 edpd/cv 11.4
set type 2 edpd/cv 26.4

compute tliquid liquid temp
compute tCNT CNT temp
thermo_modify temp tCNT

fix mynve all nve
comm_modify cutoff 5.0
comm_modify vel yes

fix mylang1 liquid langevin 0.9 0.9 10 8786
fix_modify mylang1 temp tliquid

fix mylang2 CNT langevin 2 2 10 7768
fix_modify mylang2 temp tCNT

run 10000

unfix mylang1
unfix mylang2

velocity liquid create 0.8 432982 loop local dist gaussian
velocity CNT create 2 432982 loop local dist gaussian

compute mythermo all temp
thermo 100
thermo_modify temp mythermo
thermo_modify flush yes

fix myat1 all ave/time 2 20 100 c_tliquid file temp.liquid1.dat
```

```
fix myat2 all ave/time 2 20 100 c_tCNT file temp.CNT6.dat
fix tether CNT spring/self 50.0


dump mydmp all atom 1000 dump.lammpstrj


timestep 0.0005


run 15000
```

Listing A.1 LAMMPS Input Script for CNT Heating in Water

References

Dmitry Alexeev, Jie Chen, Jens H Walther, Konstantinos P Giapis, Panagiotis Angelikopoulos, and Petros Koumoutsakos. Kapitza resistance between few-layer graphene and water: liquid layering effects. *Nano letters*, 15(9):5744–5749, 2015.

Fernando T Andón, Alexandr A Kapralov, Naveena Yanamala, Weihong Feng, Arjang Baygan, Benedict J Chambers, Kjell Hultenby, Fei Ye, Muhammet S Toprak, Birgit D Brandner, et al. Biodegradation of single-walled carbon nanotubes by eosinophil peroxidase. *Small*, 9(16):2721–2729, 2013.

Khoa Bui, Hai M Duong4, Alberto Striolo, and Dimitrios V Papavassiliou. Effective heat transfer properties of graphene sheet nanocomposites and comparison to carbon nanotube nanocomposites. *The Journal of Physical Chemistry C*, 115(10):3872–3880, 2011a.

Khoa Bui, Brian P Grady, and Dimitrios V Papavassiliou. Heat transfer in high volume fraction cnt nanocomposites: Effects of inter-nanotube thermal resistance. *Chemical Physics Letters*, 508(4-6):248–251, 2011b.

Alessandro Casto, Margherita Vittucci, Fabien Vialla, Aurélien Crut, Francesco Maria Bellussi, Matteo Fasano, Fabrice Vallée, Natalia Del Fatti, Francesco Banfi, and Paolo Maioli. Experimental optical retrieval of the

thermal boundary resistance of carbon nanotubes in water. *Carbon*, 229: 119445, 2024.

Hanna Dillekås, Michael S Rogers, and Oddbjørn Straume. Are 90% of deaths from cancer caused by metastases? *Cancer medicine*, 8(12):5574–5576, 2019.

Hai M Duong, Dimitrios V Papavassiliou, Lloyd L Lee, and Kieran J Mullen. Random walks in nanotube composites: Improved algorithms and the role of thermal boundary resistance. *Applied Physics Letters*, 87(1), 2005.

Pep Espanol. Dissipative particle dynamics with energy conservation. *Europhysics Letters*, 40(6):631, 1997.

Pep Espanol and Patrick Warren. Statistical mechanics of dissipative particle dynamics. *Europhysics letters*, 30(4):191, 1995.

Ming Fang, Kaigang Wang, Hongbin Lu, Yuliang Yang, and Steven Nutt. Single-layer graphene nanosheets with controlled grafting of polymer chains. *Journal of Materials Chemistry*, 20(10):1982–1992, 2010.

Gong Feng. *Mesoscopic Modeling of Heat Transfer in Carbon Nanotube Multiphase Systems*. PhD thesis, 2015.

Christopher J Gannon, Paul Cherukuri, Boris I Yakobson, Laurent Cognet, John S Kanzius, Carter Kittrell, R Bruce Weisman, Matteo Pasquali, Howard K Schmidt, Richard E Smalley, et al. Carbon nanotube-enhanced thermal destruction of cancer cells in a noninvasive radiofrequency field. *Cancer: Interdisciplinary International Journal of the American Cancer Society*, 110(12):2654–2665, 2007.

Robert D Groot. Electrostatic interactions in dissipative particle dynamics—simulation of polyelectrolytes and anionic surfactants. *The Journal of chemical physics*, 118(24):11265–11277, 2003.

Robert D Groot and Patrick B Warren. Dissipative particle dynamics: Bridging the gap between atomistic and mesoscopic simulation. *The Journal of chemical physics*, 107(11):4423–4435, 1997.

Naghmeh Hadidi, Niloufar Shahbahrami Moghadam, Gholamreza Pazuki, Parviz Parvin, and Fatemeh Shahi. In vitro evaluation of dspe-peg (5000) amine swcnt toxicity and efficacy as a novel nanovector candidate in photothermal therapy by response surface methodology (rsm). *Cells*, 10(11):2874, 2021.

Aasgeir Helland, Peter Wick, Andreas Koehler, Kaspar Schmid, and Claudia Som. Reviewing the environmental and human health knowledge base of carbon nanotubes. *Ciência & Saúde Coletiva*, 13:441–452, 2008.

PJ Hoogerbrugge and Johannes MVA Koelman. Simulating microscopic hydrodynamic phenomena with dissipative particle dynamics. *Europhysics letters*, 19(3):155, 1992.

Sumio Iijima. Helical microtubules of graphitic carbon. *nature*, 354(6348):56–58, 1991.

Michael B Jakubinek, Mary Anne White, Minfang Mu, and Karen I Winey. Temperature dependence of thermal conductivity enhancement in single-walled carbon nanotube/polystyrene composites. *Applied Physics Letters*, 96(8), 2010.

Cao JX, Yan XH, et al. Specific heat of single-walled carbon nanotubes: A lattice dynamics study. *Journal of the Physical Society of Japan*, 72(9):2256–2259, 2003.

Nadine Wong Shi Kam, Michael O'Connell, Jeffrey A Wisdom, and Hongjie Dai. Carbon nanotubes as multifunctional biological transporters and near-infrared agents for selective cancer cell destruction. *Proceedings of the National Academy of Sciences*, 102(33):11600–11605, 2005.

B Kitiyanan, WE Alvarez, JH Harwell, and DE Resasco. Controlled production of single-wall carbon nanotubes by catalytic decomposition of co on bimetallic co–mo catalysts. *Chemical Physics Letters*, 317(3-5):497–503, 2000.

Deepthi Konatham and Alberto Striolo. Thermal boundary resistance at the graphene-oil interface. *Applied Physics Letters*, 95(16), 2009.

Zhen Li, Yu-Hang Tang, Huan Lei, Bruce Caswell, and George Em Karniadakis. Energy-conserving dissipative particle dynamics with temperature-dependent properties. *Journal of Computational Physics*, 265:113–127, 2014.

Zhen Li, Xin Bian, Xuejin Li, Mingge Deng, Y.-H. Tang, Bruce Caswell, and George Em Karniadakis. Dissipative particle dynamics: Foundation, evolution, implementation, and applications. In *Particles in Flows*, pages 255–326. Springer, 2017.

A. D. Mackie, J. B. Avalos, and V. Navas. Dissipative particle dynamics with energy conservation: Modelling of heat flow. *Physical Chemistry Chemical Physics*, 1(9):2039–2049, 1999.

Seyed Yazdan Madani, Naghmeh Naderi, Oshani Dissanayake, Aaron Tan, and Alexander M Seifalian. A new era of cancer treatment: carbon nanotubes as drug delivery tools. *International journal of nanomedicine*, pages 2963–2979, 2011.

Mohammed Faiad Naief, Samar Naser Mohammed, Hadil Jubair Mayouf, and Ahmed Mishaal Mohammed. A review of the role of carbon nanotubes

for cancer treatment based on photothermal and photodynamic therapy techniques. *Journal of Organometallic Chemistry*, 999:122819, 2023.

Luís FF Neves, John J Krais, Brent D Van Rite, Rajagopal Ramesh, Daniel E Resasco, and Roger G Harrison. Targeting single-walled carbon nanotubes for the treatment of breast cancer using photothermal therapy. *Nanotechnology*, 24(37):375104, 2013.

Jon L Opsal and Gerald L Pollack. Improved calculations of kapitza resistance: Combined effects of phonon attenuation and impedance matching on kapitza resistance. *Physical Review A*, 9(5):2227, 1974.

JR Partington, RF Hudson, and KW Bagnall. Self-diffusion of aliphatic alcohols. *Nature*, 169(4301):583–584, 1952.

Jonathan E Peters, Dimitrios V Papavassiliou, and Brian P Grady. Unique thermal conductivity behavior of single-walled carbon nanotube- polystyrene composites. *Macromolecules*, 41(20):7274–7277, 2008.

Daniel E Resasco. Carbon nanotubes and related structures. *Nanoscale Materials in Chemistry*, 2, 2009.

Marisol Ripoll, Pep Espanol, and Matthieu H Ernst. Dissipative particle dynamics with energy conservation: Heat conduction. *International Journal of Modern Physics C*, 9(08):1329–1338, 1998.

Alessandro Sanginario, Beatrice Miccoli, and Danilo Demarchi. Carbon nanotubes as an effective opportunity for cancer diagnosis and treatment. *Biosensors*, 7(1):9, 2017.

Kolattukudy P Santo and Alexander V Neimark. Dissipative particle dynamics simulations in colloid and interface science: A review. *Advances in colloid and interface science*, 298:102545, 2021.

Ulf Daniel Schiller. Dissipative particle dynamics. *A Study of the Methodological Background*, 875, 2005.

S Sheikh, B Lonetti, I Touche, A Mohammadi, Z Li, and Micheline Abbas. Brownian motion of soft particles near a fluctuating lipid bilayer. *The Journal of Chemical Physics*, 159(24), 2023.

Sergei Shenogin, Liping Xue, Rahmi Ozisik, Pawel Keblinski, and David G Cahill. Role of thermal boundary resistance on the heat flow in carbon-nanotube composites. *Journal of applied physics*, 95(12):8136–8144, 2004.

Rebecca L Siegel, Angela N Giaquinto, and Ahmedin Jemal. Cancer statistics, 2024. *CA: a cancer journal for clinicians*, 74(1):12–49, 2024.

Kuk Hui Son, Jeong Hee Hong, and Jin Woo Lee. Carbon nanotubes as cancer therapeutic carriers and mediators. *International journal of nanomedicine*, pages 5163–5185, 2016.

Nagappa L Teradal and Raz Jelinek. Carbon nanomaterials in biological studies and biomedicine. *Advanced healthcare materials*, 6(17):1700574, 2017.

Aitor Valdivia and Carlos Jaime. Carbon nanotube transmembrane channel formation and single-stranded dna spontaneous internalization: a dissipative particle dynamics study. *Soft Matter*, 17(4):1028–1036, 2021.

Lauri Viitala, Saija Pajari, Luigi Gentile, Jukka Maatta, Marta Gubitosi, Jan Deska, Maria Sammalkorpi, Ulf Olsson, and Lasse Murtomaki. Shape and

phase transitions in a pegylated phospholipid system. *Langmuir*, 35(11):3999–4010, 2019.

Chao Wang, Ligeng Xu, Chao Liang, Jian Xiang, Rui Peng, and Zhuang Liu. Immunological responses triggered by photothermal therapy with carbon nanotubes in combination with anti-ctla-4 therapy to inhibit cancer metastasis. *Advanced materials*, (48):8154–8162, 2014.

Yan Xiao, Xiugong Gao, Oleh Taratula, Stephen Treado, Aaron Urbas, R David Holbrook, Richard E Cavicchi, C Thomas Avedisian, Somenath Mitra, Ronak Savla, et al. Anti-her2 igy antibody-functionalized single-walled carbon nanotubes for detection and selective destruction of breast cancer cells. *BMC cancer*, 9:1–11, 2009.

Feifan Zhou, Da Xing, Zhongmin Ou, Baoyan Wu, Daniel E Resasco, and Wei R Chen. Cancer photothermal therapy in the near-infrared region by using single-walled carbon nanotubes. *Journal of biomedical optics*, 14(2):021009–021009, 2009.

Wenpeng Zhu, Annette von dem Bussche, Xin Yi, Yang Qiu, Zhongying Wang, Paula Weston, Robert H Hurt, Agnes B Kane, and Huajian Gao. Nanomechanical mechanism for lipid bilayer damage induced by carbon nanotubes confined in intracellular vesicles. *Proceedings of the National Academy of Sciences*, 113(44):12374–12379, 2016.